MECHANICS BASED MODELING FOR IMAGE GUIDANCE IN BREAST CONSERVING SURGERY

By

Morgan Jill Ringel

Dissertation

Submitted to the Faculty of the

Graduate School of Vanderbilt University

in partial fulfillment of the requirements

for the degree of

DOCTOR OF PHILOSOPHY

in

Biomedical Engineering

May 10, 2024

Nashville, Tennessee

Approved:

Michael I. Miga, Ph.D.

Brett C. Byram, Ph.D.

Ingrid M. Meszoely, M.D.

Ipek Oguz, Ph.D.

Jie Ying Wu, Ph.D.

ACKNOWLEDGMENTS

My graduate school journey at Vanderbilt has been a wonderful experience, and I could not have done it without the support of my friends, family, mentors, and peers. I would first like to thank my Ph.D. advisor, Dr. Michael Miga, whose leadership, collaborative spirit, and curiosity have been instrumental in this research project. His optimism and positivity have propelled me through periods of skepticism and self-doubt. He is a wonderful mentor, and I look forward to his continued mentorship in my future career endeavors. I would also like to thank the other members of my thesis committee - Dr. Ingrid Meszoely, Dr. Brett Byram, Dr. Ipek Oguz, and Dr. Jie Ying Wu - for their critiques and guidance. I would especially like to thank Dr. Meszoely for providing her clinical expertise and feedback throughout our research developments, and I want to thank the patients and volunteers who participated in our research studies to make this work possible.

There are two researchers in particular who inspired many of the developments outlined in this dissertation. The first is Dr. Winona Richey. This work is the continuation of her dissertation, and she paved the way for many of the developments presented here. In times of doubt, her excitement for the project along with many hours of passionate discussion have encouraged and refocused my efforts. Her rigor and attention to detail have been vital in holding this work to a high standard. The second is Dr. Jon Heiselman. His generous mentorship and willingness to discuss new developments over Zoom have been invaluable for carrying out this work and shaping my understanding. He has been open and encouraging of new efforts that build upon his previously proposed work. This dissertation would not have been possible without contributions from both Winona and Jon.

I would like to thank all members, past and present, of the Biomedical Modeling Laboratory who played a part in supporting my growth as a scientist - Dr. Ma Luo, Dr. Kyvia Pereira, Frankangel Servin, Bowen Xiang, Kush Hari, Alexander Stabile, Amairanny Espinosa, and others. My first year as a graduate student was spent working on OCT imaging in the Diagnostic Imaging and Image-Guided Interventions Laboratory with Dr. Kenny Tao, Dr. Joe Malone, Dr. Eric Tang, and Rachel Eimen, where I learned valuable lessons and research skills that I carried with me throughout my Ph.D. journey. I owe thanks to the wider research groups at Vanderbilt including the Vanderbilt Institute for Surgery and Engineering (VISE) and the Biomedical Engineering Department for providing a broader network and sense of community. I would like to thank my lifelong friends that I made during my five years in Nashville for their constant support. Finally, I want to thank my family for their love and encouragement, especially my partner Jack for being with me every step of the way.

TABLE OF CONTENTS

LIST OF TABLES

LIST OF FIGURES

LIST OF ABBREVIATIONS

2D	2-dimensional
3D	3-dimensional
ANTs	Advanced Normalization Tools
AR	Augmented reality
BCS	Breast conserving surgery
CT	Computed tomography
DCIS	Ductal carcinoma in situ
FEM	Finite element method
FOV	Field-of-view
FRE	Fiducial registration error
HD	Hausdorff distance
IGS	Image guidance system
IOUS	Intraoperative ultrasound
IQR	Interquartile range
LIBR	Linearized iterative boundary reconstruction
MR	Magnetic resonance
MRI	Magnetic resonance imaging
OR	Operating room
ROI	Region of interest
TRE	Target registration error
US	Ultrasound

CHAPTER I

Introduction

I.1 Specific Aims

Breast conserving surgery (BCS) is a procedure for early-stage breast cancer where the tumor is removed to stop cancer growth and metastasis. The goal of this procedure is to localize and excise the tumor completely while maintaining breast cosmesis. While guideline standardization and new localization techniques have made some improvement, re-excision rates for these procedures remain high meaning that many BCS patients must return to the operating room (OR) for an additional procedure because of positive or close resection margins [11; 12]. The chance of needing a re-excision may be lessened by better intraoperative navigation and localization of the tumor extent and boundary.

Mechanics based modeling of the breast is of interest for many clinical and research applications, including multi-modality image fusion, longitudinal registration, and image-guided surgery. Image guidance requires either utilizing registered preoperatively acquired imaging for navigation or re-imaging during the procedure with an intraoperative imaging suite [13]. While direct re-imaging of the tissue is an attractive direction, workflow encumbrance and high cost are likely to prohibit intra-procedural adoption. Alternatively, using preoperatively acquired, well-resolved imaging data to guide breast conserving surgery (BCS) procedures is a more viable option but would be highly dependent on calculating an accurate image-to-physical registration [14]. Magnetic resonance (MR) imaging is a suitable modality for breast tumor imaging due to its high sensitivity and accuracy for tumor size estimation [15]. Diagnostic breast MR imaging is typically performed in the prone position with the breast pendant, which is subject to large gravity-induced deformations [16]. For the image-guided surgery application, the supine position has been shown to more closely match the surgical presentation [17]. However, even in the supine position, large nonrigid deformations can occur due to changes in arm positioning and table orientation [18]. Compensating for these deformations through nonrigid registration in image-guided surgery is challenging due to limited intraoperative data comprised of sparse point clouds and landmarks localized on the breast surface. Additionally, the nonrigid registration must operate in near real-time to avoid prolonging surgery. Therefore, it's imperative to develop a nonrigid registration method that aligns with sparse data constraints and the intraoperative workflow. This is essential for a fully realized BCS image guidance system (IGS).

The overall goal of this dissertation is to propose a BCS-IGS that improves intraoperative navigation for surgeons by leveraging preoperative imaging with nonrigid registration. More specifically, mechanics based

models that compensate for soft tissue deformations in the breast are employed for this nonrigid registration. The hypothesis is that mechanics based methods will achieve acceptable speed and accuracy for active deformation correction in a realized IGS platform. To accomplish this goal, this dissertation proposes the following three specific aims:

Aim 1: Use supine magnetic resonance (MR) image-to-image registration to inform finite element method (FEM) modeling of surgical deformations. The first aim of this dissertation is to evaluate FEM approaches for modeling deformations from supine breast MR imaging. An intra-subject supine breast MR dataset from healthy volunteers simulating surgical deformations is collected. Nonrigid image-to-image registration is performed to characterize breast tissue displacements and infer FEM boundary conditions. Three FEM models with varying levels of heterogeneity and anisotropy are implemented to model simulated surgical deformations. The modeling results provide a quantitative analysis of how adding additional model complexity affects target accuracy.

Aim 2: Adapt breast deformation models for the intraoperative environment by using regularized Kelvinlet functions for registration. The second aim of this dissertation is to establish a breast deformation model that can be used in the intraoperative environment. For surgical use, the model must rely on data sources collected in the operating room such as sparse point clouds and localized landmarks on the breast surface. Also, the model must run in near real-time to avoid prolonging surgery. To address these challenges, regularized Kelvinlet functions from de Goes et al. are proposed as a model for linear elasticity [19]. These functions are used in combination with a sparse-data image-to-physical registration method detailed in Heiselman et al. to align preoperative imaging to sparse data sources [20]. This model's accuracy is evaluated on the healthy volunteer dataset and on an example case from one breast cancer patient.

Aim 3: Create a breast conserving surgery image guidance system (BCS-IGS) with an integrated breast deformation model for active localization correction. The third and final aim of this dissertation is to deploy the model from Aim 2 to a fully integrated BCS-IGS system for prospective nonrigid registration. The BCS-IGS is a portable cart that includes a display monitor and extendable arm for bedside data collection and navigation. Attached optical tracking and stereo camera sensors are used for surgical scene surveillance and sparse-data collection. Navigation displays, data collection, and registration are controlled from custom-built guidance module software. The BCS-IGS system is tested with active nonrigid registration on breast phantom experiments and one healthy volunteer.

I.2 Impact

Breast cancer is the most commonly diagnosed and the second leading cause of cancer death in women in the United States, with approximately one in eight women being diagnosed in her lifetime [2]. Surgical intervention is recommended for nearly all women with early-stage breast cancer, with a majority (62%) of patients electing for BCS procedures. BCS has been shown to have equivalent survival outcomes to mastectomy procedures, but this is dependent on total tumor excision [21]. Positive margins detected after BCS require patients to have a re-excision procedure. Re-excision rates in the United States remain high hovering just below a 20% rate in most studies [11; 22]. Current standard-of-care intraoperative localization techniques include wire-guided localization, seed-based localization, and direct imaging with intraoperative ultrasound. These technologies have had variable effectiveness in reducing re-excision rates, and not all breast lesions are visible using intraoperative ultrasound [7]. The advancements outlined in this dissertation have the potential to impact clinical care for BCS patients by improving tumor localization and thus reducing the chance of a re-excision procedure. Better navigation capabilities may also benefit cosmetic outcomes because surgeons would be able to delineate the tumor boundary with improved precision. Finally, the BCS-IGS could be utilized as a surgical training tool to aid in one of the more challenging aspects of procedure – using 3D spatial thinking to translate imaging typically viewed in 2D to the surgical field.

From a research perspective, this dissertation details several novel contributions. While many biomechanical breast modeling studies have been previously published, fewer have focused specifically on breast deformations in the supine position due to surgical positioning. The analysis in Chapter IV quantifies accuracy improvements with varying levels of heterogeneity and anisotropy in a linear elastic FEM model, which may be useful for other researchers implementing mechanics based breast models for multiple use cases. Chapter V discusses regularized Kelvinlet functions, which were first proposed as computer animation sculpting brushes, and employs these functions for image-to-physical registration in the breast. This work is the first to propose these functions in an inverse problem format for a medical imaging application. Finally, Chapter VI details the BCS-IGS design and implementation. Although a similar system design was proposed in prior work, this dissertation is the first to demonstrate integrated nonrigid correction with prospective, rather than retrospective, testing.

I.3 Dissertation Structure

This dissertation begins with a background section, Chapter II, which outlines the clinical standard for BCS and current surgical guidance technologies. Next, Chapter III details the technical methods and developments employed in this work. The next sections, Chapters IV, V, and VI investigate the three specific aims of this dissertation. Finally, Chapter VII discusses the future directions and possible expansions of this work.

Additional investigation into modifying the methods from Chapter V for liver registration instead of breast registration is included in Appendix A.

CHAPTER II

Background

This chapter begins with an introduction to breast cancer by providing an overview of the disease, treatment options, and imaging methods. Then, breast conserving surgery (BCS) is discussed in more detail with regards to margin assessment and re-excision rates. Localization technologies in BCS that are used in clinical practice and that have been proposed in research settings are reviewed. Finally, biomechanical modeling methods are introduced with discussions on breast tissue material properties and deformation modeling.

II.1 Breast Cancer Introduction

II.1.1 Breast Cancer Overview

Breast cancer is the most commonly diagnosed and the second leading cause of cancer death in women in the United States. According to the American Cancer Society 2024 cancer statistics, approximately 1 in 8 women (13%) will be diagnosed with invasive breast cancer in her lifetime, and 1 in 39 women (3%) will die from breast cancer [2]. It is estimated that breast cancer will account for 32% of all female cancer cases (310,720 cases) and 15% of all female cancer deaths (42,250 deaths) in 2024 [23]. These trends are hypothesized to continue, as breast cancer is predicted to remain the most commonly diagnosed and the second leading cause of cancer death in women, second to lung cancer, in the United States in 2040 [24].

Breast cancer is divided into different classifications based on its progression, molecular characteristics, and histopathology. These classifications inform prognosis and clinical treatment decisions. The American Joint Committee on Cancer (AJCC) staging system, also referred to as the TNM system, is used by clinicians for patient management. This staging system considers the extent of the tumor size (T), the spread to adjacent lymph nodes (N), and metastasis to distance sites (M) when assigning a stage [25]. Stages are assigned as stage I-IV with subcategories. Broadly speaking, stage I refers to an early stage where the tumor is small and has not spread extensively. Stage II indicates either a larger tumor or greater spread to axillary lymph nodes. Stage III implies that there are large tumor(s) with more lymph node involvement, and stage IV indicates metastatic cancer.

Another breast cancer classification distinction is ductal carcinoma in situ (DCIS) compared to breast cancer that is invasive. DCIS is sometimes referred to as stage 0, and it refers to the presence of abnormal cells confined to the mammary ducts. DCIS is considered a precursor to invasive breast cancer, and it is associated with an increased risk of invasive cancer in the future [26]. The majority (83%) of diagnosed breast cancer cases are invasive breast cancer, meaning that abnormal cells have spread beyond the mammary

lobules or ducts into the nearby breast tissue [2]. For invasive breast cancers, the most common histological subtype is invasive ductal carcinoma where the cancer originated in the mammary ducts. Invasive ductal carcinoma accounts for approximately 8 out of every 10 invasive breast cancer cases. The second most common subtype, accounting for approximately 1 out of every 10 cases, is invasive lobular carcinoma where the cancer originated in the mammary lobules [27]. Other rarer histological subtypes include medullary, mucinous, and tubular carcinomas [28].

Breast cancers are also distinguished by their molecular subtype. These molecular subtypes detail either the presence or absence of the estrogen and progesterone hormone receptors (HR) and the human epidermal growth factor receptor 2 (HER2) expressed by the cancer cells. The main molecular subtypes are Luminal A (HR+/HER2-), Luminal B (HR+/HER2+), basal-like (HR-/HER2-), and HER2-enriched (HR-/HER2+). These molecular subtypes influence treatment decisions and patient prognosis [29].

II.1.2 Breast Cancer Treatment Options

Breast cancer treatments include hormone therapy, chemotherapy, surgical resection, radiation, and immunotherapy. Treatment regimens are dependent on tumor subtype, anatomic cancer stage, and patient preferences [30]. For DCIS, most patients undergo surgery with some also electing for adjuvant therapy. Although still under investigation, preliminary findings show that some DCIS patients have a limited risk of invasive progression, and active monitoring has been proposed as an alternative to surgical intervention in some patients [31]. For invasive breast cancer, the distribution of selected treatment options by stage are shown in Figure II.1. Most treatment plans take a multi-faceted approach that seeks to benefit from the combinatorial effects of multiple treatment methods.

The two surgical treatment options for breast cancer are mastectomy, where the entire breast is removed, and breast conserving surgery (BCS), where the tumor and a margin of healthy breast tissue is removed. BCS can also be referred to as lumpectomy or partial mastectomy. The decision to undergo mastectomy versus BCS is dependent on cancer staging, personal preference, and clinician suggestion. As shown in Figure II.1, 62% of patients with early-stage breast cancer (stages I and II) underwent BCS either with or without radiation therapy and 33% underwent mastectomy in 2018. In comparison, only 23% of patients with stage III breast cancer underwent BCS while 62% underwent mastectomy. BCS procedures have been shown to have equivalent, and in some studies superior, survival rates to mastectomies for early-stage patients and offer several advantages over mastectomies such as better cosmetic outcomes and faster recovery times [32; 21; 33; 34; 35]. Despite these studies, in recent years BCS candidate patients have been electing for either unilateral mastectomy or bilateral mastectomy (where the contralateral healthy breast is also removed during surgery) at an increasing rate. The number of BCS candidate patients ages 20-44 that have elected to have a

bilateral mastectomy has increased from 10% to 33% from 2004 to 2012 [36]. This trend is occurring despite any evidence that mastectomy offers survival benefits for these patients, and the fact that mastectomy is associated with more post-surgical complications. Reasons cited for this choice include physician suggestion, fear of recurrence, hesitation about radiation therapy, and concerns about breast symmetry [37; 38]. This trend has led some to advocate for higher rates of BCS procedures, and the National Accreditation Program for Breast Centers set the standard in 2018 that a target rate of at least 50% of eligible early-stage breast cancer patients should be treated with BCS [39; 40]. The surgical protocol, margin status, and re-excision rates for BCS are discussed more in Section II.2

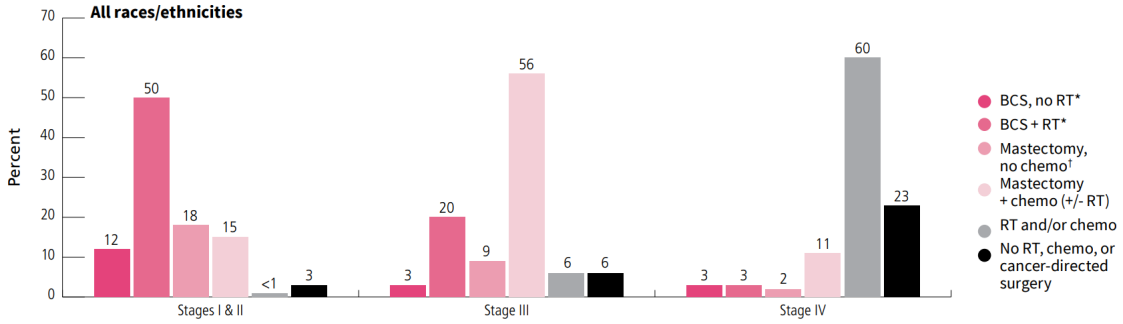

Figure II.1: Breast cancer treatment patterns (%), by stage, 2018. Image reprinted from [2] with permission.

II.1.3 Breast Cancer Imaging

Early breast cancer detection is associated with better outcomes and 5-year survival rates. Early detection relies on the use of diagnostic medical imaging. The three diagnostic imaging modalities used in breast are mammography, magnetic resonance (MR) imaging, and ultrasound. For women with an average risk of breast cancer, the American Cancer Society 2015 Guidelines for Breast Cancer Screening recommends that women ages 45 and older complete mammogram screening annually, with women having the options to begin annual screening at age 40 and to switch to every other year screening at age 55. For high risk women, screening with a mammogram and MR imaging is recommended starting at age 30 [41]. In addition to disease diagnosis, breast imaging is performed at different times throughout the course of treatments. Breast imaging can be acquired for presurgical planning, evaluating the tumor response to different therapies, biopsy guidance, wire or seed placement guidance prior to surgery, radiation therapy planning, and continued surveillance monitoring post-treatment. Breast imaging modalities are reviewed below.

Mammography

Mammography is the standard screening modality for breast cancer, and it involves compressing the breast tissue and acquiring a 2D image using low-energy X-rays. Typical mammography imaging includes oblique

and craniocaudal views. By 2015, digital mammography had replaced film mammography in the United States with 97% of machines being digital [42]. Mammography screenings have been shown to significantly decrease breast cancer mortality through randomized controlled trials [43]. A European study demonstrated that the risk of dying from breast cancer was reduced by 41% for women who participated in mammography screening [44]. While mammography is generally effective for detecting early breast cancer, it is less effective for women with dense breast tissue. According to a study conducted by the Breast Cancer Surveillance Consortium, mammography sensitivity is approximately 93% for women with fatty breasts but only 57% for women with dense breasts [45]. For breast cancer survivors undergoing routine surveillance imaging, scarring and anomalies from surgery and radiation treatment can make recurrence harder to detect on mammography [46]. Mammography is also an ionizing imaging modality that carries the minor risk of exposure to radiation.

Digital breast tomosynthesis, also known as 3D mammography, is a type of mammography imaging that constructs a 3D imaging volume of the breast. Studies have shown that digital breast tomosynthesis has improved detection rates and reduced false-positive rates for breast cancer, especially for women with dense breast tissue [47]. However, it requires additional radiation exposure when combined with standard mammography imaging. Although digital breast tomosynthesis imaging is now available at the majority of breast imaging centers in the United States, reimbursement policies are variable depending on the state and health insurance plan [48].

MR Imaging

Breast MR imaging acquires a high resolution volumetric image of breast tissue. Patients are positioned in the MR scanner bore which contains a strong magnet, usually either 1.5 Tesla or 3.0 Tesla in strength. Patients lay in the prone position with their arms above their head and with the breast hanging pendant in a specialized breast imaging coil (Figure II.2A). Radiofrequency coils are used to perturb and measure the alignment of hydrogen atoms in the body which creates tissue contrast in an MR image. An intravenous contrast agent, typically gadolinium, is administered for improved MR imaging contrast for tumor localization and measurements. Solid tumor growth is associated with new and leaky blood vessels (neoangiogenesis) which causes faster extravasation of the contrast agent during imaging and appears as a bright, locally enhanced region on the resulting scan [15]. Unlike mammography, MR imaging is a non-ionizing modality. MR imaging is recommended for breast cancer screening in women with a high lifetime risk of breast cancer of at least 20-25% or in women with previous chest radiation therapy [2]. Breast MR imaging has high sensitivity at over 90%, and it can identify smaller lesions that can be missed in mammography [49]. It has comparable specificity to mammography, but widespread screening with MR imaging is not recommended for women with an average risk of breast cancer in the United States due to the risk of identifying false positives, which

adds unnecessary stress and concern for patients [50]. MR imaging is particularly useful for imaging women with dense breast tissue – MR was shown to be the best supplemental imaging modality for women with an average risk of breast cancer with dense breast tissue that had lesions that were undetected on mammography [51].

Although not standard of care, performing MR imaging with the patient positioned lying on their back in the supine position has been explored in research studies (Figure II.2B). Prone MR imaging is typically the opted-for position because of tissue separation from the pendant position, a reduction of breathing motion artifacts, and the ability to use breast MR coils for acquisition. A feasibility study showed no significant difference in diagnostic value, lesion classification, or image quality between supine MR scans with contrast and prone MR scans with contrast [52]. This study, and most supine MR studies reported in the literature, utilized a standard torso coil placed on top of the patient in lieu of a breast coil. The torso coil was positioned so that the breast was not compressed, and it provided comparable image quality compared to using the breast coil. Although not required for the majority of supine MR imaging studies, others have designed a custom supine breast receive coil to conform to the supine breast shape, which showed comparable image quality to diagnostic MR imaging [53].

The main quantitative differences caused by supine compared to prone MR imaging are observed in measuring lesion volume, lesion geometry, and lesion location relative to anatomical landmarks like the nipple and chest wall [17; 54; 5; 16]. This is visually shown in Figure II.2C. Tumor displacements between 3-6 cm were observed in the three orthogonal directions between prone and supine imaging [17]. The tumor's mean distance to the chest wall and nipple decreased by approximately 70% and 18% respectively when imaged in the supine position, although these measurements vary depending on the tumor's location in the breast tissue [16]. When comparing tumor size to histology, prone imaging overestimated tumor size by 47% while supine imaging overestimated tumor size by only 15% [16]. Finally, a pairwise comparison showed changes in tumor volume (average 23.8% change), surface area (average 6.5% change), and sphericity (average 6.8% change) between prone and supine imaging with wide ranges of variability among patients [5].

A key advantage of supine breast MR imaging related to this work is the improved correspondence for informing tumor localization during BCS procedures [13; 55]. The large tumor measurement differences between prone and supine imaging noted above mean that the breast imaging referenced by surgical teams prior to BCS – typically mammography and/or prone MR imaging – are not maximally informative of the observed tumor measurements in the operating room. Supine MR imaging may offer a 3D representation of the tumor relative to anatomical landmarks that better matches the surgical presentation. The clinical impact of using supine MR imaging to improve BCS outcomes has been variable. One study used supine breast MR imaging to create a tumor boundary outline that was projected onto the breast surface prior to surgery.

Patients treated with this method had smaller excised lesions and lower positive margin rates compared to a control group [56]. Another study acquired supine breast MR imaging with a thermoplastic shell fitted to the breast shape. This shell allowed for precise preoperative incision markings to be placed on the skin while referencing the supine MR image. Out of $N = 35$ patients included in the study, 25 had negative margins and 7 had positive margins – a 21.2% positive margin rate [57]. A third study acquired preoperative supine MR imaging for $N = 1,150$ patients but showed a similar positive margin rate (18.8%) to those who had prone MR imaging [58]. This implies that just acquiring supine MR imaging alone may not be sufficient for improving clinical outcomes, but that using supine MR imaging in combination with an active guidance method during the operation may be a promising approach. Previously proposed BCS image guidance methods are discussed further in Section II.3.4. Other advantages associated with supine MR imaging and related to breast cancer treatment (but not as closely relevant to the work in this dissertation) include better alignment between MR and ultrasound imaging since ultrasound is acquired in the supine position and the potential use of supine MR in conjunction with CT for radiation therapy planning [59; 60].

Figure II.2: Breast MR imaging in (A) the prone scanning position and (B) the supine scanning position. (C) Overlayed contrast-enhanced MR images in the prone and supine positions with 3D prone (blue) and supine (green) tumor models. Images reprinted from [3; 4; 5] with permission.

Ultrasound

Breast ultrasound (US) imaging relies on tissue acoustic impedance differences for image contrast. A breast US imaging exam is performed with the patient in the supine position. A trained sonographer places a hand-held transducer on the breast surface that emits and receives US waves at frequencies between 3-12 MHz to acquire 2D B-mode anatomical images [61]. It is a non-ionizing imaging modality, and it is cheaper than MR imaging. US alone is not used as a screening modality for breast cancer, but instead it is used as a second imaging method to evaluate abnormal findings when a mammogram is inconclusive. Like MR imaging, US is effective in detecting breast cancers missed by mammography for women with dense breast tissue [62]. Using US alone for detection has been shown to have comparable sensitivity to mammography, but worse specificity meaning it is more likely to identify false positives [63]. It can be used to distinguish between solid lesions which may require biopsy and cysts or fluid-filled lesions which are more likely benign. US

is also accompanied by a doppler imaging mode to quantify tumor vascularization and blood flow. In research settings, US-based imaging techniques that probe tissue mechanical properties including elastography imaging, shear wave elastography, and acoustic radiation force impulse imaging for are being explored for differentiating between benign and malignant breast lesions [64].

In addition to diagnostic imaging, US is employed for guiding breast cancer intervention procedures because of its real-time nature. It is often used for needle visualization and guidance during biopsy procedures. For BCS specifically, US can be used to localize the tumor intraoperatively. Intraoperative ultrasound (IOUS) is explored more as a guidance technology in Section II.3.3.

II.2 Breast Conserving Surgery

II.2.1 Surgical Protocol

BCS procedures begin by positioning the patient in the supine position on the operating table and administering monitored anesthesia. The patient is draped and sterilized in preparation for the procedure. The surgical team reviews available imaging to confirm lesion size and location. The surgeon uses a handheld probe to locate any seeds that were placed at the tumor site prior to surgery. They may also palpate the breast to identify the tumor location. They plan the incision by indicating the incision path on the skin with a marker. The procedure begins with the surgeon making an incision. The surgeon uses the Bovie cautery device to form skin flaps to access the tumor site. The cavity is held open with surgical retractors. The handheld probe may be used throughout the procedure to reidentify the seed location(s). Once the tumor site is identified, the surgeon mobilizes a plug of tissue for excision. Single stitches may be attached to the tissue plug boundary prior to excision to help maintain anatomical orientation. After mobilization, the tissue plug is excised and placed on a sterile cloth. The tissue plug is immediately inked on the boundary with 6 colors that indicate the anatomical directions (anterior, posterior, superior, inferior, medial, and lateral) of the plug relative to the resection cavity. The tissue plug is sent to the hospital's pathology lab for imaging and intraoperative evaluation. X-ray imaging is acquired to rapidly evaluate the tissue plug margins. Intraoperative frozen section analysis may also be performed. Depending on the resulting imaging, an additional cavity shaving specimen may be removed and evaluated. To conclude the procedure, the incision is closed, and the excised tissue specimens are sent to pathology for postoperative margin assessment. BCS procedures may also be accompanied by sentinel lymph node biopsy or axillary lymph node dissection procedures to evaluate if cancer cells have spread to the lymph nodes and evaluate the risk of metastatic cancer [65].

II.2.2 Resection Margins

Tumor margin status is an assessment of the presence of malignant cells at or close to the excised tissue specimen boundary. Margin status acts as an implied indicator of residual cancer remaining in the breast after surgery. Margins can be classified as either negative, close, or positive. Margin status is correlated to the likelihood of recurrence and is used to inform subsequent treatment decisions including the need for re-excision. The most current BCS margin guidelines were defined by the Society of Surgical Oncology (SSO) and American Society for Radiation Oncology (ASTRO) for invasive breast cancer in 2014 and for DCIS in 2016 [66; 67]. The most recent official consensus statement about BCS margin guidelines was released by the American Society of Breast Surgeons in December 2017. Prior to 2014, there were no consensus guidelines for defining negative and positive margins which meant that centers had different criteria for when a re-excision was necessary [68]. A positive margin, shown in Figure II.2, is defined as "tumor on ink" during histological analysis. In the case of positive margins, re-excision surgery is recommended for invasive breast cancer and DCIS. A close margin refers to tumor cells being present within a 2 mm border of the inked specimen edge. A negative margin, also shown in Figure II.2 is defined as "no tumor on ink". For invasive breast cancer, re-excision surgery is not recommended for negative or close margins. For DCIS, re-excision is recommended for close margins but not recommended for negative margins.

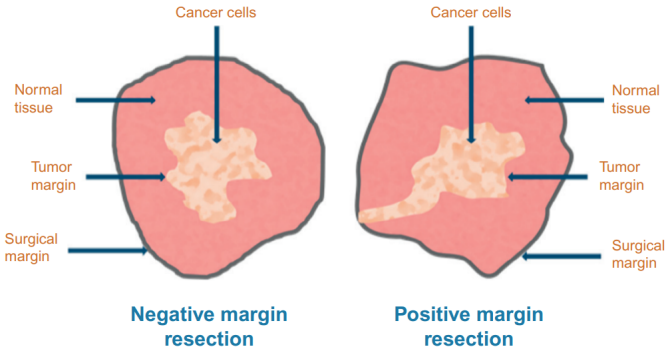

Figure II.3: Negative and positive tumor margin status. Image reprinted from [6] with permission.

Histological assessment is the current gold standard for margin designation. After the BCS procedure, the specimen is sent to pathology where it is fixed and stained with hematoxylin and eosin (H&E) and examined under a microscope for cancerous cells. This process is completed several days or sometimes weeks after the surgery. Although it is the gold standard for margin assessment, H&E histology is not a feasible intraoperative technique because of the time required. Thus, additional pathological and imaging approaches for rapid margin assessment during the procedure are of interest. A cheap, effective, and rapid intraoperative margin assessment technology for BCS comparable to H&E histology may help reduce re-excision rates for patients. While important, these efforts should be viewed as complementary to, rather than replacements for, surgical

guidance. Intraoperative identification of positive margins after excision is important, but accurate first-pass excision is desired for optimal cosmetic outcomes. Current clinical and state-of-the-art research technologies for intraoperative margin assessment are reviewed below.

Intraoperative frozen sectioning is a rapid pathology approach where small samples from the specimen are examined under a microscope while the patient is still in the operating room under anesthesia. Its use depends on the hospital – some centers routinely perform frozen section analysis for BCS procedures, while others use it more selectively. Although frozen sectioning is similar to H&E histology, it examines only small regions of the specimen border and can be impacted by freezing artifacts [69]. It has been shown to significantly reduce re-excision rates, but it is not a substitute for H&E histology given its low sampling rate [70]. Another alternative pathology approach used by some hospitals is imprint cytology, where the specimen surface is carefully pressed onto a glass slide allowing cancerous cells to adhere to the slide surface. The slide is then examined under a microscope for margin evaluation. This technique has been shown to be less sensitive than frozen section analysis, but it can be performed rapidly and has better coverage of the entire specimen surface [69]. Results can be impacted by charring from cauterization on the specimen surface.

The standard imaging approach for intraoperative margin assessment is specimen x-ray imaging. These x-ray machines offer high energy and high resolution (10-20 μm) imaging for improved specimen visualization compared to screening mammography machines. They are used to image microcalcifications and tumor margins in the specimen after excision, although distinguishing between tumor and dense glandular tissue can be challenging. Miro-CT specimen imaging, which provides a 3D volumetric image, may offer improved soft tissue contrast compared to a 2D projection in x-ray imaging. However, distinguishing between tumor and dense tissue is still difficult in micro-CT imaging. Significant clinical benefits compared to x-ray imaging have yet to be demonstrated to justify the additional time and resources required for micro-CT imaging. One study that included a cohort of $N = 100$ patients showed that the inclusion of micro-CT altered the surgical decision after first-pass excision in 6.3% of cases and estimated that micro-CT may reduce re-excision rates by 2.2% compared to x-ray imaging alone [71].

Substantial efforts have focused on developing unconventional imaging methods for intraoperative margin assessment. These techniques rely on measuring a distinct signature from malignant cells on the specimen surface to indicate margin status. Previously demonstrated optical and non-optical methods include radiofrequency spectroscopy, bio-impedance spectroscopy, optical coherence tomography, photoacoustic microscopy, nonlinear microscopy, Raman spectroscopy, and hyperspectral imaging [72]. Radiofrequency spectroscopy relies on differences in electromagnetic scattering and absorbance to detect residual cancer. The MarginProbe (Dilon Technologies, Newport News, VA, USA) uses radiofrequency spectroscopy and was approved by the Food and Drug Administration in 2013 for BCS intraoperative margin assessment in the United States [73]. It

includes a handheld probe and console for real-time detection of cancerous cells on the specimen surface after excision. A clinical study showed that using MarginProbe for immediate intraoperative margin assessment reduced re-excision rates from 26% to 20% compared to standard-of-care BCS with no significant change in total excised specimen volume [74]. Other intraoperative margin imaging methods have been demonstrated in research settings with varying sensitivities, specificities, benefits, and tradeoffs [69]. While promising, these methods have not replaced x-ray imaging and histological approaches as the standard-of-care for intraoperative margin assessment.

II.2.3 Re-excision Rates

A primary concern with BCS is that re-excision rates for these procedures remain high. A re-excision (or reoperation) procedure requires a patient to return to the operating room for an additional surgery because of incomplete tumor excision. As stated above, this is recommended for positive margins in invasive cancer patients and for positive and close margins in DCIS patients. Re-excision procedures have been found to be effective in reducing the risk of local recurrence. A population study of BCS patients where 19% of the study cohort needed re-excision surgery found that the re-excision patients who had an additional BCS or mastectomy surgery had equivalent survival outcomes compared to those who did not require re-excision operations [75]. However, this does not diminish the importance of reducing re-excision rates from an individual and population health standpoint. The study stated that, "The significant variation in the likelihood of re-excision by geography and by individual surgeon is concerning, especially given the costs to the patient associated with additional surgery and the financial costs to the health system." Successful first-pass tumor excision is the primary goal of BCS for optimal outcomes.

Prior to the release of the SSO-ASTRO margin guidelines in 2014, it was estimated that 20-40% of BCS patients would require a re-excision procedure [76; 77]. After six years of guideline adoption, a study reported a significant decrease in post-guideline re-excision rates compared to pre-guideline rates [78]. This is likely because of the lack of standardization during the pre-guideline period. Prior to 2014, only 11-15% of breast surgeons reported that they accepted a "no tumor on ink" margin. Thus, it was common practice among the majority of surgeons to advocate for re-excision surgeries, even in cases of negative margins, reflecting a more aggressive surgical approach during the pre-guideline period [79; 80]. Despite guideline standardization, re-excision rates still remain high hovering just below a 20% rate in most studies in the post-guideline period. Two 2019 studies reported 17.2% and 16.1% re-excision rates in the United States post-guideline changes [11; 22]. These rates have also been reported to be highly variable depending on the individual surgeon and hospital center. The hospital facility has been shown to be the most impactful determinant influencing whether a patient has a re-excision procedure, and only 1 in 4 facilities achieve re-

excision rates below 10% [22]. Regarding surgeon variability, approximately 1 in 6 (17.5%) breast surgeons have an individual re-excision rate higher than the expert consensus cutoff of a 30% re-excision rate [11].

Spatial reasoning has been reported as one of the main challenges when teaching and learning BCS procedure techniques, and it may be one of the factors contributing to high and variable re-excision rates among surgeons. Direct quotes from surveying breast surgeon educators and trainees about procedural challenges include, "Sometimes the mammogram can throw you off—location of the actual lesion can be different," "It is very hard to take out the right amount of tissue, especially with no landmarks," and "It's hard to learn to think in 3D" [81]. The two main abilities that were cited for differentiating the educators and trainees were being able to conceptualize the lesion and being able to use 3D spatial thinking to visualize the lesion from 2D imaging. Technologies that address these challenges may be beneficial for improving BCS outcomes.

Overall, these high re-excision rates are detrimental to patient care. Re-excision procedures delay subsequent therapy, result in less favorable cosmetic outcomes, and are additional stress on the patient. In a survey of 592 BCS patients after treatment, having a re-excision procedure was associated with significantly lower postoperative satisfaction [82]. Re-excision procedures are also an additional financial burden on the healthcare system. A cost analysis estimated that re-excision procedures cost between $40-53.7 million annually in the United States [83]. Given (1) the commonality of BCS procedures, (2) the high and variable re-excision rates associated with BCS procedures, and (3) the additional cost and emotional burden caused by re-excision, investigations into techniques for successful first-pass tumor excision are a top priority. Reducing re-excision rates is the main clinical motivation for the work presented in this dissertation. A review of clinically adopted and state-of-the-art localization technologies to reduce re-excision rates are explored next (Section II.3).

II.3 Localization Technology

Breast surgeons rely on technologies to locate the tumor for pre-incision case planning and intraoperative localization during BCS, although the specific technology employed depends on the case and hospital center. This section divides BCS localization technologies into wire-guided localization, seed localization, direct imaging techniques, and navigation platforms.

II.3.1 Wire-guided Localization

Wire-guided localization involves placing a wire in the targeted tumor area prior to surgery using mammography or ultrasound imaging so that the tumor can be located intraoperatively. Wire-guided localization is a well-established method that has been shown to be safe and effective [84]. It is also cheaper than some of the more novel methods. However, its use has been decreasing in favor of other localization methods. One study of a sample cohort reported that BCS procedures using wire-guided localization decreased from 68%

of procedures in 2015 to 38% in 2019 as shown in Figure 2 [7]. The average aggregated rate of positive margins after first-pass excision for BCS procedures performed with wire-guided localization reported by 13 studies from 2015-2021 is 21.7% [85; 86; 87; 88; 89; 90; 91; 92; 93; 8; 94; 95]. During resection, the wire tip that designates the estimated tumor centroid is not visible to the surgeon so its location must be estimated. Additionally, the placement of a singular wire in the tumor does not provide any information about where the tumor boundary edges are located to guide resection.

A main disadvantage of wire-guided localization driving adoption of alternative methods is patient comfort. After placement, the wire protrudes out of the skin which is uncomfortable for patients. The external wire may migrate, fracture, or dislodge prior to surgery which compromises care [96]. Wire-guided localization is also challenging from a logistical standpoint because the wire placement typically occurs on the same day prior to surgery. This reduces the ability of hospitals to flexibly schedule surgeries and presents more challenges compared to using localization devices that can be inserted days or weeks in advance.

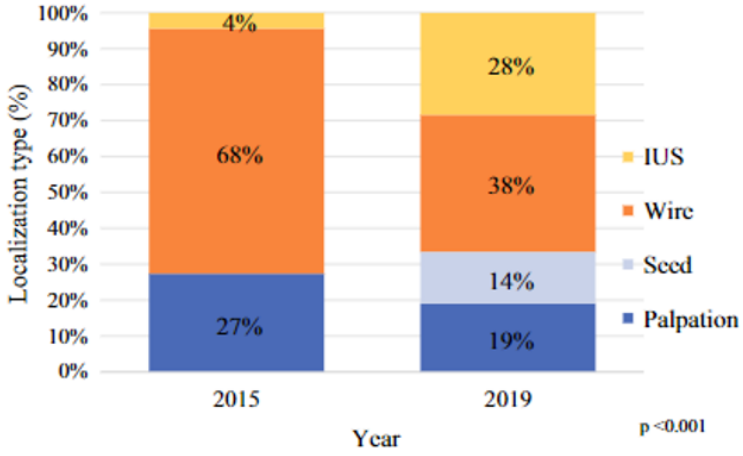

Figure II.4: Use of localization methods in 2015 ($N = 1815$) versus 2019 ($N = 2226$). Image reprinted from [7] with permission.

II.3.2 Seed Localization

Seed-based localization technologies are a more modern alternative to wire-guided localization. A small seed (3 – 12 mm in length depending on the technology) is implanted with a needle in the estimated tumor centroid using mammography or ultrasound imaging prior to surgery for intraoperative localization. Different seed-based technologies have been used, each with its own advantages and disadvantages. Various seed-based technologies include radioactive seed localization, magnetic seed localization, and radar seed localization.

Radioactive seed localization involves placing a radioactive seed that contains Iodine-125 and emits gamma radiation. To localize the seed during surgery, a handheld gamma probe is used to display the dis-

tance from the probe to the seed, and the surgical incision is planned accordingly. Since radioactive seeds involve using radioactive materials, the process is regulated by the U.S. Nuclear Regulatory Commission and requires extra planning and safety precautions in case of a seed rupture and seed disposal [97]. However, one advantage is that Iodine-125 has a half-life of 60 days, so seeds can be placed further in advance compared to wire-guided localization. Seed placement is also more comfortable for the patient [98]. The average aggregated rate of positive margins after first-pass excision for BCS procedures performed with radioactive seed localization reported by 6 studies from 2015-2018 is 19.9% [86; 88; 89; 90; 92; 99]. Direct comparison studies between wire-guided and radioactive seed localization demonstrated comparable outcomes regarding positive margin rates, specimen volume, and cosmetic outcomes between the two methods [100; 101]. Regarding patient preference, patients who received radioactive seed localization had higher overall satisfaction and procedure convenience ratings compared to patients who received wire-guided localization [102].

Magnetic seed localization uses an implantable seed that can become temporarily magnetized when used with the corresponding handheld probe. Magnetic seed localization is commercially known as Magseed (Endomatics Inc., Cambridge, UK), and it received approval for BCS guidance in the United States in 2016. It relies on implanting a 5 mm seed under ultrasound or mammography guidance up to 30 days prior to surgery. The reported rate of positive margins after first-pass excision for BCS procedures performed with magnetic seed localization from 6 studies from 2018-2021 ranged from 12-24% with an aggregate average of 16.8% [103; 104; 105; 93; 106; 107]. Unlike radioactive seed localization, there are no radiation safety concerns with magnetic seed localization. While the seed is MR compatible, it can cause a bloom imaging artefact up to 4 cm in size [108]. While it is a competitive method in terms of positive margin rates and patient satisfaction, it is not available at all hospitals.

Radar seed localization is similar to radioactive and magnetic seed localization in that it involves an implanted seed and handheld probe for localization. The SAVI SCOUT system (Merit Medical, South Jordan, UT, USA) uses a 12 mm reflector seed and a handheld probe that emits radar and infrared waves to measure the distance to the reflector. Like the Magseed, the reflector seed can be implanted up to 30 days before a patient's surgery. Four studies from 2016-2018 that used the SAVI SCOUT reported positive margin rates ranging from 7.0-14.9% with an aggregate average of 10.4% [91; 109; 110; 111]. One limitation is that reflector placement deeper than 6 cm may affect seed detection, meaning that the system may not be suitable for all patients and tumors.

The main limitation of all seed-based methods is that localization information is limited to one discrete point that is dependent on the accuracy of the seed placement. Seed bracketing, where several seeds are placed to designate the lesion extent, addresses this by providing more points. One study that used multiple radioactive seed localization bracketing showed a statistically significant decrease in the re-excision rate in

BCS patients that had multiple seeds implanted (N=58, 20.7% re-excision rate) compared to patients that had one seed implanted (N=48, 39.6%) [112]. The EnVisio SmartClips system (Elucent Medical, Eden Prairie, MN, USA) is another bracketing approach that uses electromagnetic signals from triangulated seeds. It involves placing three 10 mm seeds with unique electromagnetic signals around the tumor. During BCS, a handheld stylus is used to measure the distances to the three seeds for improved tumor navigation. It received approval for BCS procedures in the United States from the Food and Drug Administration in 2019. In a preliminary study, EnVisio SmartClips were shown to be safe and reliable for lesion localization, but current studies evaluating efficacy compared to other localization technologies are ongoing [113]. While these new technologies may offer slight improvements in positive margin and re-excision rates, multiple seed localization information is still limited because these methods are unable to provide intraoperative information about the full lesion extent.

II.3.3 Direct Imaging

Intraoperative Ultrasound (IOUS) Imaging

Direct intraoperative imaging can be used to visualize the full tumor boundary thus addressing the main limitation of seed-based methods. The primary intraoperative imaging method that has been investigated for BCS guidance is intraoperative ultrasound (IOUS). IOUS can be used to locate the lesion prior to sterilization and incision to help inform the surgical plan. It can also be used during the procedure to visualize the lesion in the resection cavity and after excision to visualize margin extent on the excised specimen. Like seed-based methods, the use of IOUS for BCS localization has increased from use in only 4% of cases in a 2015 study cohort to use in 28% of cases in a 2019 study cohort shown in Figure II.4. Six recent studies that have used IOUS for localization have reported re-excision rates ranging from 1.5-28.6% with an aggregate average re-excision across all studies of 12.6% [87; 94; 114; 115; 116; 117]. In two direct comparison studies, BCS performed with IOUS demonstrated significantly improved re-excision rates compared to wire-guided localization (3% compared to 13%) but comparable re-excision rates to seed-based localization (11% compared to 8%) [118; 119]. Other related surgical outcomes effected by IOUS include positive margin rates, total excised lesion volume, and cosmetic outcomes. In a randomized controlled trial, the use of IOUS reduced the positive margin rate from 17% to 3% compared to palpation alone [120]. IOUS has also been shown to result in smaller excised lesion volumes – averaged excised volumes of 38 cm^3 with IOUS compared to 57 cm^3 without IOUS – suggesting favorable postoperative cosmetic outcomes [120]. When cosmetic outcomes were directly evaluated by measuring patient satisfaction, 20% reported excellent cosmesis and 6% reported poor cosmesis in the IOUS patient group, compared to 14% excellent and 13% poor in the palpation only patient group [121].

While IOUS is considered to be beneficial and effective for improving surgical outcomes, especially for nonpalpable lesions, several disadvantages should be noted. The use of IOUS may extend surgical procedure time, leading to higher costs and more risk for the patient. However, one study noted an extra 2-5 minutes required for IOUS which is likely negligible given the potential guidance benefits [122]. Surgeons require technical training to acquire and interpret breast ultrasound imaging. While this is a barrier, one study showed that breast surgeons demonstrated proficiency in IOUS after eight procedures [123]. Finally, IOUS requires a designated US machine, but the portability and low cost of US makes resource availability a minor concern in most hospitals.

Another concern when using IOUS for guidance is tumor visibility on US imaging. Not all breast lesions are echogenic, which confounds the use of IOUS. Results from studies quantifying the presence of sonographically occult breast lesions (not visible on US) have been variable. One study estimated that only 50% of nonpalpable lesions are visible on ultrasound, meaning that IOUS is not applicable in all cases [124]. Another study found that out of 231 nonpalpable breast lesions, 32 (13.8%) were sonographically occult but noted that the true rate of not visible lesions is likely higher [125]. Small microcalcifications often associated with DCIS can be missed with IOUS since its presentation can mimic that of normal breast structures [126]. Non-mass-like lesions are difficult to detect using IOUS, particularly when they are small and flat in shape. [127]. Obesity and large breast volumes can also limit IOUS abilities for localizing deeply posterior lesions. US artifacts like acoustic shadowing and imaging artifacts from air or foreign bodies can make IOUS difficult in practice [128]. To assist with IOUS visualization, the placement of sonographic visible clips bracketing the lesion under mammography guidance has been proposed so that the region of interest can be quickly and easily identified during IOUS [129]. However, this method does not solve the problems outlined for seed-based methods like clip migration and lack of full boundary visualization.

Research efforts have expanded the capabilities of IOUS to tracked IOUS, where an ultrasound imaging device is combined with an optical or electromagnetic tracking device [130]. Tracked IOUS involves monitoring the position and orientation of the ultrasound transducer combined with a 3D navigation view that provides a more intuitive view of the imaging plane and patient anatomy. This improves the surgeon's ability to visualize the ultrasound plane and navigate during a procedure. The use of tracked IOUS in BCS is limited, but one study demonstrated a tracked IOUS navigation platform used successfully for navigation during six BCS procedures [131]. Tracked IOUS has been explored more extensively in neurosurgery, abdominal surgery, and orthopedic surgery. In this work, tracked IOUS is leveraged not for the direct imaging of the tumor boundary because, as noted above, direct IOUS imaging of breast tumors is variable. Instead, it is used to locate specific anatomical structures (namely the breast chest wall) in a BCS image guidance system. This is explored more in Chapter VI.

Intraoperative MR Imaging

Intraoperative MR imaging has also been explored to image residual tumor in the cavity after excision in BCS procedures. This methodology has been limited to the Advanced Multimodality Image Guided Operating Suite (AMIGO) at Brigham and Women's Hospital, which is an operating room equipped with a ceiling-mounted MR scanner so that a patient can be imaged while on the operating table. Intraoperative MR imaging was acquired on 12 BCS patients demonstrating the feasibility of the approach, and 2 out of the 12 enrolled patients needed a re-excision procedure [13]. While intraoperative MR imaging for BCS guidance would allow high resolution imaging of tumor position and extent, intraoperative MR suites are not an available resource outside of the AMIGO Suite. This limitation and the importance of pursuing alternative image guidance approaches for improved BCS outcomes are noted in the study.

II.3.4 Navigation Platforms

To combat the fact that intraoperative imaging is not an available option for all BCS cases, navigation platform approaches that leverage preoperatively acquired imaging have been proposed. Acquiring imaging prior to surgery and registering these images to the surgical field provides an estimate of the tumor location and boundaries that can help guide excision. Several research-grade navigation platform systems have been developed and tested for tumor localization.

One proposed approach is to use patient-specific, 3D printed molds created from preoperative imaging to help localize the tumor intraoperatively. A study with $N = 19$ BCS patients used a 3D printed, bra-like guide generated from preoperatively acquired supine MR imaging to inject blue dye around the tumor border for guidance during BCS [132]. This method was shown to be effective at transferring MR imaging cues to the surgeon. Another study used a similar method – a patient specific 3D printed guide from supine MR imaging was generated and used to trace the tumor outline shape onto the breast surface and inject blue dye [133]. The guide was also used to verify post-excision shape and volume. In $N = 88$ patients, 18.0% had positive margins after first-pass excision.

Rather than having a physical 3D printed object, another navigation platform strategy is to display tumor geometry in a virtual 3D scene space that is registered to the patient anatomy. This was done in a study that acquired preoperative supine MR imaging and then used optical tracking and optical scanning to rigidly register the segmented 3D tumor model to the patient in the OR, shown in Figure II.5 [8]. The surgeon then used tracked tools to mark the projected tumor boundary on the breast surface to guide excision. The effectiveness of this method was compared to wire-guided localization and was shown to significantly improve positive margin rates from 23% to 12% in a group of $N = 138$ patients. An additional navigation platform method utilized electromagnetic tracking with tracked ultrasound imaging, a tracked guide-wire needle, and a nav-

igation display screen [131]. A virtual 3D tumor model was generated from segmented tracked ultrasound imaging, and the tumor model moved relative to the tracked guide-wire needle throughout excision. This system was tested on breast phantom experiments and evaluated for feasibility in six BCS patients. One out of the six BCS patients had positive margins. This study cited breast deformations as a remaining challenge for achieving negative margins with their navigation system. This approach could be enhanced when combined with preoperatively acquired imaging, especially for use on sonographically occult lesions.

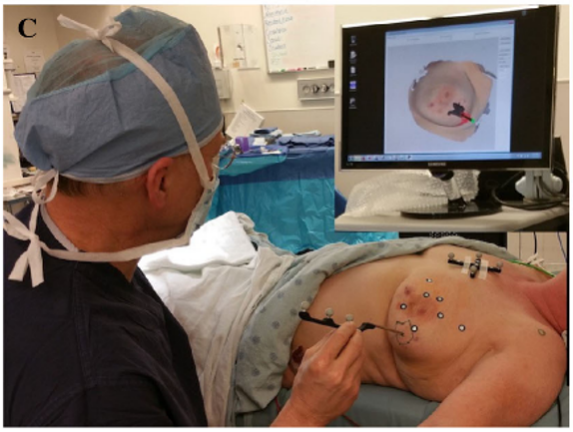

Figure II.5: The navigation platform proposed in Barth et al. showing the display monitor with 3D tumor, breast geometry, optically tracked skin fiducials, and a tracked stylus tool. Image reprinted from [8] with permission.

The interest in augmented reality (AR) as a potential surgical visualization tool has led researchers to explore AR for BCS as a navigation platform. In a proof-of-concept study with ten breast cancer patients, supine preoperative MR was acquired, and a 3D tumor model was segmented in the MR image. Prior to surgery, a HoloLens AR headset was used to display a rigidly registered hologram of the segmented breast tumor on the breast surface which was compared to the palpated location. Preliminary results showed effective rigid localization but noted discrepancies from nonrigid breast deformations [134]. A similar study also acquired supine MR imaging and used a HoloLens to visualize a 3D tumor model prior to the start of surgery. Preoperative planning with the HoloLens was compared to the standard-of-care planning using skin markings in one example case [135]. Another AR study used an implanted fiber optoacoustic guide seed combined with the HoloLens device for continuous visualization of the seed location. While this study showed accurate seed localization and was demonstrated in a cadaver study, this method is akin to seed-based methods with the AR device replacing the handheld probe, rather than a full navigation platform that visualizes tumor boundary and extent [136]. A fourth study compared localization accuracy between using a 3D-printed physical guide and an AR guide for tumor bracketing, and both guides had similar targeting accuracies. However, this comparison was only performed on a breast phantom, and the study noted errors from soft tissue deformations

[137]. While AR is an exciting new visualization tool, these methods have the potential to be improved by deformation correction methods to better align physical and imaging space, whether the imaging space is displayed in AR or on a traditional monitor.

Previous investigations into nonrigid registration deformation correction methods for BCS guidance include an approach that combined breast surface data and tracked ultrasound chest wall contours to retrospectively evaluate tumor position with nonrigid registration compared to ground-truth tracked ultrasound tumor position [138]. A later approach expanded this work by improving the nonrigid registration method to work with sparse-data sources that were specifically designed for intraoperative BCS data collection and guidance purposes [139]. While these works do propose nonrigid registration methods, they were not evaluated prospectively with active deformation correction in an intraoperative setting. The work in this dissertation aims to demonstrate active nonrigid deformation correction in a BCS-IGS system. Mechanics based breast deformation modeling methods, from which the nonrigid registration algorithm outlined in this work is derived, are reviewed in the next section.

II.4 Breast Biomechanical Modeling

II.4.1 Anatomy

Designating tissue composition and constitutive material properties is an important part of breast biomechanical modeling, and it requires detailed knowledge about the anatomy of the breast. The healthy breast is composed of multiple tissue types including skin, adipose tissue, glandular tissue, muscle, ligaments, and fascia. These tissues are organized in a heterogeneous fibro-adipose network that forms the structure and shape of the breast shown in Figure II.6. The first description of the suspensory ligaments in the breast is attributed to Sir Cooper in 1840, resulting in the name "Cooper's ligaments" [140]. A more recent anatomical dissection study notes that fascia layers including the superficial fascia and the pectoral fascia surround fibro-adipose tissue pockets that are located both anterior and posterior to the corpus mammae. The breast is positioned anterior to the pectoral muscles, and the boundary between muscle tissue and the fibro-adipose tissue is referred to as the chest wall [9]. The structure and makeup of the breast is also known to change composition over a woman's lifetime. Menstruation, pregnancy, breastfeeding, menopause, and hormone medications can all cause breast tissue property changes.

II.4.2 Material Properties

Understanding the material properties of the breast is critical for developing accurate biomechanical deformation models. Multiple studies, including ex vivo and in vivo measurement techniques, have been performed to characterize breast adipose, glandular, skin, muscle, and tumor tissue [141]. In the simplest linear-elastic

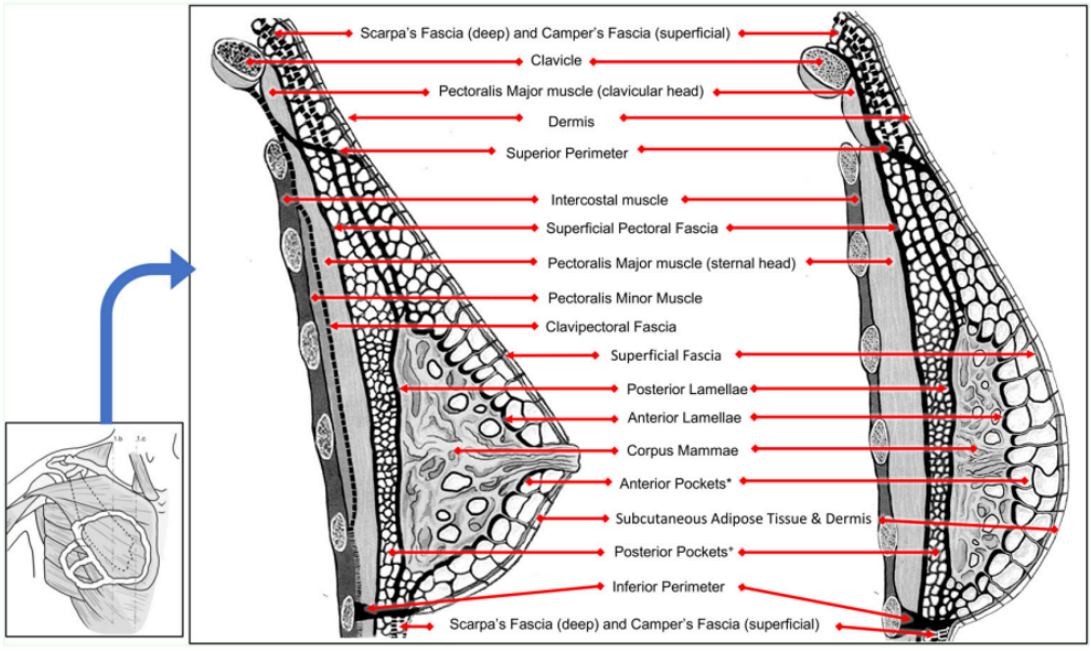

Figure II.6: Breast anatomy. Image reprinted from [9] with permission.

model, tissue can be represented by two material properties – the Young's Modulus value E, which quantifies a tissue's stiffness and is equal to the ratio between the imparted stress on object and the resulting axial strain, and the Poisson's ratio value ν which quantifies a tissue's compressibility and is equal to the negative of the ratio between transverse and axial strain. Biological tissue is generally regarded as nearly incompressible with Poisson's ratio values ranging between $0.45 < \nu < 0.49$ [142]. However, some have suggested that tissue's degree of compressibility is actually variable with values as low as $\nu = 0.3$ and changes in Poisson's ratio being an early indicator of disease [143]. Studies quantifying Young's Moduli values in breast tissue have also been variable. One ex vivo study that tested 38 adipose and 31 glandular tissue samples reported stiffness ranges of 18-22 kPa for adipose tissue and 28-35 kPa for glandular tissue at 5% preload compression [144]. Another study reported average stiffness values of 0.7 kPa for 33 adipose tissue samples and 0.8 kPa for 27 glandular tissue samples at a low stress range between 0-0.2 kPa [145]. Both studies were performed ex vivo with uniaxial compressive force tests.

The process of excising, preserving, and freezing tissue samples for material property testing may itself alter the measured properties. In vivo tissue measurement techniques are advantageous in that they maintain the surrounding environment, and patient-specific properties can be measured with pre-existing imaging modalities. One study quantified adipose and glandular tissue stiffness using ultrasound shear wave elastography and found average shear stiffness moduli values ranging between 4.7-5.0 kPa for adipose tissue and

6.5-6.7 kPa for glandular tissue [146]. MR elastography has also been used to generate high resolution elastogram maps of breast tissue stiffness, with one study from six healthy volunteers reporting average shear stiffness moduli values of 7.5 ± 3.6 kPa and 3.3 ± 1.9 kPa for glandular and adipose tissue measured with MR elastography [147]. Note that for both results, the Young's modulus and the shear stiffness modulus μ are related in a linear elastic material, $\mu = \frac{E}{2(1+\nu)}$. Computational reconstruction techniques have also been explored to characterize breast tissue stiffness with noninvasive excitation like gravity excitation [148]. This study estimated Young's moduli values of 0.2 ± 0.1 kPa and 2.8 ± 4.0 kPa for adipose and glandular tissue.

While many of the breast material property studies have focused on characterizing adipose and glandular tissue, there is also specific interest in Cooper's ligaments and fascia as a main factor influencing breast shape and structure. Both MR and ultrasound have been used to quantify the directional anisotropy in the breast caused by ligaments and fascia structures [149; 150]. A recent 2022 study characterized Cooper's ligaments material properties using uniaxial tensile tests of excised cadaver ligament specimens [151]. The study proposed an original anisotropic hyperelastic constitutive law that best fit the collected empirical data and concluded that Cooper's ligaments were 2-3 orders of magnitude stiffer than other breast tissues. This work suggests that deformation modeling approaches may benefit from incorporating the distinct material properties exhibited by Cooper's ligaments.

Like material property measurements, the exact constitutive model employed for modeling breast tissue is another source of variation in the literature. The linear-elastic constitutive model is the simplest. It represents the stress-strain relationship as a linear function with Hooke's Law, $\sigma = E\varepsilon$, where σ is stress, ε is strain, and E is Young's Modulus [152]. While simple and adequate for small deformations, the linear elastic constitutive law is thought to be less accurate under large strain and deformation conditions. The neo-Hookean hyperelastic constitutive model has a nonlinear stress-strain curve. For incompressible tissues, it can be written as $W = C_1(I_1 - 3)$ where W is the strain energy density, I_1 is the first invariant of the Cauchy-Green deformation tensor, and C_1 is the material property constant. The Mooney-Rivlin hyperelastic constitutive model is a more general case of the neo-Hookean model where (for an incompressible material) $W = C_1(I_1 - 3) + C_2(I_2 - 3)$ where I_2 is the second invariant of the Cauchy-Green deformation tensor and C_2 is a second material property constant [153]. Other nonlinear constitutive models include the Ogden and Arruda-Boyce models, but neo-Hookean and Mooney-Rivlin appear most frequently in the literature for modeling breast tissue.

The variation in constitutive models is demonstrated in Figure II.7, which compares the stress-strain curves for glandular and adipose tissue used in six different studies [1]. The six studies indicated by their first authors – Wellman, Samani, Krouskop, Bakic, Lorenzen, and Schnabel – leveraged a variety of constitutive models including linear, exponential, and neo-Hookean models [154; 155; 144; 156; 157; 158]. In a similar investigation, a comprehensive review by Eder et al. directly compared twelve different constitutive models

for breast deformations that had been previously proposed in the literature [159]. The twelve models included linear, piecewise-linear, exponential, Neo-Hookean, and Mooney-Rivlin constitutive models derived from ten different publications [144; 154; 160; 155; 161; 162; 163; 164; 165; 166]. Two models in particular – the model by Tanner et al. and the model by Rajagopal et al., both neo-Hookean constitutive models – had the best accuracy for modeling breast deformations caused by gravity [163; 165]. While nonlinear constitutive models are thought to better represent large breast tissue dynamics, it should be noted that incorporating nonlinear properties in FEM modeling increases computation time and requires iterative methods that may have instability or convergence issues. Given the variability in the literature, the choice of a constitutive model and material properties for breast mechanics based modeling should be evaluated depending on the application.

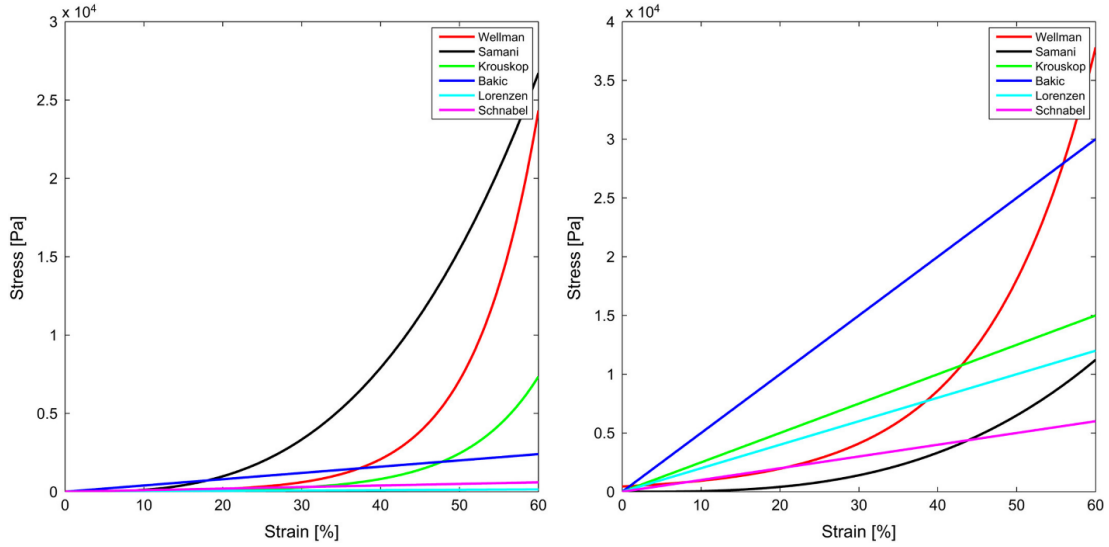

Figure II.7: Strain-stress relationship graphs showing the variability in glandular (left) and adipose (right) tissue properties used by multiple authors for breast biomechanical models. Image reprinted from [1] with permission.

II.4.3 Deformation Modeling Approaches

Mechanics based modeling utilizes the laws of continuum mechanics to predict nonrigid deformations in breast tissue subject to designated forces. These forces include external forces like changes in patient positioning relative to gravity or internal forces like pectoral muscle movement that causes tension in the connected breast fascia and ligaments [167]. While image guidance is one of the main applications for breast biomechanical models, these models have been used for other clinical and research purposes. Multi-modality fusion provides imaging information from multiple modalities for improved breast cancer detection. Since the loading conditions for different imaging systems vary – for example, in mammography the breast is com-

pressed between two plates and in MR imaging the breast is pendant – biomechanical models have been used to compensate for these different imaging positions to register images from different modalities [1]. Biomechanical models require three main components – (1) a geometric representation of the breast geometry and tissues, (2) constitutive material models that represent the mechanical response of different breast tissue types, and (3) designation of boundary loading conditions or forces that are acting on the breast [168]. Two of these three components have already been discussed. For (1), patient-specific representations of breast geometries are generated from breast imaging (Section II.1.3), and for (2), breast material properties and various constitutive models are selected from several reported methods (Section II.4.2).

For the third component, which involves designating loading conditions and computing a resulting deformation field, many of the biomechanical models implemented for breast use the finite element method (FEM). FEM is a numerical technique used to solve for a particular solution to a partial differential equation by discretizing the domain with a mesh composed of nodes and elements. For modeling deformations, FEM solves for a particular displacement solution to the Navier-Cauchy equations for a set of known boundary conditions. An aggregate summary of 12 papers that have used patient-specific breast FEM biomechanical models is presented in Table II.1 [169; 170; 171; 172; 173; 174; 175; 138; 176; 177; 178; 139]. This table is an updated and expanded version of a table presented in a review paper by García et al. [1]. As shown in the table, these FEM implementations vary in their complexity ranging from modeling breast tissue as one homogeneous volume to including 6 different tissue types (adipose, glandular, skin, muscle, ligaments, and fascia tissue). They also vary in their choice of mesh size, element type, and constitutive model. The wide variation in these methods suggest that engineering implementation decisions about model complexity should be made on a case-by-case basis depending on the application.

Hyperelastic constitutive models are more accurate when modeling biological tissue deformations under large strain conditions. Yet, linear-elastic models are used throughout this dissertation. As previously stated, modeling linear elasticity is less computationally expensive and more stable than nonlinear constitutive models. Model complexity is a limiting factor given the application in BCS and the goal of near real-time deformation correction. Also, several studies have shown that a linear elastic model has been sufficient for approximating breast deformations compared to nonlinear models, despite it being a less realistic model [171; 179; 180]. Tanner et al. compared displacement errors from several constitutive models and observed no significant difference between linear and nonlinear models, concluding that errors were much more dependent on perturbations to the boundary conditions and Poisson's ratio rather than the selected constitutive model [163].

Although FEM has been widely employed for various breast deformation modeling applications, it can be computationally expensive and relies on 3D mesh generation which can be cumbersome. Several mesh-

Table II.1: Summary of FEM modeling implementations detailing the study author, application, breast tissue types, mesh element types, and constitutive model. This table was updated and expanded from [1].

Author	**Application**	**Tissues**	**Mesh element type**	**Constitutive Model**
Tanner et al. 2011 [169]	Breast compression	Adipose, glandular	10-Node tetrahedrons	Linear
Han et al. 2011 [170]	Breast compression	Adipose, glandular, tumor	4-Node tetrahedrons	Neo-Hookean
Hsu et al. 2011 [171]	Breast compression	Adipose, glandular, skin	4-Node tetrahedrons	Linear
Lee et al. 2013 [172]	3D-2D registration	Breast volume	8-Node tetrahedrons	Neo-Hookean
Hopp et al. 2013 [173]	3D-2D registration	Breast volume	4-Node tetrahedrons	Neo-Hookean
Mertzanidou et al. 2014 [174]	3D-2D registration	Breast volume	4-Node tetrahedrons	Neo-Hookean
Solves-Llorens et al. 2014 [175]	3D-2D registration	Adipose, glandular, skin	4-Node tetrahedrons 3-Node tetrahedrons (skin)	Neo-Hookean
Conley et al. 2015 [138]	Image guided surgery	Breast volume	4-Node tetrahedrons	Linear (corotational)
García et al. 2017 [176]	3D-2D registration	Adipose, glandular	4-Node tetrahedrons	Neo-Hookean
Mîra et al. 2018 [177]	Gravity load	Adipose, glandular, skin, muscle, ligaments, fascia	4-Node tetrahedrons	Neo-Hookean
Xue et al. 2021 [178]	Prone-to-supine registration	Adipose, glandular, skin	8-Node hexahedrons	Neo-Hookean
Richey et al. 2022 [139]	Image guided surgery	Breast volume	4-Node tetrahedrons	Linear

free methods for modeling soft tissue deformations have been proposed as FEM alternatives. These include the moving least squares method, the element-free Galerkin method, and others [181]. While these methods have been used for modeling soft tissue deformations in several organs and for virtual surgery simulations, their direct use in breast modeling has been limited. Machine learning approaches have also been proposed as an FEM alternative, especially for applications where real-time deformation modeling is required. These approaches involve training machine learning models on results from FEM simulations. Demonstrations in breast deformation modeling include a method for predicting deformations from compression during mammography imaging and a method for predicting deformations caused by gravity from variations in patient positioning in one patient [182; 183]. In both applications, the proposed machine learning models' generalizability is limited. For [182], the model is not generalizable to new loading conditions outside of mammography compression, and for [183], the model is not generalizable to new patient geometries.

In summary, breast deformation modeling has been an active field of research for more than thirty years, and many different modeling approaches with various applications have been evaluated. The mechanics based breast deformation methods in the following chapters build upon previously proposed methods in the literature, with the aim of proposing a method specifically designed for use in a BCS-IGS system.

CHAPTER III

Methodology

This chapter provides an overview of the mechanics based methodology used in this work, including linear elasticity, transverse isotropy, the finite element method, and regularized Kelvinlet functions. It then describes the linearized iterative boundary reconstruction (LIBR) method for registration. Finally, methods regarding the BCS-IGS system implementation are discussed.

III.1 Linear Elasticity

Linear elasticity is a fundamental concept in continuum mechanics that can be used as an approximate model for soft tissue deformations [153]. The constitutive model governing linear elasticity can be represented using Hooke's Law written in matrix form,

$$\sigma = C\varepsilon \tag{III.1}$$

$$\varepsilon = S\sigma \tag{III.2}$$

$$\sigma = \begin{bmatrix} \sigma_{xx} \\ \sigma_{yy} \\ \sigma_{zz} \\ \sigma_{xy} \\ \sigma_{yz} \\ \sigma_{xz} \end{bmatrix} \qquad \varepsilon = \begin{bmatrix} \varepsilon_{xx} \\ \varepsilon_{yy} \\ \varepsilon_{zz} \\ \varepsilon_{xy} \\ \varepsilon_{yz} \\ \varepsilon_{xz} \end{bmatrix} \tag{III.3}$$

The vectors σ and ε are representations of the Cauchy stress tensor and the Cauchy strain tensor in engineering notation. The constitutive model can either be expressed using the material stiffness matrix C or the compliance matrix S, where $S = C^{-1}$.

A linear elastic isotropic material has no characteristic orientation and is defined by two material property parameters - Young's Modulus E which describes the stiffness of the material and is the slope of the linear stress-strain curve, and Poisson's ratio ν which describes the compressibility of the material and is the ratio of lateral to longitudinal strain in uniaxial tensile stress. The compliance matrix satisfying Equation III.2 for an isotropic linear elastic material can be written as,

$$S = \frac{1}{E}\begin{bmatrix} 1 & -\nu & -\nu & 0 & 0 & 0 \\ -\nu & 1 & -\nu & 0 & 0 & 0 \\ -\nu & -\nu & 1 & 0 & 0 & 0 \\ 0 & 0 & 0 & 1+\nu & 0 & 0 \\ 0 & 0 & 0 & 0 & 1+\nu & 0 \\ 0 & 0 & 0 & 0 & 0 & 1+\nu \end{bmatrix} \tag{III.4}$$

When following infinitesimal strain theory, the constitutive model equations above can be substituted into the linear momentum balance equation (also known as the Cauchy momentum equation from Newton's Second Law) to derive the Navier Cauchy displacement equations,

$$\frac{E}{2(1+\nu)}\nabla^2\mathbf{u} + \frac{E}{2(1+\nu)(1-2\nu)}\nabla(\nabla\cdot\mathbf{u}) + \mathbf{F} = 0 \tag{III.5}$$

where $\nabla^2\mathbf{u} = \nabla\cdot\nabla\mathbf{u}$, $\mathbf{u}$ is displacement, and $\mathbf{F}$ is a forcing vector. The Navier Cauchy equations are partial differential equations that describe the relationship between displacements and forces in an isotropic linear elastic domain at static equilibrium.

III.2 Transverse Isotropy

A transverse isotropic material is an anisotropic material that contains a plane of isotropy, meaning that the object can be rotated around one axis with no change to the object's elastic response. It is the simplest form of anisotropy, as it requires specifying material properties in one additional orthogonal direction. The directions are typically described as the longitudinal direction, sometimes called the fiber direction, and the transverse directions which are the two orthogonal directions spanning the isotropic plane. When the x direction is assumed to be the longitudinal direction and the y and z directions are the transverse directions, the compliance matrix satisfying Equation III.2 for an transverse isotropic linear elastic material can be written as,

$$S = \begin{bmatrix} \frac{1}{E_L} & \frac{-\nu_{LT}}{E_L} & \frac{-\nu_{LT}}{E_L} & 0 & 0 & 0 \\ \frac{-\nu_{TL}}{E_T} & \frac{1}{E_T} & \frac{-\nu_{TT}}{E_T} & 0 & 0 & 0 \\ \frac{-\nu_{TL}}{E_T} & \frac{-\nu_{TT}}{E_T} & \frac{1}{E_T} & 0 & 0 & 0 \\ 0 & 0 & 0 & \frac{1}{G_{LT}} & 0 & 0 \\ 0 & 0 & 0 & 0 & \frac{1}{G_{TT}} & 0 \\ 0 & 0 & 0 & 0 & 0 & \frac{1}{G_{LT}} \end{bmatrix} \tag{III.6}$$

$$\frac{-\nu_{LT}}{E_L} = \frac{-\nu_{TL}}{E_T}$$

$$G_{TT} = \frac{E_T}{2(1+\nu_{TT})}$$

where 5 unique properties need to be designated: E_T (Young's modulus transverse direction), E_L (Young's Modulus longitudinal direction), ν_{LT} (Poisson's ratio in the longitudinal direction), ν_{TT} (Poisson's ratio in the transverse directions), and G_{LT} (shear modulus) [153]. For simplification, G_{LT} can be assumed to be the harmonic mean of E_L and E_T [184]. The compliance matrix in Equation III.6 is defined with longitudinal and transverse directions aligned with the coordinate system. In practice, the local compliance matrix can be rotated to align to an arbitrary longitudinal vector direction by applying a rotation matrix.

III.3 Finite Element Method

The finite element method is a mathematical technique developed to solve partial differential equations like the Navier-Cauchy equations. It involves discretizing the domain into a geometric mesh containing volumetric elements designated as a list of vertices and edges. The displacements on a local element level are described using weighting functions, and the partial differential equations are enforced by leveraging the weighted residuals weak formulation. In a forward-solve problem, boundary conditions in the form of known displacements or forces are applied to the system to solve for a displacement field. When the effects from gravitational and body forces are assumed to be negligible, the Navier-Cauchy equations in Equation III.5 can be rewritten in a simplified form using the shear modulus coefficient G,

$$G = \frac{E}{2(1+\nu)}$$

$$\nabla \cdot G\nabla\mathbf{u} + \nabla\frac{G}{1-2\nu}(\nabla\cdot\mathbf{u}) = 0 \tag{III.7}$$

The solution to the simplified Navier-Cauchy equations in Equation III.7 is achieved using the Galerkin method of weighted residuals. The method begins with the volume integration of Equation III.7 using the spatially continuous weighting functions ϕ_i,

$$\left\langle \phi_i \nabla \cdot G\nabla\mathbf{u} \right\rangle + \left\langle \phi_i \nabla\frac{G}{1-2\nu}(\nabla\cdot\mathbf{u}) \right\rangle = 0 \tag{III.8}$$

where $\left\langle \cdot \right\rangle$ represents integration over the problem domain. ϕ_i is the ith member of the complete set of scalar position functions. In this work, linear Lagrange weighting functions - the standard C^o local Lagrange polynomial interpolants - are used with tetrahedral finite elements, although other element types and higher-order weighting functions can be substituted.

Applying integration by parts and Stokes' divergence theorem yields the weighted residual vector expression,

$$\left\langle G\nabla\mathbf{u}\cdot\nabla\phi_i \right\rangle + \left\langle \frac{G}{1-2\nu}(\nabla\cdot\mathbf{u})\nabla\phi_i \right\rangle = \oint \sigma_s\cdot\hat{n}\phi_i ds \tag{III.9}$$

where $\oint$ denotes the surface integral over the applied boundary stress σ_s acting on the enclosed domain boundary, and $\hat{n}$ is the outward-pointing unit normal direction on this boundary. Spatial discretization of the displacement solution $\mathbf{u}$ is also written using the Galerkin method, where the unknown displacement vector is represented as unknown coefficients multiplied by the weighting position functions,

$$\mathbf{u}(x) = \sum_j u_j\phi_j(x) \tag{III.10}$$

Substituting Equation III.10 into III.9 as the representation of $\mathbf{u}$ produces the set of ordinary differential equations,

$$\sum_j u_j\left\langle G\nabla\phi_j\cdot\nabla\phi_i \right\rangle + \sum_j u_j\cdot\left\langle \nabla\phi_j\frac{G}{1-2\nu}\nabla\phi_i \right\rangle = \oint \sigma_s\cdot\hat{n}\phi_i ds \tag{III.11}$$

Finally, Equation III.11 is associated with the finite element assembly process and can be rewritten in the conventional linear system of equations form,

$$K_{ij}\mathbf{u} = \mathbf{b}_i \tag{III.12}$$

where K_{ij} is the global stiffness matrix of size $3M$ x $3M$, $\mathbf{u}$ is the displacement vector of size $3M$, $\mathbf{b}_i$ is the forcing vector of size $3M$, and M is the number of mesh nodes. Boundary conditions can be prescribed in this form by setting direct values for $\mathbf{u}$ or $\mathbf{b}_i$. The resulting displacement vector $\mathbf{u}$ is computed by inverting the global stiffness matrix.

$$\mathbf{u} = K_{ij}^{-1}\mathbf{b}_i \tag{III.13}$$

III.4 Regularized Kelvinlet Functions

Section III.3 describes a numerical method to approximate a solution to the Navier Cauchy equations by discretizing the geometry. However, analytical solutions to the Navier Cauchy equations exist for simplified forcing functions and geometries. One such solution is the Kelvinlet (also known as Kelvin's state or Kelvin Solution), which is a fundamental solution of linear elasticity corresponding to a singular point load $\delta(\boldsymbol{x}-\boldsymbol{x}_0)$ applied to an infinite elastic space. Multiple techniques exist for solving for the Kelvinlet equation including

using Fourier transforms and using the Papkovich Neuber potentials [153]. The Papkovich Neuber potentials are three equations - a displacement field, harmonic vector potential, and harmonic scalar potential - that satisfy the Navier Cauchy equations from Equation III.5.

$$\mathbf{u}(\boldsymbol{x}) = \frac{2(1+\nu)}{E}\left[\Psi(\boldsymbol{x}) + \frac{1}{4(1+\nu)}\nabla(\Phi(\boldsymbol{x}) - \boldsymbol{x}\cdot\Psi(\boldsymbol{x}))\right] \tag{III.14}$$

$$\nabla^2\Psi(\boldsymbol{x}) = -\mathbf{F}(\boldsymbol{x}) \tag{III.15}$$

$$\nabla^2\Phi(\boldsymbol{x}) = -\boldsymbol{x}\cdot\mathbf{F}(\boldsymbol{x}) \tag{III.16}$$

By setting the forcing function $\mathbf{F}(\boldsymbol{x})$ equal to a scaled impulse response function such that $\mathbf{F}(\boldsymbol{x}) = \boldsymbol{f}\delta(\boldsymbol{x}-\boldsymbol{x}_0)$, particular solutions to Equations III.15 and III.16 can be computed using the established solution for Poisson's equations. Note that $\boldsymbol{r} = \boldsymbol{x}-\boldsymbol{x}_0$ and $r = \|\boldsymbol{r}\|$.

$$\Psi(\boldsymbol{x}) = \frac{1}{4\pi}\int_{\mathbb{R}_3}\frac{\boldsymbol{f}\delta(\boldsymbol{s}-\boldsymbol{x}_0)}{\|\boldsymbol{x}-\boldsymbol{s}\|}\,d\boldsymbol{s} = \frac{\boldsymbol{f}}{4\pi r} \tag{III.17}$$

$$\Phi(\boldsymbol{x}) = \frac{1}{4\pi}\int_{\mathbb{R}_3}\frac{\boldsymbol{x}\cdot\boldsymbol{f}\delta(\boldsymbol{s}-\boldsymbol{x}_0)}{\|\boldsymbol{x}-\boldsymbol{s}\|}d\boldsymbol{s} = \frac{\boldsymbol{x}\cdot\boldsymbol{f}}{4\pi r} \tag{III.18}$$

Equations III.17 and III.18 can be substituted into Equation III.14 and simplified to arrive at the Kelvinlet function, where the material parameter coefficients are $a = \frac{(1+\nu)}{2\pi E}$, $b = \frac{a}{4(1-\nu)}$, and I is the identity matrix.

$$\mathbf{u}(\boldsymbol{r}) = \left[\frac{a-b}{r}I + \frac{b}{r^3}\boldsymbol{r}\boldsymbol{r}^t\right]\boldsymbol{f} \tag{III.19}$$

Examining Equation III.19, displacements and displacement gradients are singular at the point forcing location $\boldsymbol{x}_0$. To address this, de Goes et al. proposed the regularized Kelvinlet function for digital sculpting purposes [19]. The regularized Kelvinlet function uses the "bump" forcing function in Equation III.20 as the point load, which was first proposed for solving the equations for Stokes flow [185]. Using the regularized forcing function with the Papkovich Neuber potentials from Equations III.14 - III.16 yields the regularized Kelvinlet function in Equation III.21, where $r_\varepsilon = \sqrt{r^2+\varepsilon^2}$ is the regularized distance, and ε is the regularization radial scale.

$$\mathbf{F}_\varepsilon(\boldsymbol{r}) = \boldsymbol{f}\left[\frac{15\varepsilon^4}{8\pi}\frac{1}{r_\varepsilon^7}\right] \tag{III.20}$$

$$\mathbf{u}_\varepsilon(\boldsymbol{r}) = \left[\frac{a-b}{r_\varepsilon} I + \frac{b}{r_\varepsilon^3}\boldsymbol{r}\boldsymbol{r}^t + \frac{a}{2}\frac{\varepsilon^2}{r_\varepsilon^3} I\right]\boldsymbol{f} \tag{III.21}$$

Regularized Kelvinlet functions can also be extended to affine loads by using a matrix-based load distribution instead of a forcing vector [19]. The locally affine regularized Kelvinlet function (Equation III.22) is derived from a 3x3 forcing matrix F, rather than a forcing vector $\boldsymbol{f}$.

$$\mathbf{u}_\varepsilon(\boldsymbol{r}) = -a\left(\frac{1}{r_\varepsilon^3} + \frac{3\varepsilon^2}{2r_\varepsilon^5}\right) F\boldsymbol{r} + b\left[\frac{1}{r_\varepsilon^3}(F + F^T + \mathrm{tr}(F)I) - \frac{3}{r_\varepsilon^5}(\boldsymbol{r}^T F\boldsymbol{r})I\right]\boldsymbol{r} \tag{III.22}$$

For a skew-symmetric matrix, the forcing matrix F can be represented by a vector $\boldsymbol{q}$ using the cross product operation. This simplifies Equation III.22 to a regularized Kelvinlet function that models twisting deformations.

$$\mathbf{u}_\varepsilon(\boldsymbol{r}) = -a\left(\frac{1}{r_\varepsilon^3} + \frac{3\varepsilon^2}{2r_\varepsilon^5}\right)\boldsymbol{q} \times \boldsymbol{r} \tag{III.23}$$

The resulting deformations from the regularized Kelvinlet functions in Equations III.21 and III.23 are visualized with varying ε values in Figure III.1. In this work, regularized Kelvinlet functions are distributed in a predetermined geometry on an object, and their displacement fields are superposed to result in a deformation field for registration. More information about regularized Kelvinlet functions and their use in breast registration is presented in Chapter V.

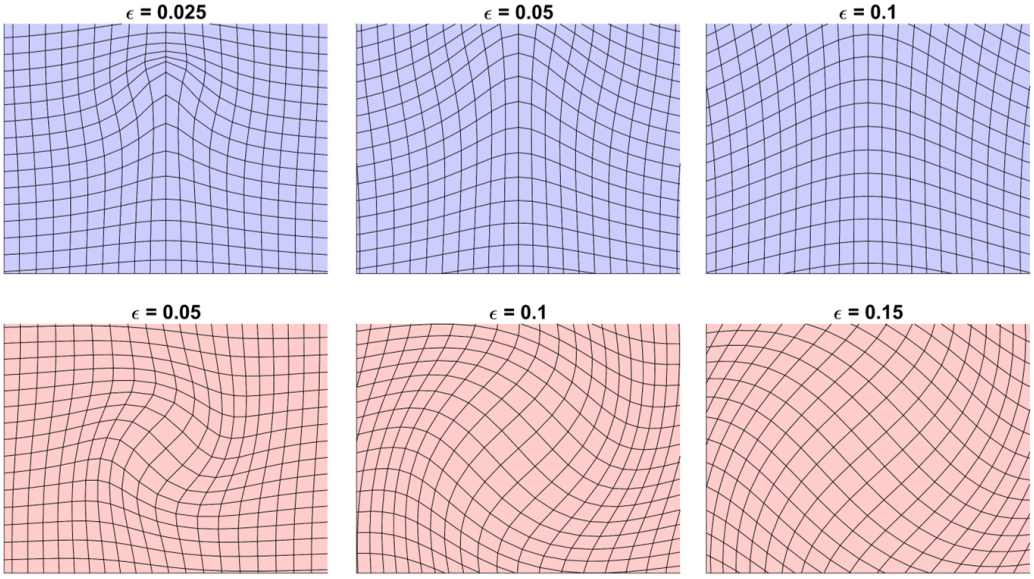

Figure III.1: Regularized Kelvinlet deformations from Equations III.21 (blue) and III.23 (red) with varying ε values. $E = 2100$ Pa and $\nu = 0.45$.

III.5 LIBR Method

The methods discussed thus far have described deformation modeling as a forward problem, where the forces acting on an object are known, and a mechanics based method (whether FEM or regularized Kelvinlet functions) is used to calculate resulting displacements. However, in many applications, the exact forces acting on an object are ambiguous. In BCS, breast deformations can be caused by arm motion and forces from the pectoral muscles, which are difficult to estimate directly. To address this, the mechanics based methods can be reframed as inverse problems that estimate the likely forces acting on an object that caused observed displacements. In this framework, observed displacements are used as model inputs. The observed displacements are partial, or sparse, measurements of the object geometry and subject to measurement noise. These sparse-data sources are used to solve for an optimal estimate of forces applied to the object. Solving for this force estimate provides a displacement vector field that can be applied to the entire object for registration.

Because the input data is sparse, there is an infinite set of forces that could result in displacement fields that satisfy the observed sparse data. The inverse problem is ill-posed, as the uniqueness criteria describing a well-posed problem is violated [186]. This means that to solve for an optimal set of forces, additional constraints must be imposed. In previous work, the linearized iterative boundary reconstruction (LIBR) method was proposed to constrain this inverse problem and solve for an optimal registration [20]. The LIBR method predefines a set of possible deformations, a displacement basis, intended to span likely object deformations. In the original LIBR algorithm, these displacements were computed using FEM from point load perturbations followed by Saint-Venant point load relaxation. In this work, they are computed using regularized Kelvinlet functions distributed on the object geometry. Using the principle of superposition, a deformation state can be linearized and estimated,

$$\tilde{\mathbf{u}} = J_u \boldsymbol{\alpha} \tag{III.24}$$

$$\tilde{\sigma} = J_\sigma \boldsymbol{\alpha} \tag{III.25}$$

$$\tilde{\varepsilon} = J_\varepsilon \boldsymbol{\alpha} \tag{III.26}$$

where $\tilde{\mathbf{u}}$, $\tilde{\sigma}$, and $\tilde{\varepsilon}$ are the displacement, stress, and strain estimates, J_u, J_σ, and J_ε are the displacement, stress, and strain response matrices, and $\boldsymbol{\alpha}$ is the weighting vector for the displacement bases (in this context, ε refers to strain, not the regularized Kelvinlet relaxation radius). To adapt the LIBR method for regularized Kelvinlet functions, the J matrices can be replaced with the Kelvinlet response matrices, where the matrix columns are composed of displacement, stress, and strain vectors calculated from unit forcing vectors for a set of regularized Kelvinlet functions.

Then, the optimal registration is iteratively computed as the linear combination of weighted displacement basis functions that minimizes the error between sparse data inputs and deformed model geometry. In addition to calculating the displacement basis function weights $\boldsymbol{\alpha}$, rigid registration parameters including translation $\boldsymbol{\tau}$ and rotation $\boldsymbol{\theta}$ are also computed. The $\boldsymbol{\alpha}$, $\boldsymbol{\tau}$, and $\boldsymbol{\theta}$ parameters are combined such that $\boldsymbol{\beta} = [\boldsymbol{\alpha}, \boldsymbol{\tau}, \boldsymbol{\theta}]$, and $\boldsymbol{\beta}$ represents the deformation state. Written in this form, the deformed model state $\boldsymbol{x}$ at every iteration can be calculated as,

$$\boldsymbol{x} = R(\boldsymbol{x}_0 - \bar{\boldsymbol{x}_0} + J_u\boldsymbol{\alpha}) + \boldsymbol{\tau} + \bar{\boldsymbol{x}_0} \tag{III.27}$$

where $\boldsymbol{x}_0$ is the original undeformed mesh, $\bar{\boldsymbol{x}}_0$ is the mesh centroid, and the rotation matrix R is defined from the $\boldsymbol{\theta}$ parameter $R(\boldsymbol{\theta}) = R(\theta_x)R(\theta_y)R(\theta_z)$.

The least squares objective function used to calculate the optimal $\boldsymbol{\beta}$ vector is shown in Equation III.28, and it contains two model-data error terms - e_{point} and $e_{surface}$. The e_{point} error is the model-data error for corresponding fiducial points. It is computed as the Euclidian distance between the input sparse data fiducial point y_i and the fiducial point in model space after the deformation state $\boldsymbol{\beta}$ is imposed, x_i. To calculate x_i, the deformed mesh vector $\boldsymbol{x}$ is calculated using Equation III.27, and the resulting displacements interpolated onto the original model space fiducial point location x_0. The $e_{surface}$ error term calculates the model-data error when exact point correspondence is unknown, but a model surface geometry is available. At each iteration, correspondence is established as the closest x_i point in $\boldsymbol{x}$ for every feature point y_i. Then, a sliding constraint is imposed such that the vector between x_i and y_i is projected onto the surface unit normal vector at x_i. This allows for sliding between the model surface and the sparse input data resulting in better alignment.

$$\Omega(\boldsymbol{\beta}) = \frac{1}{n_{point}} \sum_{i=1}^{n_{point}} (e^i_{point})^2 + \frac{1}{n_{surface}} \sum_{i=1}^{n_{surface}} (e^i_{surface})^2 + w_{SE}(e_{SE})^2 \tag{III.28}$$

In addition to the model-data error terms, a strain energy regularization term e_{SE} is included which penalizes deformations with large strain energies, and it is scaled by weight w_{SE}. e_{SE} is calculated at every iteration as the average strain energy of the deformation state in Equation III.29, where M is the number of mesh nodes.

$$e_{SE} = \frac{1}{2M}\boldsymbol{\alpha}^T(J_\varepsilon^T J\sigma)\boldsymbol{\alpha} \tag{III.29}$$

Levenberg-Marquardt optimization is used to iteratively solve for $\boldsymbol{\beta}$ at each iterative step k using the standard nonlinear least-squares form,

$$\boldsymbol{\beta}_{k+1} - \boldsymbol{\beta}_k = (J^T W J + \lambda \,\mathrm{diag}(J^T W J))^{-1} J^T W \boldsymbol{e} \tag{III.30}$$

where the error vector $\boldsymbol{e}$ is a concatenated vector of all e_{point}, $e_{surface}$, and e_{SE} terms. The Jacobian of the error J is analytically computed as $J = \frac{d\boldsymbol{e}}{d\boldsymbol{\beta}}$. λ is a trust region prediction ratio, and the termination criteria is set at $|\Delta\Omega(\boldsymbol{\beta})| < 10^{-12}$. More information about the LIBR method and its use with regularized Kelvinlet functions in breast registration are presented in Chapter V.

III.6 Image Guidance System Development

The BCS-IGS system was developed for bedside data collection and active deformation correction. It features a mobile cart with a display monitor, computer, extendable arm, and monitoring sensors. More details on the guidance system hardware are presented in Section VI.4.1.

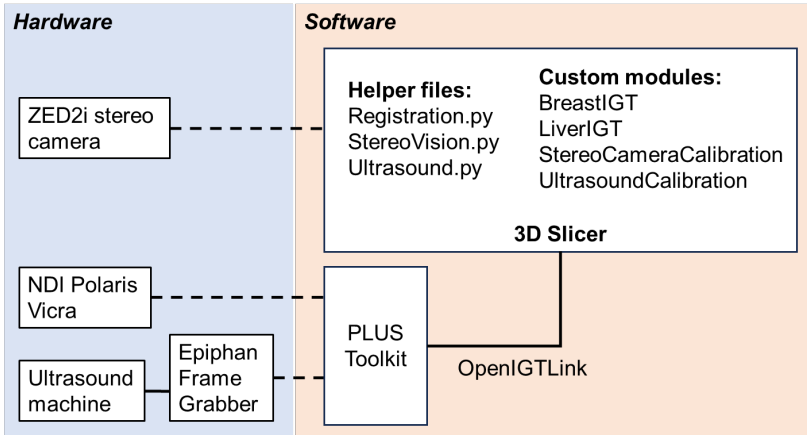

Figure III.2: System architecture diagram for the BCS-IGS system with hardware (blue) and software (orange) components.

The custom software for the guidance system module was developed as a scripted Python module for 3D Slicer v4.11. The system architecture for the BCS-IGS system is shown in Figure III.2. The software ecosystem features four modules so far – `BreastIGT` for the data collection and nonrigid registration presented in this dissertation, `LiverIGT` for guidance during hepatic surgeries, `StereoCameraCalibration` for calculating the co-registration calibration between optical tracker and stereo camera coordinate systems, and `UltrasoundCalibration` for calculating calibration matrices for tracked ultrasound. These modules load functionality saved in modular helper files so that capabilities can be easily shared between different modules. The helper files include `Registration.py` for executing rigid and nonrigid registrations, `StereoVision.py` for interfacing with the ZED stereo camera, and `Ultrasound.py` for interfacing with the ultrasound data. Functions in `StereoVision.py` directly control the ZED stereo camera through the PyZED API, unlike the other hardware devices that communicate through the PLUS Toolkit. All modules can be cloned through a Github Repository. The guidance system module's functionality is detailed in Section VI.4.2. The methods for the stereo camera calibration and ultrasound calibration modules are presented

below.

III.6.1 Stereo Camera Calibration

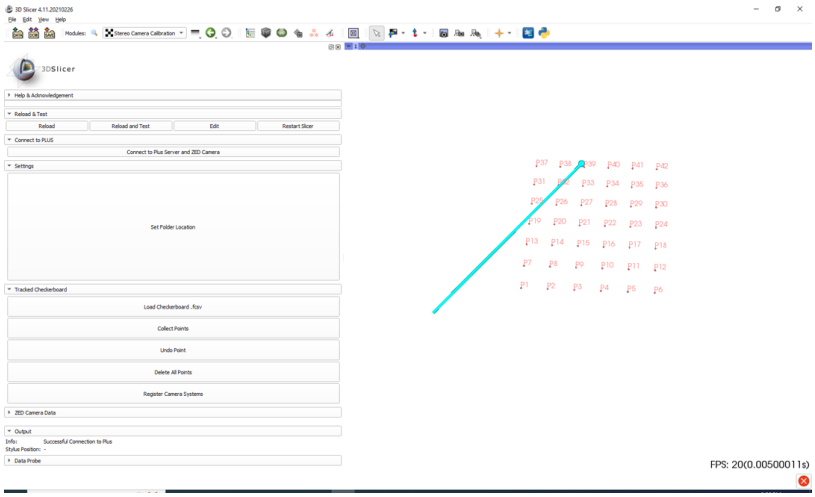

Figure III.3: Stereo camera calibration module in 3D Slicer.

The module for stereo camera and optical tracker co-registration is shown in Figure III.3. A tracked checkerboard calibration object was used for co-registration [187]. The calibration object was made from an aluminum plate with a 7x8 black and white checkerboard with 18 mm squares mounted to the plate surface. The aluminum plate had 4 machined mounts where passive optically reflective spheres were attached for optical tracking of the calibration object. For calibration, the checkerboard was placed in 10 positions at different tilts covering the field-of-view of the optical tracker and stereo camera. The module was used for simultaneous collection of the optically tracked calibration object position and stereo camera images in each of the 10 positions. In optical tracking space, the 42 internal checkerboard square intersects were tracked relative to the calibration object. In stereo camera space, the intersect points were identified in the left camera color image using OpenCV. The stereo camera calibration between the left and right cameras is set internally by the manufacturer. The PyZED API was used to convert left image pixel space to a 3D coordinate in stereo camera space. After collection at the 10 checkerboard positions, all collected points (420 for each space) were aggregated into point vectors q_O in optical tracking space and q_S in stereo camera space. Then, the calibration matrix ${}^{O}_{S}T$ was computed using conventional least-squares singular value decomposition point-based registration [188]. This resulted in a calibration matrix registering optical tracking and stereo camera spaces such that,

$$q_O = {}^{O}_{S}T \, q_S \tag{III.31}$$

Because the optical tracker and stereo cameras are rigidly mounted in a stable configuration, this process only needs to be performed once, barring adjustments to the sensor mounting. Calculating this calibration matrix allows for data collected with the stereo camera to be transformed into optical tracking space, and for both spaces to be co-registered in the breast guidance module.

III.6.2 Tracked Ultrasound

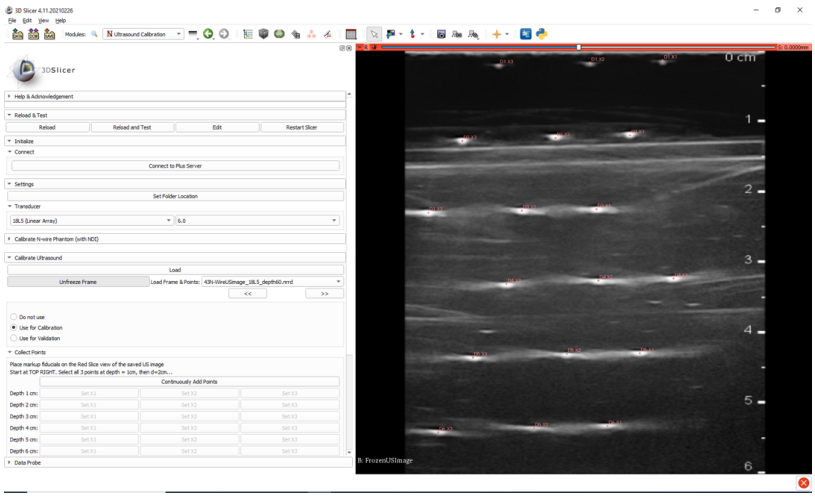

Figure III.4: Ultrasound calibration module in 3D Slicer.

The module for tracked US probe calibration is shown in Figure III.4. A custom US transducer case was designed and 3D printed to attach an optical tracking rigid body to the top of the transducer in a reproducible way (see Figure VI.1 from Chapter VI). The case was made to minimize line-of-sight problems from the rigid body to the optical tracker while also maintaining US probe functionality and usability. Tracked US calibration was performed using the N-wire calibration method [189]. This method requires two optically tracked rigid bodies – one attached to the US probe, and another attached to the N-wire calibration phantom. The N-wire calibration phantom contains wires threaded between two plates in distinct triangular patterns, such that the wire geometries are known relative to the attached rigid body. The phantom is submerged in water for US imaging. The calibration process includes (1) acquiring a US image, (2) manually labeling the wire intersect points visible in the image, and (3) computing the rigid transformation between image-labeled wire points and physical N-wire phantom points. Tracked ultrasound calibration was performed at 12 depths ranging from 3 - 9 cm to achieve the image-to-physical calibration matrix for each individual depth.

CHAPTER IV

Informing biomechanical breast modeling using supine magnetic resonance image registration

This chapter details Aim 1 of this dissertation, which is to utilize image-to-image registration of supine breast MR imaging to inform FEM breast modeling approaches. First, a supine MR imaging dataset that simulates surgical deformations from healthy volunteers is collected. Then, image-to-image registration between MR images acquired in different positions is performed. These registrations are used to examine tissue mechanical properties and infer FEM boundary conditions. Finally, three FEM breast modeling approaches are evaluated and compared – a homogeneous isotropic model, a heterogeneous isotropic model, and a heterogeneous transverse-isotropic model.

IV.1 Abstract

Simulating soft-tissue breast deformations is of interest for many applications including image fusion, longitudinal registration, and image-guided surgery. For the surgical use case, positional changes cause breast deformations that compromise the use of preoperative imaging to inform tumor excision. A biomechanical modeling approach to simulate supine breast deformations for surgical applications must be both accurate and computationally tractable. A supine MR breast imaging dataset from $N = 11$ volunteers was used to simulate surgical deformations by acquiring images in arm-down and arm-up positions. A diffeomorphic image registration method from the Advanced Normalization Tools (ANTs) repository was used to calculate deformation metrics (volume change and anisotropy) from the ANTs deformation field and derive biomechanical modeling boundary conditions. Then, three linear-elastic modeling approaches with varying levels of complexity (heterogeneity and anisotropy) were used to predict deformations caused by this arm motion. The average target registration error (TRE) after ANTs registration was 2.8 ± 1.3 mm (mean $\pm$ standard deviation). The mechanics-based deformation metrics revealed an overall anisotropic tissue behavior and a statistically significant difference in volume change between glandular and adipose tissue. These metrics were consistent with the biomechanical modeling results, which revealed a statistically significant improvement in TRE when using the heterogeneous anisotropic model compared to both the homogeneous and heterogeneous isotropic models ($p < 0.01$). While a model that fully incorporates all constitutive complexities of anatomical structure likely achieves the best accuracy, these image registration and biomechanical modeling methods may be of interest for predicting surgical deformations in the supine position.

IV.2 Contributions

This chapter is adapted from two publications, namely "Supine magnetic resonance image registration for breast surgery: Insights on material mechanics" published in the Journal of Medical Imaging, and "Incorporating Heterogeneity and Anisotropy for Surgical Applications in Breast Deformation Modeling" published in Clinical Biomechanics. These works have been reproduced with permission from the publishers.

[190]: M. J. Ringel, W. L. Richey, J. S. Heiselman, M. Luo, I. M. Meszoely, and M. I. Miga, "Supine magnetic resonance image registration for breast surgery: Insights on material mechanics," *Journal of Medical Imaging,* vol. 9, no. 6, pp. 065001, 2022.

[191]: M. J. Ringel, W. L. Richey, J. S. Heiselman, I. M. Meszoely, and M. I. Miga, "Incorporating Heterogeneity and Anisotropy for Surgical Applications in Breast Deformation Modeling," *Clinical Biomechanics,* vol. 104, pp. 105927, 2023.

IV.3 Introduction

Breast biomechanical modeling is of interest for multiple clinical and research applications. One use case is multi-modality image fusion, where biomechanical models are used to compensate for variable imaging positions when registering images from two or more modalities such as mammography imaging and magnetic resonance (MR) imaging [172; 174]. Another application is for longitudinal comparison, where alignment is needed to understand disease progression at different imaging timepoints [192; 193]. Additional relevant uses include employing biomechanical models for enhancing diagnostic information through elastography measurements and for predicting treatment responses [148; 194]. For all of the aforementioned applications, a breast biomechanical modeling approach that achieves accurate co-registration is required. However, the correct modeling implementation to optimally simulate breast deformations is unclear.

This work focuses specifically on the context of image-guided surgery, wherein preoperatively acquired breast MR imaging data informs tumor localization and excisions in breast conserving surgeries via image-to-physical alignment of preoperative and intraoperative breast anatomy [8; 138]. However, the primary confounding factor within this context is that the breast can undergo large nonrigid soft-tissue deformations between the imaging and intraoperative positions which can compromise the usability and accuracy of preoperative imaging for guidance purposes. With conventional MR imaging, this issue is especially problematic as breast MR imaging is typically acquired in the prone position with the breast pendant. However, during surgery, the patient lies supine with their arm abducted 90 degrees, which drastically deviates from the prone imaging position. Biomechanical models have been used for prone-to-supine registration to correct for these deformations, but the large scale of the tissue movement makes the approach quite challenging

[195; 196; 197]. MR imaging in the supine position has been explored as a solution to acquire imaging that more closely reflects the patient's positioning in the operating room [17]. However, even when imaging in the supine position, breast deformations caused by arm motion and repositioning still alter the breast geometry resulting in large image-to-physical misalignments [18]. Any soft tissue deformations that occur to the breast degrade the relevancy of preoperatively acquired imaging. Compensating for deformations in the supine position by using breast biomechanical modeling approaches may prove to be useful for informing surgical procedures, thus leading to more successful first-pass tumor excisions and improved patient outcomes.

In general, breast biomechanical modeling approaches consist of three conventional steps: (1) extracting breast geometric information to create a simulated breast model, (2) setting breast material properties to describe breast tissue's response to external forces, and (3) designating boundary conditions to model the loading forces applied to the breast [1]. These three components vary considerably in their implementations. For creating geometric breast mesh models, tetrahedral elements and hexagonal elements have been used with the finite element method (FEM) to model breast elasticity [173; 178]. Additionally, different tissue types in the breast have been designated in various modeling approaches. The simplest implementations model the breast as a homogeneous tissue like in Mertzanidou et al., while more complex models are heterogeneous like the model by Mira et al. with designated adipose, glandular, skin, muscle, ligaments, and fascia tissue types [174; 177]. For designating material properties, a linear elastic stress-strain relationship based on Hooke's Law has been used as a material property constitutive model for breast tissues. Nonlinear hyper-elastic models such as the Neo-Hookean and Mooney-Rivlin models have also been employed [1]. An implementation by García et al. featured a transverse-isotropic Neo-Hookean material model to simulate the effect of anisotropic Cooper's ligaments for breast MR and mammography co-registration [198]. Most breast tissue material models are derived using ex vivo tissue characterization with mechanical tests, but these can have wide variability in their measurement values[144; 145]. A recent breast tissue characterization study by Goodbrake et al. examined adipose and glandular tissue specimens and found that both tissue types displayed complex anisotropic behavior [199]. The third step, designating boundary conditions, varies depending on the application. For some applications, like for mammography compression between two plates or for prone to supine deformations caused by gravity, the boundary conditions are relatively straightforward [200]. However, repositioning from imaging unit to surgical configuration causes deformations that are a combination of internal body forces as well as changes to breast lateral support, and these deformations are non-trivial to implement in forward-solve problems [138]. Additionally, when combining these loading conditions with those that take place during surgery, the complexity of boundary conditions can rapidly escalate.

To address the challenge of assigning boundary conditions that accurately model surgical deformations, nonrigid image-to-image registration is used. Image registrations produce dense displacement mappings

between the moving and fixed images, which can be used to inform model boundary conditions and deformation characteristics with voxel-level specificity. The image registration method selected for this study was a symmetric diffeomorphic image-to-image registration algorithm with B-spline regularization available in the Advanced Normalization Tools (ANTs) repository [201]. Although many algorithms are available, this method in the ANTs repository was chosen because of its ease of use, ability to capture large deformations, and robustness in many different medical imaging applications. Along with inferring boundary conditions, the image registration deformation field is also used to analyze volume change and anisotropy for the entire breast and for adipose and glandular tissue independently to better understand the underlying material mechanics associated with breast deformations. This has an added benefit in that insights from the material mechanics measured from the image registration may be able to inform biomechanical modeling design. Material mechanics measured from the image registrations are presented alongside biomechanical modeling results in this work.

While many different breast biomechanical models have been proposed with varying levels of complexity, only a few studies have directly investigated how adding tissue heterogeneity and anisotropy affects modeling accuracy, and neither of these studies were performed in the supine position [170; 169]. While adding model complexity may improve realism by more accurately capturing physical effects, it may also introduce a model implementation that is more cumbersome and less applicable to a near real-time modeling approach for intraoperative surgical guidance. A quantitative assessment that addresses which additional modeling complexities have the largest effect on results would provide clinicians and researchers guidance for implementing biomechanical breast modeling approaches. Given the different tissue types in the breast, incorporating heterogeneity within breast models is quite logical. The breast also contains the suspensory ligament structure known as Cooper's ligaments, which are thought to significantly inform the breast's shape and structure. These ligaments range from 0.04–0.3 mm in diameter and are typically not resolved with conventional clinical breast imaging modalities [151]. However, given that the ligaments are embedded within the breast parenchyma, we hypothesize that modeling breast tissue as an anisotropic material may capture the composite effect that the Cooper's ligaments have on breast deformation.

Overall, the goal of this work is to address how heterogeneity and anisotropy affect modeling accuracy when incorporated into biomechanical models of breast deformation, while using image registration to inform model boundary conditions. This was investigated using a supine MR imaging dataset meant to mimic deformations caused by positional changes during surgery specifically for the image-guided surgery application. Biomechanical insights were extracted from the nonrigid image-to-image deformation field. Target registration error (TRE) was used to quantify accuracy and provide a data-driven evaluation of the potential performance improvement when using a heterogeneous, anisotropic model compared to a homogeneous,

isotropic model.

IV.4 Methods

The methods can be largely divided into four general steps: (1) MR image acquisition and preprocessing, (2) performing deformable image registration, (3) calculating registration-derived tissue mechanics-based metrics, and (4) implementing biomechanical modeling methods with varying levels of complexity. In summary, supine breast MR image volumes were acquired from healthy volunteers in arm-down and arm-up positions to simulate intraoperative deformations, and 3D anatomical models were generated from the image volumes. Then, registration between the arm-down and arm-up images was performed, and mechanics-based metrics were derived from these deformation fields. These deformation fields also provided the boundary conditions for the biomechanical models. Three biomechanical modeling approaches were implemented and evaluated - a homogeneous isotropic model (Model A), a heterogeneous isotropic model (Model B), and a heterogeneous anisotropic model (Model C).

IV.4.1 Image Acquisition and Preprocessing

Seven healthy adult women volunteers were enrolled in an MR imaging study approved by the Institutional Review Board at Vanderbilt University. Supine breast MR imaging was performed on the left and right breasts of seven healthy volunteers using a Phillips 3.0 Tesla closed bore scanner (Philips Healthcare, Best, The Netherlands) and a 16-channel torso coil. T1 High Resolution Isotropic Volume Excitation (THRIVE) sequence scans were obtained with one of two voxel sizes ($0.357\times0.357\times1$ mm^3 or $0.391\times0.391\times1$ mm^3) with the ipsilateral arm down by the torso to mimic preoperative positioning and with the ipsilateral arm up by the head to mimic intraoperative positioning. The field of view included the entire breast volume, and the primary image slice was acquired in the axial direction. While true intraoperative positioning usually extends the arm to a T-shape pose, the arm-up configuration represents a more challenging configuration that enables quantitative image-to-image comparison. Prior to imaging, 23-26 MR visible synthetic fiducials (IZI Medical Products, Owing Mills, MD, USA) were placed on the surface of each breast. Two out of the fourteen breast images were omitted due to imaging artifacts. For one subject, only the left breast was imaged leaving eleven ($N = 11$) breasts from seven individuals with ages ranging from 25 to 57 years included in the study.

3D breast volumes were manually segmented from the MR images along the boundary between the chest wall and breast parenchyma using ITK-SNAP. The surface fiducial markers were manually labeled and used as corresponding points in the mock preoperative and intraoperative positions. For each volunteer, 18-26 corresponding subsurface features were manually picked in the mock preoperative and intraoperative images for target evaluation by visual inspection of the glandular features in the breast. Target points were chosen

Table IV.1: Volunteer breast volume and glandular tissue percentage. Each Roman numeral denotes one volunteer with (a,b) indicating an individual breast.

Case	Volume (cm^3)	% Glandular
I	1198	4
II.a	701	9
II.b	682	9
III.a	672	36
IV	649	15
V	629	50
III.b	611	44
VI.a	596	60
VI.b	519	42
VII.a	444	32
VII.b	398	37
Mean ± std	*645 ± 208*	*31 ± 19*

so that they were evenly distributed throughout the breast mesh volumes. These subsurface target points were independent from the MR skin surface fiducial points. Breast tissue was labeled as either adipose or glandular tissue semi-automatically using Otsu thresholding with manual correction [202]. Volunteer breast segmentation volumes and glandular tissue percentages are reported in Table IV.1. After segmentation, 3D meshes in the arm-down position with 2 mm edge length tetrahedral elements were generated for the FEM modeling complexity experiments. The breast meshes were created based on the segmentation volumes using a marching cubes algorithm with custom mesh generation software [203]. To create a heterogeneous mesh, elements were classified as either adipose or glandular tissue based on each element's centroid location. The interfaces between adipose and glandular tissue mesh elements were treated the same as all other internal mesh interfaces. These data preprocessing steps are shown in Figure IV.1.

IV.4.2 Image Registration

After data preprocessing, 3D image-to-image registration that registered the arm-down and arm-up MR images was performed. This approach registered the mock preoperative and intraoperative images using a symmetric diffeomorphic image registration algorithm with explicit B-spline regularization available in the ANTs repository [201]. Images were masked using a dilated breast volume segmentation mask so that the MR visible fiducials were included in the masked volume. The registration was initialized with a rigid point-based registration calculated from the surface fiducials using a conventional least-squares singular value decomposition point-based registration method [188]. This was followed by the deformable B-spline symmetric normalization method. Registration was performed using multi-threading on 2.3 GHz Intel Xeon (E5-4610 v2) CPUs. The optimal parameters used for ANTs registration are reported in Table IV.2.

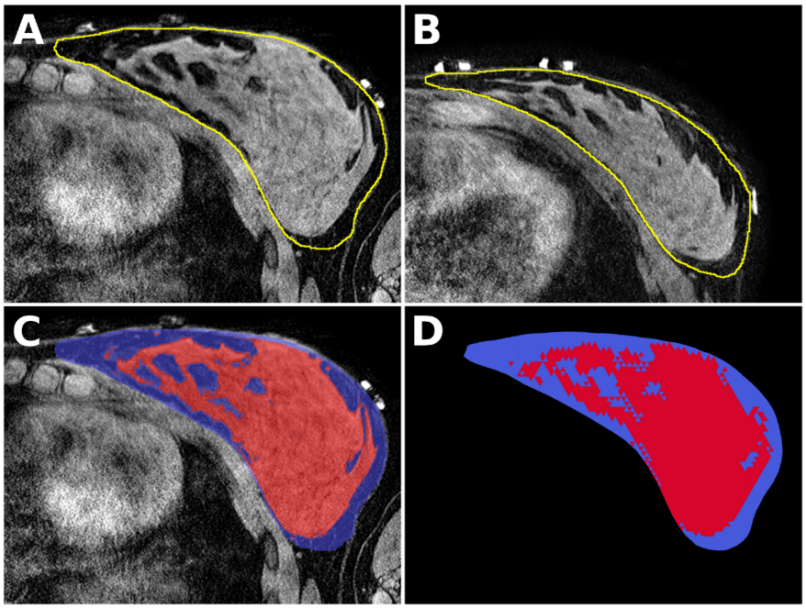

Figure IV.1: MR breast data preprocessing. (A–B) Axial slices of the arm-down (A) and arm-up (B) images with manual segmentation contours. (C) Segmentation of adipose tissue (blue) and glandular tissue (red). (D) Segmentation after mesh discretization.

Table IV.2: ANTs registration parameters.

Parameter	Value
ANTs Script	antsRegistrationSyN.sh
Initialization	Rigid point-based registration
Stages	Deformable b-spline symmetric normalization
Similarity metric	Cross-correlation
Multiresolution sampling levels	5
Histogram bins	32
Histogram matching	Yes
Spline distance	26
Gradient step size	0.1

IV.4.3 Evaluation of Registration Accuracy

The resulting deformations from either the image registration deformation fields or biomechanical modeling deformation fields were applied to the preoperative skin fiducials or the subsurface targets and compared to their ground truth imaging locations to measure accuracy. These accuracy measures were formulated as fiducial registration error (FRE) and target registration error (TRE). FRE was calculated as the root mean squared error between corresponding deformed and ground-truth fiducial points,

$$\text{FRE} = \sqrt{\frac{1}{N}\sum_{i=1}^{N} FRE_i^2} \tag{IV.1}$$

where FRE_i is the distance between the deformed i^{th} fiducial and the corresponding i^{th} intraoperative (ground-truth) fiducial. Similarly, TRE was calculated as the root mean squared error between deformed and ground-truth target points,

$$\text{TRE} = \sqrt{\frac{1}{N}\sum_{i=1}^{N} TRE_i^2} \tag{IV.2}$$

where TRE_i is the distance between the deformed i^{th} target and the corresponding intraoperative (ground-truth) i_{th} target.

IV.4.4 Image Registration-based Tissue Characterization

Mechanics-based metrics representing volume change and directional preference in volume change were calculated as a means of interpreting the ANTs deformation field as described in Amelon et al. and utilized for breast in Jahani et al. [204; 205]. The Jacobian determinant index (J) to measure volume change and the anisotropic deformation index (ADI) to measure anisotropy were computed using the following formulas,

$$J = \lambda_1\lambda_2\lambda_3 \tag{IV.3}$$

$$ADI = \sqrt{\left(\frac{\lambda_1-\lambda_2}{\lambda_2}\right)^2 + \left(\frac{\lambda_2-\lambda_3}{\lambda_3}\right)^2} \tag{IV.4}$$

where λ are the eigenvalues, or the principal stretches, of the deformation gradient tensor with $\lambda_1 > \lambda_2 > \lambda_3$ for material that has anisotropic behavior in all 3 principal directions and $\lambda_1 = \lambda_2 = \lambda_3$ for isotropic materials. $J < 1$ indicates volume contraction, $J = 1$ indicates no volume change, and $J > 1$ indicates volume expansion. $ADI = 0$ indicates isotropic deformation and $ADI > 0$ indicates increasingly anisotropic deformation [204]. J and ADI were calculated at every element in the breast mesh using the data provided by the ANTs deformation field. The metrics were averaged within segmented adipose tissue and within segmented glandular tissue. Average metrics were compared across tissue types using paired t-tests ($\alpha = 0.05$).

IV.4.5 FEM Modeling Implementation

Linear-elastic FEM models with varying levels of complexity were used to predict deformations caused by the arm-down to arm-up positional change. While more sophisticated nonlinear models exist, the selection of a linear model was made as it balances accuracy with computational tractability. The boundary condition designation methods, three model implementations, and model experimentation are detailed in the sections below.

FEM Boundary Condition Designation

Designating boundary conditions for biomechanical modeling is challenging, especially when deformations are caused by variable sources such as the deformations imparted by arm motion. To address this challenge, the same intensity-based nonrigid image-to-image registration method described in Section IV.4.2 above was used to establish correspondence between the arm-down and arm-up positions. After registration, displacement boundary conditions extracted from the image-to-image registration field were enforced on the entire mesh boundary for FEM modeling. This was done by interpolating the resulting displacement field after registration onto the mesh boundary nodes. These displacement vectors were enforced as Dirichlet boundary conditions for FEM modeling comparisons. Displacements at the boundary of the biomechanical model were defined to exactly match the estimates from the nonrigid image-to-image registration. Boundary conditions were applied to all boundary mesh nodes as shown by the segmentation contours in Figure IV.1. Although this undoubtedly has some degree of error, each modeling approach being investigated is provided with equivalent boundary conditions derived using this method. This allows for quantitative evaluation of the impact of the changes to constitutive relationships.

Model A – Homogeneous Isotropic Linear Elastic Model

The simplest elastic model employed was Model A —a homogeneous isotropic FEM model. This FEM model utilized the Galerkin method of weighted residuals with linear Lagrange basis functions to solve for a displacement solution governed by the Navier Cauchy equations for linear elasticity. This model represented all breast tissue as one tissue type and did not incorporate directional variation in the material property constitutive model. It is not necessary to define a Young's Modulus value for this model because the entire mesh boundary is defined by Dirichlet boundary conditions. This implementation was used as a baseline comparator for Model B and C implementations.

Model B – Heterogeneous Isotropic Linear Elastic Model

The next model employed was Model B —a heterogeneous isotropic FEM model with two different tissue types (adipose and glandular tissue) that were incorporated for heterogeneity. Since the mesh boundary nodes are defined by Dirichlet boundary conditions (rather than applied stress), only the relative stiffness between adipose and glandular tissue affects the displacement solution. This glandular-to-adipose stiffness ratio is defined as,

$$R_1 = \frac{E_{Glandular}}{E_{Adipose}} \tag{IV.5}$$

where $E_{Adipose}$ and $E_{Glandular}$ are the Young's Moduli values for adipose and glandular tissue.

Model C – Heterogeneous Anisotropic Linear Elastic Model

The last comparator model employed was Model C —a heterogeneous transverse-isotropic FEM model. Transverse isotropy is defined by a plane of isotropy where material properties are symmetric (in transverse directions) and a direction normal to the plane of isotropy where the material properties vary (in the longitudinal direction). The linear stress-strain relationship can be written such that $\varepsilon = S\sigma$, where S is the compliance matrix and ε and σ are the strain and stress tensors, respectively. This relationship can be written as,

$$\begin{bmatrix} \varepsilon_{xx} \\ \varepsilon_{yy} \\ \varepsilon_{zz} \\ \varepsilon_{xy} \\ \varepsilon_{yz} \\ \varepsilon_{xz} \end{bmatrix} = \begin{bmatrix} \frac{1}{E_L} & \frac{-\nu_{LT}}{E_L} & \frac{-\nu_{LT}}{E_L} & 0 & 0 & 0 \\ \frac{-\nu_{TL}}{E_T} & \frac{1}{E_T} & \frac{-\nu_{TT}}{E_T} & 0 & 0 & 0 \\ \frac{-\nu_{TL}}{E_T} & \frac{-\nu_{TT}}{E_T} & \frac{1}{E_T} & 0 & 0 & 0 \\ 0 & 0 & 0 & \frac{1}{G_{LT}} & 0 & 0 \\ 0 & 0 & 0 & 0 & \frac{1}{G_{TT}} & 0 \\ 0 & 0 & 0 & 0 & 0 & \frac{1}{G_{LT}} \end{bmatrix} \begin{bmatrix} \sigma_{xx} \\ \sigma_{yy} \\ \sigma_{zz} \\ \sigma_{xy} \\ \sigma_{yz} \\ \sigma_{xz} \end{bmatrix} \tag{IV.6}$$

$$\frac{-\nu_{LT}}{E_L} = \frac{-\nu_{TL}}{E_T} \tag{IV.7}$$

$$G_{TT} = \frac{E_T}{2(1+\nu_{TT})} \tag{IV.8}$$

where 5 unique properties need to be designated to properly characterize the material: E_T (Young's modulus transverse direction), E_L (Young's Modulus longitudinal direction), ν_{LT} (Poisson's ratio in the longitudinal direction), ν_{TT} (Poisson's ratio in the transverse directions), and G_{LT} (shear modulus) [153]. In Equations IV.6-IV.8, the longitudinal direction is oriented along the x-axis. To reduce the number of degrees of freedom, G_{LT} was assumed to be the harmonic mean of E_L and E_T which is consistent with a previous implementation of a transverse-isotropic model [184]. This simplified the number of independent material properties characterizing stiffness to two Young's Moduli values, namely E_L and E_T. The longitudinal-to-transverse isotropic stiffness ratio is defined as,

$$R_2 = \frac{E_L}{E_T} \tag{IV.9}$$

The relationship in Equation IV.6 implies that the direction of longitudinal property difference is known at the local tissue element level. Based on a general structural anatomy associated with breast parenchyma and Cooper's ligaments, the longitudinal direction for each mesh element was designated as the unit vector normal to the segmented chest wall surface. The longitudinal directions and boundary conditions are visualized in Figure IV.2.

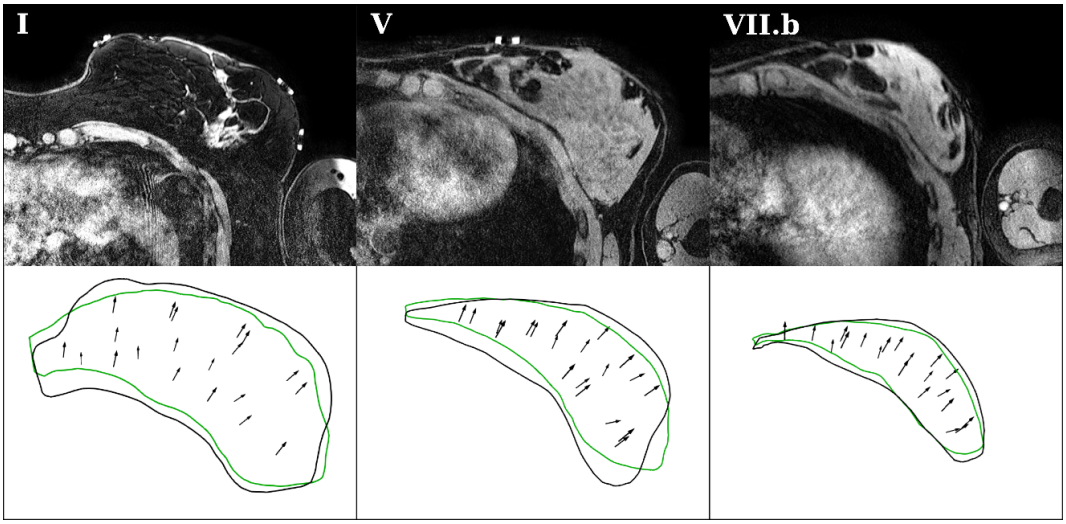

Figure IV.2: Boundary conditions and anisotropic longitudinal directions. (Top) Axial slices for three representative cases - I, V, and VII.b. (Bottom) 2D views of the arm-down mesh outline (black contours), the longitudinal directions for the transverse-isotropic model (black arrows), and the arm-down mesh outline deformed into arm-up position using image-to-image registration (green contours). The displacements between the green and black contours were implemented as boundary conditions.

FEM Modeling Experimentation

Logarithmic parameter sweeps were used to investigate the effects of heterogeneity (R_1) in Model B and the effects of heterogeneity and anisotropy (R_1 and R_2) in Model C. The parameter sweep of R_1 values was $R_1 = \{2^{-4}, 2^{-3}, 2^{-2}, 2^{-1}, 2^0, 2^1, 2^2, 2^3, 2^4\}$, and this parameter sweep was used for both Models B and C. The parameter sweep of R_2 values was $R_2 = \{2^1, 2^4, 2^7\}$, and this parameter sweep was used for Model C. For Models A and B, the Poisson's ratio was $\nu = 0.45$ to model soft tissue as nearly incompressible based on previous modeling implementations [139; 190]. For Model C, the Poisson's ratios in both directions were $\nu_{LT} = \nu_{TT} = 0.45$ to reduce the number of degrees of freedom and model nearly incompressible tissue.

Measuring TRE provided a quantitative model accuracy measurement that was compared for the models across the parameter sweeps. For Model B, the R_1 parameter value that resulted in the lowest TRE was selected for each individual case. For Model C, the lowest R_1 and R_2 parameter combination that resulted in the lowest TRE was selected for each individual case. Significance testing was performed using paired Wilcoxon signed-rank tests on TRE values across all 11 cases to test for a statistically significant difference in performance when using Models A–C at a significance level of $\alpha = 0.01$ [206].

IV.5 Results

IV.5.1 Image Registration Results

The average of the root mean squared error FRE values across all breasts was 3.1 $\pm$ 1.1 mm after ANTs image registration (mean $\pm$ standard deviation). When compared to rigid registration, ANTs resulted in a 60% improvement in FRE ($p < 0.001$). The average of the root mean squared error TRE values across all breasts was 2.8 $\pm$ 1.3 mm after ANTs image registration (mean $\pm$ standard deviation). When compared to rigid registration, ANTs resulted in a 73% improvement in TRE ($p < 0.001$). ANTs registration took 7.4 hours on average for each case and would not be feasible for real-time applications.

The ANTs image registration results and deformation field were further analyzed for insights into breast deformation patterns. Subsurface target distributions and errors from three example cases are shown in Figure IV.3A. The target locations were distributed evenly throughout the breast volume. The maximum target errors were 1.7 mm, 6.6 mm, and 5.9 mm for the low (VII.b), medium (V), and high (I) volume example cases, respectively. For all 237 targets aggregated across the $N = 11$ cases, the average absolute error in the inferior-superior direction was slightly yet significantly higher than in the medial-lateral and anterior-posterior directions ($p < 0.05$). This result is likely because the inferior-superior direction corresponds to the image acquisition direction with the larger voxel dimension. There were no observable correlations between error directionality and anatomical target location. The mesh deformations generated from the ANTs image registration are shown in Figure IV.3B as the signed deformation distance on the mesh surface. In the coronal view, outward extension was seen in the upper outer quadrant and inward compression was seen around the nipple although there was variation in different cases. Overall, the ANTs image registration deformation revealed stretching in the superior-inferior direction and flattening in the anterior-posterior direction occurring with arm-down to arm-up motion. While qualitative, the results agree with anticipated behavior.

Image registration was also evaluated by comparing deformed and ground truth image volumes shown in Figure IV.4A. The glandular features were similar in corresponding axial slices of the deformed and target image volumes indicating an accurate image registration. Example images are shown with four targets from four different cases. For each quartile, one target is shown with error within 0.1 mm of the quartile median target error. Although the 4th quartile target shown has a larger error distance, the glandular image features in the deformed and target images still show strong agreement. 75% of all target errors were below 3 mm as shown in the histogram in Figure IV.4B, implying that the ANTs image registration was accurate throughout the image volume for all cases.

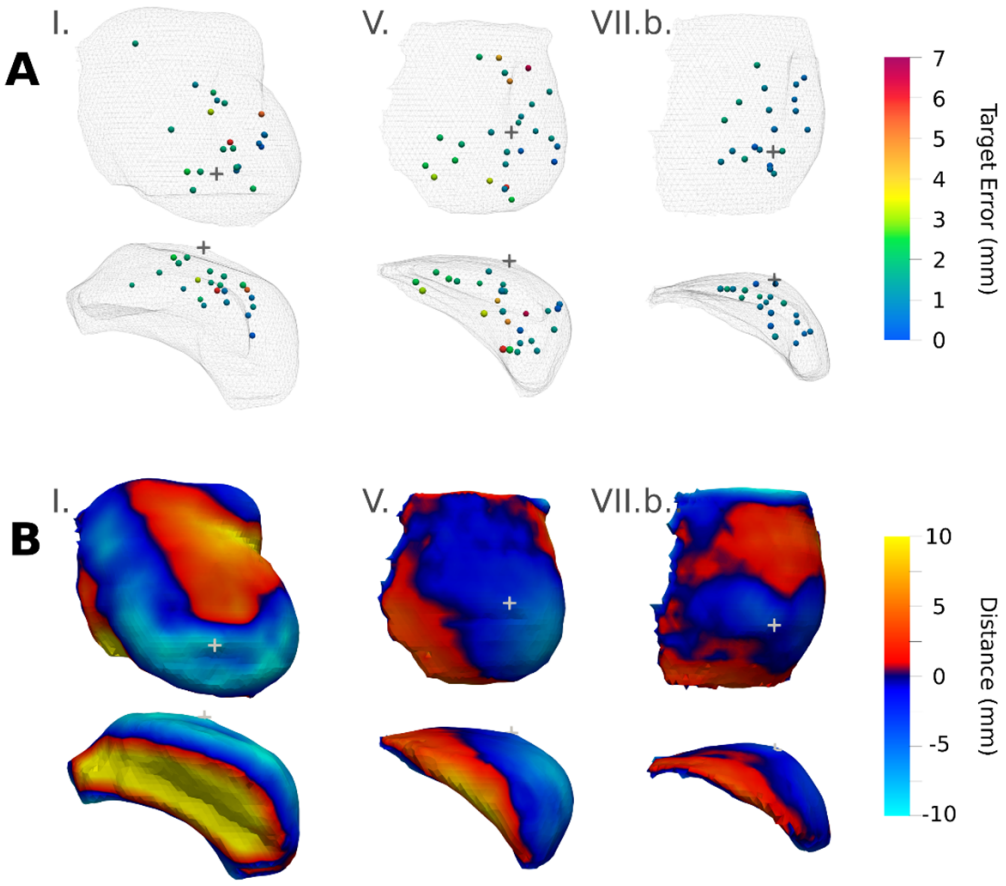

Figure IV.3: ANTs image registration results from a large (I), medium (V), and small (VII.b.) breast volume case displayed on coronal (top) and axial (bottom) views of breast meshes with a gray cross marking the nipple location. (A) Spheres indicate subsurface target locations and are colored according to individual target error. (B) Mesh color indicates the signed distance from ANTs image registration deformation moving from arm-down to arm-up with warm colors representing outward surface extension and cool colors representing inward surface compression.

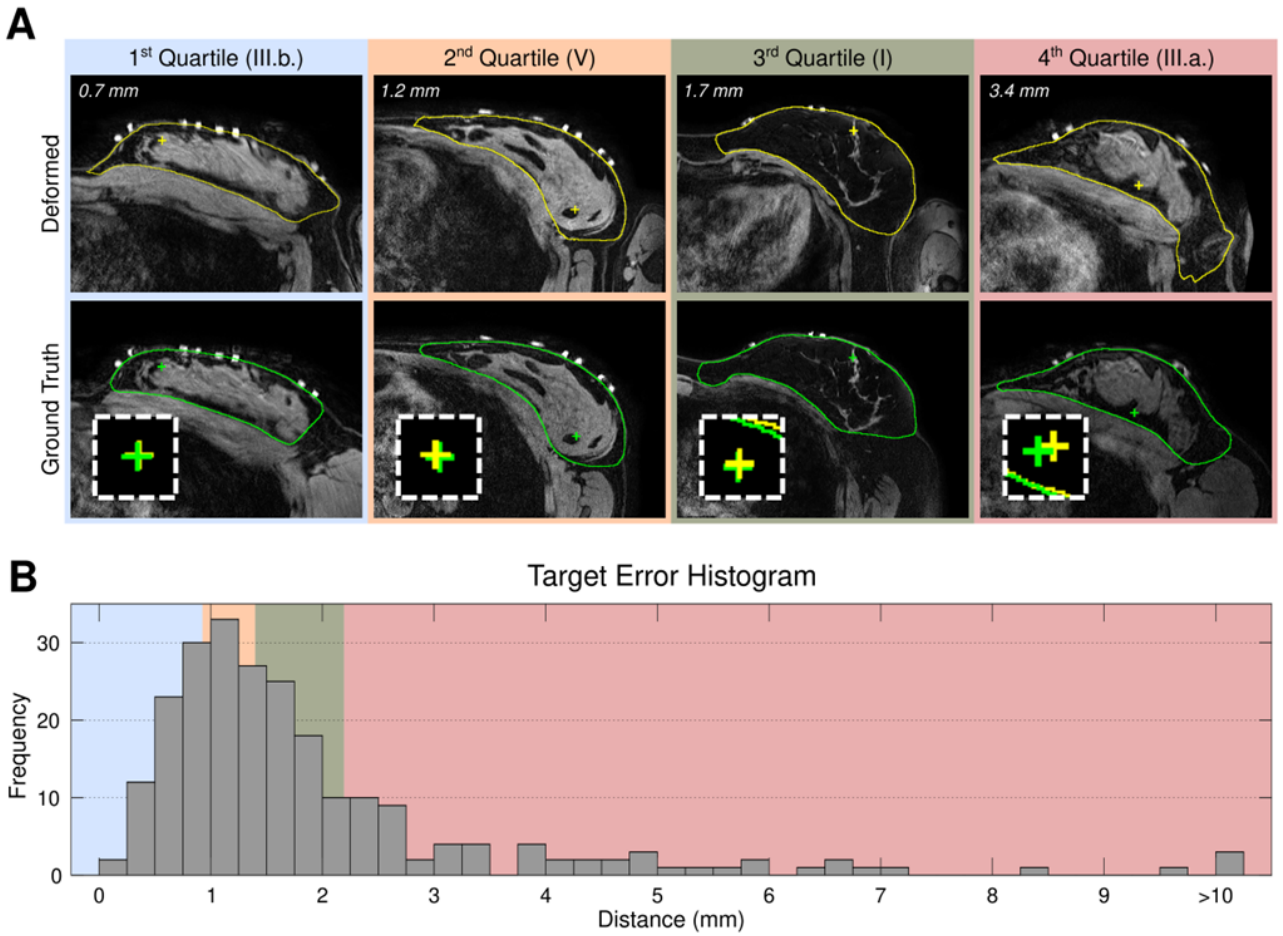

Figure IV.4: Target error distribution and image results from ANTs registration. (A) Registration results from four cases where axial slices show a target with error within 0.1 mm of the median target error of each quartile. The deformed image segmentations and targets are in yellow (top), and the ground truth image segmentations and targets are in green (bottom). The insert shows axial projections of the overlayed deformed and ground truth targets. (B) Target error histogram of 237 subsurface targets from all cases with quartiles shown in blue, yellow, green, and red.

IV.5.2 Tissue Characterization Results

The average eigenvalues, or principal stretches, of the deformation gradient tensor computed at each mesh element deformed by the ANTs deformation field and stratified by tissue type are reported in Table IV.3. These average eigenvalues suggest that the breast exhibits orthotropic behavior and that the three eigenvalues vary in magnitude. There is also consistency in the eigenvalue magnitudes exhibited across all $N = 11$ cases.

Table IV.3: Average eigenvalues from the deformation gradient tensor for adipose and glandular tissue.

Case	λ_1		λ_2		λ_3	
	Adipose	Glandular	Adipose	Glandular	Adipose	Glandular
I	1.27	1.54	0.98	0.96	0.76	0.70
II.a	1.28	1.42	0.97	0.99	0.78	0.74
II.b	1.27	1.52	0.97	0.94	0.78	0.71
III.a	1.23	1.20	1.01	1.01	0.81	0.82
IV	1.31	1.46	1.00	1.01	0.72	0.69
V	1.32	1.35	0.99	1.00	0.71	0.73
III.b	1.29	1.37	0.97	0.99	0.73	0.74
VI.a	1.38	1.40	0.99	1.00	0.70	0.72
VI.b	1.31	1.37	0.97	1.00	0.73	0.75
VII.a	1.30	1.31	1.04	1.04	0.73	0.75
VII.b	1.27	1.28	1.00	0.99	0.74	0.81
Mean ± std	*1.29 ± 0.04*	*1.39 ± 0.10*	*0.99 ± 0.02*	*0.99 ± 0.03*	*0.74 ± 0.03*	*0.74 ± 0.04*

The distribution of the average J and ADI values computed from the ANTs deformation field and stratified by tissue type are shown in Figure IV.5, and the metric values for each individual case are reported in Table IV.4. The average J value for adipose tissue was 0.96 ± 0.02 across all cases (mean $\pm$ standard deviation). Comparatively, the average J value for glandular tissue was 1.01 ± 0.02, which was slightly yet statistically significantly higher than adipose tissue ($p < 0.001$). This difference indicates that on average, ANTs predicted a minor contraction of adipose tissue and a minor expansion of glandular tissue during the deformation from arm-down to arm-up positions. The average ADI value for adipose tissue was 0.54 ± 0.09 across all cases, and the average ADI value for glandular tissue was 0.60 ± 0.15 (mean $\pm$ standard deviation). There was no statistically significant difference in ADI value between adipose and glandular tissue ($p = 0.23$). This finding suggests that ANTs registration predicts both tissue types to have anisotropic behavior.

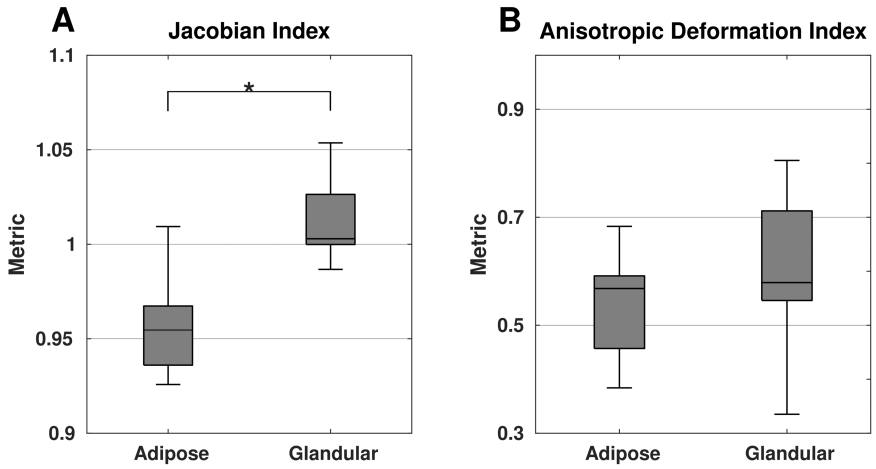

Figure IV.5: Distribution of average (A) Jacobian - J and (B) Anisotropic Deformation Index - ADI values for adipose and glandular tissue calculated from the ANTs deformation field. Whiskers represent minimum and maximum index values. Statistical significance is denoted with asterisks ($J^* p < 0.001$).

Table IV.4: Average Jacobian and anisotropic deformation index values for adipose, glandular, and total tissue.

Case	J			ADI		
	Adipose	Glandular	Total	Adipose	Glandular	Total
I	0.95	1.00	0.96	0.48	0.81	0.49
II.a	0.97	1.03	0.97	0.44	0.64	0.46
II.b	0.96	1.00	0.96	0.45	0.79	0.48
III.a	1.01	1.00	1.01	0.38	0.34	0.37
IV	0.95	1.00	0.96	0.60	0.73	0.61
V	0.93	0.99	0.96	0.64	0.58	0.61
III.b	0.93	1.00	0.96	0.53	0.57	0.55
VI.a	0.96	1.02	0.99	0.68	0.66	0.67
VI.b	0.94	1.05	0.98	0.57	0.58	0.57
VII.a	1.01	1.02	1.01	0.57	0.54	0.56
VII.b	0.93	1.03	0.97	0.57	0.40	0.51

IV.5.3 Finite Element Method Modeling Results

TRE performance for the three linear-elastic models with varying levels of complexity is shown in Table IV.5. For Model A (homogeneous isotropic model), the average TRE across all 11 cases was 5.4 $\pm$ 1.5 mm. In Model B (heterogeneous isotropic model), for 4 out of 11 cases, at least one R_1 parameter value improved TRE. In 7 out of 11 cases, adding heterogeneity in Model B for the instances where $R_1 \neq 1$ worsened TRE compared to Model A where $R_1 = 1$, and there was not a heterogeneous R_1 parameter value that improved TRE. For the 4 cases where TRE improved, the average improvement was very modest with the average optimal TRE across all 11 cases for Model B being 5.3 ± 1.5 mm. There was no significant difference in TRE values between Model A and Model B ($p > 0.01, p = 0.1250$).

For Model C (heterogeneous anisotropic model), there was at least one parameter sweep R_1 and R_2 combination that improved TRE compared to Model A for every case. The average of the minimum TRE values across all 11 cases was 4.7 ± 1.4 mm for Model C, which corresponds to a $11.7 \pm 8.7\%$ average improvement in TRE. There was a statistically significant difference in TRE values between Model A and Model C when tested using a paired Wilcoxon signed-rank test ($p < 0.01, p = 0.0010$). There was also a statistically significant difference in TRE values between Model B and Model C ($p < 0.01, p = 0.0010$).

These model performance results are displayed visually in Figure IV.6. To summarize, the x-axis of each subfigure designates varying glandular-to-adipose elastic stiffness contrast R_1, and each color-encoded line represents variations in longitudinal-to-transverse stiffness contrast ratios among the anisotropic properties R_2 (Model C). The black line in each subfigure represents the results of the heterogeneous isotropic model (Model B), with the dashed-black vertical line at $\log_2(R_1) = 0$ representing the line of homogeneity (Model A). As shown in Fig. 4, there is large variability in TRE behavior as a function of R_1 and R_2 for each individual case. However, the addition of model anisotropy on average improves TRE performance compared to the isotropic models. Due to the sparsity of the R_1 and R_2 parameter sweeps, we caution against interpreting the R_1 and R_2 values as individualized stiffness characterizations for each individual case.

IV.6 Discussion

This work demonstrates accurate deformable image registration between supine MR breast imaging taken in two distinct arm positions (arm-up and arm-down) meant to mimic surgical deformations. The results from these image registrations were then used to extract inferences about breast tissue material properties using J and ADI as mechanical indices. Both J and ADI value differences implied that nonrigid modeling methods may benefit from incorporating material properties reflecting heterogeneity and anisotropy. To explore this hypothesis, a quantitative evaluation of how incorporating heterogeneity and anisotropy affects modeling accuracy for a finite element method biomechanical modeling approach was performed in biomechanical modeling experiments.

One contribution of this work was utilizing the ANTs registration package for breast MR supine-to-supine image registration and analysis. While ANTs registration has been used extensively on neuroimaging data, its application for breast image registration is more limited. The specific method used here was the ANTs symmetric image normalization method with explicit B-spline regularization (a directly manipulated free-form deformation algorithm) with cross correlation as the similarity metric. Using Gaussian smoothing regularization instead of explicit B-spline regularization was explored, but the explicit B-spline regularization method performed significantly better ($p < 0.01$) in terms of TRE. This behavior likely arose because B-spline regularization can better capture the large deformations present in the breast. Using mutual information instead of

Table IV.5: Minimum TRE results from the homogeneous isotropic model (Model A), the optimal heterogeneous isotropic model (Model B), and the optimal heterogeneous transverse isotropic model (Model C). A dash (-) indicates no improvement (0.0%) over Model A and that $\log_2(R_i) = 0$ was optimal for Model B.

	Model A	Model B			Model C			
Case	TRE (mm)	TRE (mm)	% Improvement over Model A	Optimal $\log_2(R_1)$	TRE (mm)	% Improvement over Model A	Optimal $\log_2(R_1)$	Optimal $\log_2(R_2)$
I	5.9	5.9	-	0	5.2	11.3%	-4	7
II.a	6.4	6.4	-	0	5.8	9.0%	1	4
II.b	5.6	5.5	2.1%	-2	4.7	16.5%	-2	7
III.a	2.7	2.7	-	0	2.6	2.6%	-2	1
III.b	7.1	7.1	-	0	5.9	16.9%	0	7
IV	6.7	6.6	0.6%	2	5.3	21.3%	-1, 0	7
V	5.4	5.4	-	0	5.2	3.9%	-4	4
VI.a	7.1	7.0	2.0%	-4	6.9	2.7%	-4	1
VI.b	4.4	4.4	-	0	3.7	14.5%	-4	4
VII.a	4.0	4.0	-	0	3.9	1.8%	4	7
VII.b	3.8	3.7	3.2%	4	2.7	28.1%	2, 3	7
Mean ± std	*5.4 ± 1.5*	*5.3 ± 1.5*	*0.7 ± 1.2%*	*0.0 ± 2.0*	*4.7 ± 1.4*	*11.7 ± 8.7%*	*-1.2 ± 2.8*	*5.1 ± 2.4*

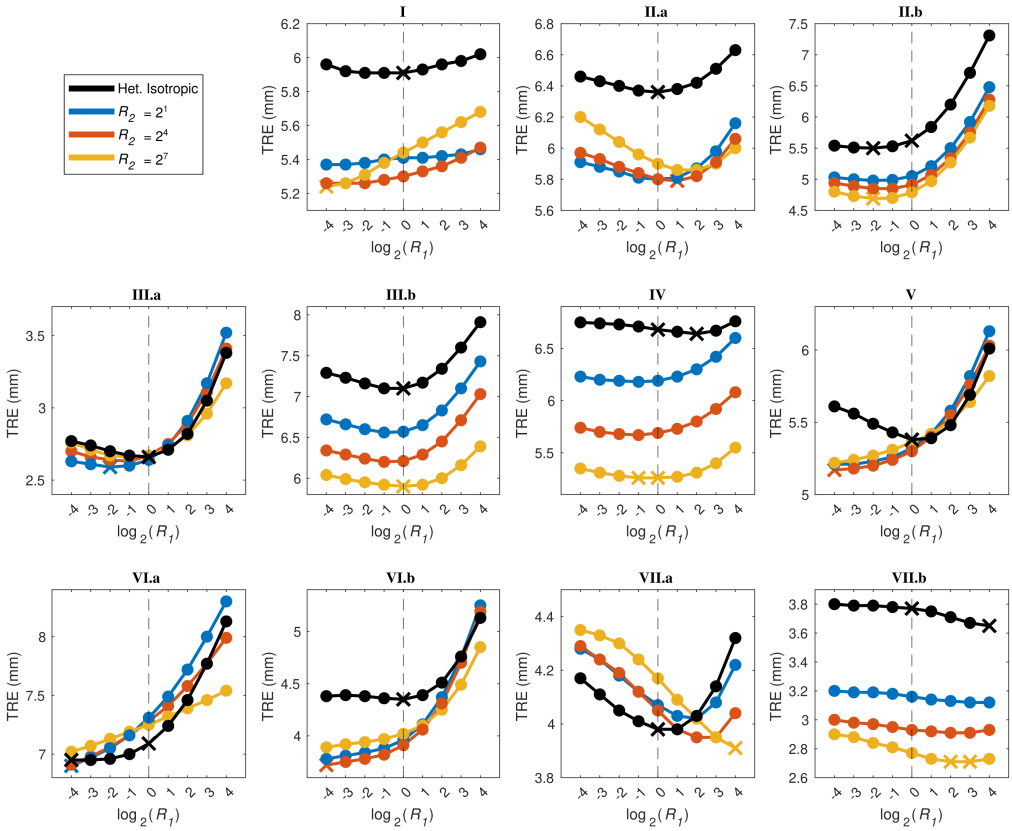

Figure IV.6: Parameter sweep results. TRE performance results from R_1 and R_2 parameter sweeps for each individual case labeled I - VII.b. The heterogeneous isotropic model, Model B, is shown as the black line. The heterogeneous transverse-isotropic models, Model C, are shown with the three R_2 parameter sweep values as the blue, red, and yellow lines. The vertical dashed line represents the line of homogeneity, with the circles intersecting the dashed line implemented as either homogeneous isotropic or homogeneous transverse-isotropic models. "X" indicates minimum TREs for Models A–C included in Table IV.5.

cross correlation as the similarity metric was also explored, and there was no significant difference ($p > 0.05$) in TRE results when using the different similarity metrics. However, cross correlation was selected as most applicable similarity metric for this dataset because it can be assumed that both the fixed and moving images have similar intensity profiles given that they are both MR images of the same subject. Other diffeomorphic image registration packages and algorithms have been applied to breast images previously including Elastix, Thirion's demons algorithm, and the DRAMMS algorithm [192; 207]. While more analysis is needed to evaluate ANTs registration performance compared to other available image registration packages, the ANTs registration parameters reported here may be applicable for additional breast image registration applications including longitudinal studies, inter-subject comparisons when studying tumor treatment responses, and performing multimodal registrations [208; 209].

With respect to understanding breast biomechanics and its material properties, the average J value across

all cases was 0.97 ± 0.02 suggesting, as expected, nearly no volume change ($J = 1$) in breast tissue between arm-down and arm-up positioning. However, examining the average J value within adipose and glandular tissue types separately showed statistically significant differences. While very modest, the J value for glandular tissue was slightly higher than the J value for adipose tissue. This suggests a variable response to different arm positions between adipose and glandular tissue, with glandular tissue expanding slightly more than adipose tissue. Additionally, the average ADI value across all cases was 0.53 ± 0.09 suggesting that the breast undergoes anisotropic deformation ($ADI > 0$) between arm-down and arm-up positions.

Insights into the heterogeneous and anisotropic nature of breast tissue led to a quantitative evaluation of how incorporating these factors affects modeling accuracy. In a set of biomechanical modeling experiments, three different models (Models A-C) with varying levels of complexity were implemented. There was very little improvement in TRE when using a heterogeneous isotropic model that accounted for glandular and adipose tissue (Model B) compared to using the homogeneous isotropic model (Model A). However, when using the heterogeneous transverse-isotropic model (Model C), there was statistically significant improvement in TRE performance compared to both the homogeneous isotropic and the heterogeneous isotropic models (Models A and B). This suggests that incorporating anisotropy through a transverse-isotropic material model can improve registration accuracy for breast modeling. This finding is consistent with anatomical depictions of the breast which report that the Cooper's ligaments and surrounding fascia form the breast's shape and structure. These tissues have directional variability, and Cooper's ligaments' tensile properties are estimated to be significantly stiffer than breast tissue [210]. Incorporating this ligament structure through a transverse-isotropic model may allow for tissue to deform in an anisotropic manner and more closely model the true breast tissue mechanics. Another interesting observation in Table IV.5 is that the glandular-to-adipose stiffness ratio (R_1) had little effect when considering tissue-type isotropy alone (Model B offered little improvement over Model A), but the ratio became more pronounced when anisotropy among the tissue-type components was introduced in Model C. This is shown by the difference in average reported R_1 values between Models B and C, which were 2^0 and $2^{-1.2}$, respectively. Additionally, the longitudinal-to-transverse stiffness ratio (R_2) on average was $2^{5.1}$ in Model C indicating a significantly stiffer longitudinal property. Another important observation is that in 9 of the 11 cases, homogeneous anisotropic tissue outperformed homogeneous isotropic tissue. Lastly, it should be noted that in 10 of 11 cases, the best performing parameter configuration was heterogeneous and anisotropic. Three general findings can be summarized from this biomechanical modeling study - (1) adding adipose and glandular tissue heterogeneity alone does not provide sufficient degrees of freedom to capture improvements in our modeling approach, (2) transverse isotropy provides additional degrees of freedom that resulted in localization improvement for all subjects, and (3) results indicate that the best solution would likely be one that incorporates heterogeneity and anisotropy.

IV.7 Limitations

Several limitations should be noted when interpreting the results of both the image registration and biomechanical modeling studies. The study cohort was limited to 7 volunteers with ages ranging from 23 to 57 years, and all volunteers were Caucasian. Studies about racial differences in breast material properties have had variable results, but factors including age, body mass index, and reproductive factors are all known to impact breast density and stiffness [211]. Also, cancerous tumors are typically stiffer than adipose and glandular tissue [141]. While this cohort is sufficient for preliminary exploration, investigation on a larger, more diverse population of breast cancer patients is of interest.

Another limitation is that all conclusions drawn from the biomechanical indices assume that the ANTs deformation field is correctly representing the true local deformation field that occurs between arm-down and arm-up positioning. For the biomechanical modeling study, the boundary conditions were derived from the deformation field calculated from the image-to-image registration method available in the ANTs repository. It is important to note that the ANTs deformation field is subject to method-specific bias from the image-to-image registration algorithm and not necessarily constrained by mechanics. The TRE results show that the ANTs registration achieves a registration accuracy lower than 3 mm for 75% of targets in all volunteers. However, the average maximum target registration error across all cases is 8.9 mm for ANTs registration, with the error from an individual target from one case being as high as 20.8 mm. This implies that there are some regions of the image volumes where ANTs registration is not accurate. This may be because of poor image quality in those regions, MR imaging artifacts, or a lack of distinguishable image features. These inaccuracies should be considered when using the biomechanical indices to make inferences about tissue properties.

Regarding the biomechanical modeling study, the R_1 and R_2 parameters were constrained by the sparsity of the parameter sweep. This parameter sweep was chosen to explore a range of potential stiffness values and demonstrate the effect of additional modeling parameters. However, because this sweep was limited, the stiffness ratios reported in Table IV.5 should not be interpreted as individualized stiffness characterizations for each case. More refinement with either a more localized parameter search or with the inclusion of direct elasticity measurement techniques would be needed for a more accurate measurement of breast tissue stiffness for each case. An optimization approach that solves for the R_1 and R_2 values that minimize target error could also be used to provide more nuanced insights into the breast tissue stiffness of each individual case. Another design choice was the longitudinal direction when incorporating anisotropy in the transverse-isotropic model. The longitudinal direction in the transverse-isotropic model was assumed to be perpendicular to the chest wall to simulate the direction of Cooper's ligaments, but the true orientation of Cooper's ligaments in

the breast is likely significantly more complex. It should be noted that in results not reported here, other approaches were pursued. For example, in one approach, principal directions were derived from the deformation gradient associated with the displacement field provided by the nonrigid image-to-image registration used to derive boundary conditions. While interesting, this approach did not outperform the one adopted. A high-resolution breast imaging technique that would specifically illuminate the underlying substructure of the breast associated with Cooper's ligaments may be useful for improved modeling approaches. While imaging methods designed to uncover anisotropy such as MR diffusion tensor imaging have been applied to breast parenchyma, it is not clear if these modalities can extract this substructure given the spatial size of these ligaments relative to the typical breast MR resolution and the sparsely distributed spatial configuration that is characteristic of these ligaments [212]. Additionally, given that ligament structures behave differently in tension versus compression, it is likely that local aspects of the stress configuration in the tissue would need to be considered. This awaits further study.

Another limitation in the biomechanical modeling study was the choice to use linear-elastic models. Using nonlinear hyper-elastic models may better capture soft-tissue dynamics, especially with larger deformations, and improve accuracy. However, a disadvantage of using nonlinear models is that they must be implemented as iterative methods that are not guaranteed to converge to a realistic solution especially when considering the methodology employed for boundary condition estimation. Additionally, nonlinear patient-specific material parameter characterizations are less accessible compared to linear models when considering clinically available elastography measurement techniques. More investigation is needed to evaluate the degree to which a more complex material model would improve modeling performance. Additionally, this study incorporated heterogeneity by including two breast tissue types – adipose and glandular tissue – as these two tissue types constitute most of the breast parenchyma. However, other biomechanical modeling efforts have included separate material models for skin, muscle, and fascia. These too await further exploration.

IV.8 Conclusion

In this work, an image registration method from the ANTs repository was used to register supine breast MR images. Subsurface TRE was 2.8 ± 1.3 mm between registered supine MR images acquired in two distinct arm positions (arm-down and arm-up). Biomechanical indices calculated from the ANTs deformation field suggest that adipose and glandular tissue vary in terms of volume change and that the breast undergoes anisotropic deformation during the arm-down to arm-up motion. This investigation suggests that model-based registration may improve with approaches that incorporate anisotropic material properties and heterogeneous tissue types. Linear elastic FEM models with varying levels of complexity were implemented to test this hypothesis. Overall, quantitative accuracy measurements of biomechanical modeling approaches meant to

simulate breast deformations in the supine position showed that a heterogeneous anisotropic model was significantly more accurate than either a homogeneous isotropic model or a heterogeneous isotropic model. Incorporating anisotropy by using a transverse-isotropic model offered an 11.7% improvement in target error on average while still being relatively simple in terms of implementation. This analysis may be useful for future work toward developing biomechanical models that can accurately predict supine breast deformations, with the potential for more accurate patient-specific material properties as elastography imaging methods continue to improve. It also demonstrates the utility of image-to-image registration in uncovering soft-tissue mechanical properties, which is an underemphasized application of image-to-image registration compared to its use for longitudinal and inter-subject comparisons.

Acknowledgements

This work was supported by the National Institutes of Health through Grant Nos. R01EB027498 and T32EB021937, the National Science Foundation for a Graduate Research Fellowship awarded to M.J.R., and the Vanderbilt Center for Human Imaging supported by Grant No. 1S10OD021771-01 for the 3T MRI.

CHAPTER V

Regularized Kelvinlet functions for breast deformation modeling

This next chapter details Aim 2 of this dissertation, which is to establish a breast deformation model that can be used in the intraoperative environment. Regularized Kelvinlet functions are proposed as a novel method for mechanics based breast deformation modeling. These functions are combined with a method for nonrigid image-to-physical registration. Registration accuracy is evaluated using the same dataset of healthy volunteer supine MR images from Aim 1 in Chapter IV. Tumor overlap metrics are evaluated using an example case from one breast cancer patient.

V.1 Abstract

Image-guided surgery requires fast and accurate registration to align preoperative imaging and surgical spaces. The breast undergoes large nonrigid deformations during surgery, compromising the use of imaging data for intraoperative tumor localization. Rigid registration fails to account for nonrigid soft tissue deformations, and biomechanical modeling approaches like finite element simulations can be cumbersome in implementation and computation. In this work, regularized Kelvinlet functions are introduced for breast registration. These functions are closed-form smoothed solutions to the partial differential equations for linear elasticity. Analytical equations that represent nonrigid point-based translation ("grab") and rotation ("twist") deformations embedded within an infinite elastic domain are derived and presented. Computing a displacement field using this method does not require mesh discretization or large matrix assembly and inversion conventionally associated with finite element or mesh-free methods. For registration, the optimal superposition of regularized Kelvinlet functions that achieves alignment of the medical image to simulated intraoperative geometric point data of the breast is computed. Registration performance is evaluated using a dataset of supine MR breast imaging from healthy volunteers mimicking surgical deformations with 237 individual targets from 11 breasts. An analysis of the method's sensitivity to the regularized Kelvinlet function hyperparameters is included. To demonstrate application, registration is performed on a breast cancer patient case with a segmented tumor, and performance is compared to other image-to-physical and image-to-image registration methods. This method was shown to have comparable accuracy to a previously proposed image-to-physical registration method with improved computation time, making regularized Kelvinlet functions an attractive approach for image-to-physical registration problems.

V.2 Contributions

This chapter is adapted from a conference proceedings paper, "Regularized Kelvinlet Functions to Model Linear Elasticity for Image-to-Physical Registration of the Breast" presented at the Medical Image Computing and Computer Assisted Intervention (MICCAI) 2023 conference. The summary and discussion sections are supplemented with text from a journal article, "Comparing Regularized Kelvinlet Functions and the Finite Element Method for Registration of Medical Images to Sparse Organ Data" released on arXiv and currently in review at Medical Image Analysis. This work has been reproduced with permission from the publisher.

[213]: M. J. Ringel, J. S. Heiselman, W. L. Richey, I. M. Meszoely, and M. I. Miga, "Regularized Kelvinlet Functions to Model Linear Elasticity for Image-to-Physical Registration of the Breast," *Medical Image Computing and Computer Assisted Intervention – MICCAI 2023,* pp. 344–353, 2023.

[214]: M. J. Ringel, J. S. Heiselman, W. L. Richey, I. M. Meszoely, W. R. Jarnagin, and M. I. Miga, "Comparing Regularized Kelvinlet Functions and the Finite Element Method for Registration of Medical Images to Sparse Organ Data," *arXiv, Medical Image Analysis (In Review),* 2023.

V.3 Introduction

Image-to-physical registration is a necessary process for computer assisted surgery to align preoperative imaging to the intraoperative physical space of the patient to inform surgical decision making. Most intraoperatively utilized image-to-physical registrations are rigid transformations calculated using fiducial landmarks [14]. However, with better computational resources and more advanced surgical field monitoring sensors, nonrigid registration techniques have been proposed [215; 216]. This has made image-guided surgery more tractable for soft tissue organ systems like the liver, prostate, and breast [217; 138; 218]. This work focuses specifically on nonrigid breast registration, although these methods could be adapted for other soft tissue organs. Current guidance technologies for breast conserving surgery localize a single tumor-implanted seed without providing spatial information about the tumor boundary. As a result, resections can have several centimeters of tissue beyond the cancer margin. Despite seed information and large resections, reoperation rates are still high ($\sim$17%), emphasizing the need for additional guidance technologies such as computer assisted surgery systems with nonrigid registration [11].

Intraoperative data available for registration is often sparse and subject to data collection noise. Image-to-physical registration methods that accurately model an elastic soft tissue environment while also complying with intraoperative data constraints is an active field of research. Determining correspondences between imaging space and geometric data is required for image-to-physical registration, but it is often an inexact and ill-posed problem. Establishing point cloud correspondences using machine learning has been demonstrated

on liver and prostate datasets [219; 220]. Deep learning image registration methods like VoxelMorph have also been used for this purpose [221]. However, these methods require extensive training data and may struggle with generalizability. Other non-learning image-to-physical registration strategies include [222] which utilized a corotational linear-elastic finite element method (FEM) combined with an iterative closest point algorithm. Similarly, the registration method introduced in [20] iteratively updated the image-to-physical correspondence between surface point clouds while solving for an optimal deformation state.

In addition to a correspondence algorithm, a technique for modeling a deformation field is required. Both [222] and [20] leverage FEM, which uses a 3D mesh to solve for unique deformation solutions. However, large deformations can cause mesh distortions with the need for remeshing. Mesh free methods have been introduced to circumvent this limitation. The element free Galerkin method is a mesh free method that requires only nodal point data and uses a moving least-squares approximation to solve for a solution [223]. Other mesh free methods are reviewed in [181]. Although these methods do not require a 3D mesh, solving for a solution can be costly and boundary condition designation is often unintuitive. Having identified these same shortcomings, [19] proposed regularized Kelvinlet functions for volumetric digital sculpting in computer animation applications. This sculpting approach provided deformations consistent with linear elasticity without large computational overhead.

In this work, we propose an image-to-physical registration method that uses regularized Kelvinlet functions as a novel deformation basis for nonrigid registration. Regularized Kelvinlet functions are analytical solutions to the equations for linear elasticity that can be superposed to compute a nonrigid deformation field nearly instantaneously [19]. "Grab" and "twist" regularized Kelvinlet functions are utilized with a linearized iterative reconstruction approach (adapted from [20]) that is well-suited for sparse data registration problems. Sensitivity to regularized Kelvinlet function hyperparameters is explored on a supine MR breast imaging dataset. Finally, our approach is validated on an example breast cancer case with a segmented tumor by comparing performance to previously proposed registration methods.

V.4 Methods

In this section, closed-form solutions to linear elastic deformation responses in an infinite medium are derived to obtain regularized Kelvinlet functions. Then, methods for constructing a superposed regularized Kelvinlet function deformation basis for achieving registration within an iterative reconstructive framework are discussed. Equation notation is written such that constants are italicized, vectors are bolded, and matrices are double-struck letters.

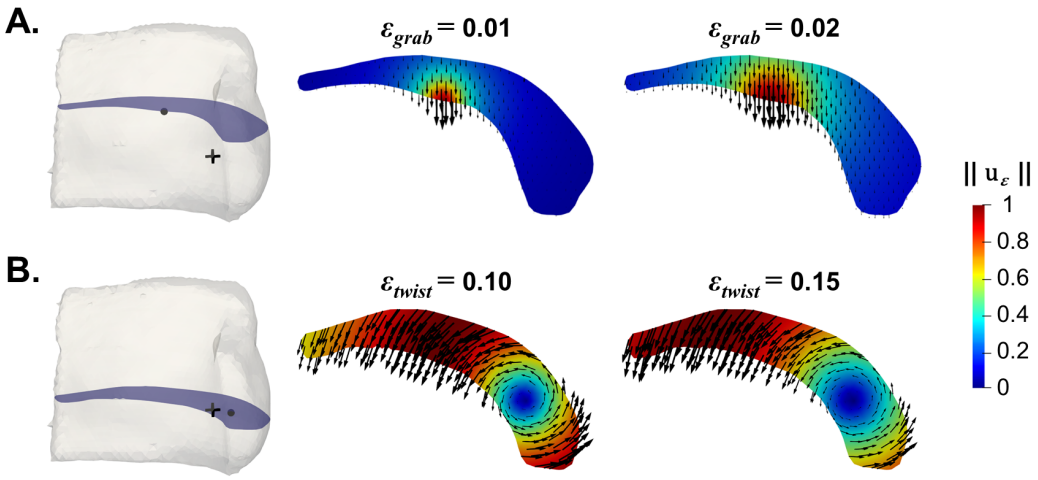

Figure V.1: Visualization of (A) "grab" and (B) "twist" regularized Kelvinlet functions on 2D breast geometry axial slices at various ε values. (+) denotes nipple location, (•) denotes x_0 location.

V.4.1 Regularized Kelvinlet Functions

Linear elasticity in a homogeneous, isotropic media is governed by the Navier Cauchy equations in Equation V.1, where E is Young's modulus, ν is Poisson's ratio, $\mathbf{u}(\boldsymbol{x})$ is the displacement vector, and $\mathbf{F}(\boldsymbol{x})$ is the forcing function. Analytical displacement solutions to Equation V.1 that represent elastostatic states in an infinite solid can be found for specific forcing functions $\mathbf{F}(\boldsymbol{x})$. Equation V.2 represents the forcing function for a point source $\mathbf{F}_\delta(\boldsymbol{x})$, where $\boldsymbol{f}$ is the point source forcing vector and $\boldsymbol{x}_0$ is the load location. The closed-form displacement solution for Equation V.1 given the forcing function in Equation V.2 is classically known as the Kelvin state in Equation V.3, rewritten as a function of $\boldsymbol{r}$ where $\boldsymbol{r} = \boldsymbol{x} - \boldsymbol{x}_0$ and $r = \|\boldsymbol{r}\|$. The coefficients are $a = \frac{(1+\nu)}{2\pi E}$, $b = \frac{a}{4(1-\nu)}$, and $\mathbb{I}$ is the identity matrix.

We note that the deformation response is linear with respect to $\boldsymbol{f}$, which implies that forcing functions can be linearly superposed. However, practical use of Equation V.3 becomes numerically problematic in discretized problems because the displacement and displacement gradient become indefinite as $\boldsymbol{x}$ approaches $\boldsymbol{x}_0$.

$$\frac{E}{2(1+\nu)}\nabla^2\mathbf{u}(\boldsymbol{x}) + \frac{E}{2(1+\nu)(1-2\nu)}\nabla(\nabla\cdot\mathbf{u}(\boldsymbol{x})) + \mathbf{F}(\boldsymbol{x}) = 0 \tag{V.1}$$

$$\mathbf{F}_\delta(\boldsymbol{x}) = \boldsymbol{f}\delta(\boldsymbol{x}-\boldsymbol{x}_0) \tag{V.2}$$

$$\mathbf{u}(\boldsymbol{r}) = \left[\frac{a-b}{r}\mathbb{I} + \frac{b}{r^3}\boldsymbol{r}\boldsymbol{r}^t\right]\boldsymbol{f} = \mathbb{K}(\boldsymbol{r})\boldsymbol{f} \tag{V.3}$$

To address numerical singularity, regularization is incorporated with a new forcing function in Equation V.4, where $r_\varepsilon = \sqrt{r^2+\varepsilon^2}$ is the regularized distance, and ε is the regularization radial scale. Solving Equation V.1 using Equation V.4 yields a formula for the first type of regularized Kelvinlet functions used in this work in Equation V.5, which is the closed-form, analytical solution for linear elastic translational ("grab") deformations.

$$\mathbf{F}_\varepsilon(\boldsymbol{x}) = \boldsymbol{f}\left[\frac{15\varepsilon^4}{8\pi}\frac{1}{r_\varepsilon^7}\right] \tag{V.4}$$

$$\mathbf{u}_{\varepsilon,grab}(\boldsymbol{r}) = \left[\frac{a-b}{r_\varepsilon}\mathbb{I} + \frac{b}{r_\varepsilon^3}\boldsymbol{r}\boldsymbol{r}^t + \frac{a}{2}\frac{\varepsilon^2}{r_\varepsilon^3}\mathbb{I}\right]\boldsymbol{f} = \mathbb{K}_{grab}(\boldsymbol{r})\boldsymbol{f} \tag{V.5}$$

The second type of regularized Kelvinlet functions represent "twist" deformations which are derived by expanding the previous formulation to accommodate locally affine loads instead of displacement point sources. This is accomplished by associating each component of the forcing function in Equation V.4 with the directional derivative of each basis $\boldsymbol{g}_i$ of the affine transformation, leading to the regularized forcing matrix in Equation V.6. An affine loading configuration consisting of pure rotational ("twist") deformation constrains $\mathbb{F}_\varepsilon^{ij}(\boldsymbol{x})$ to a skew-symmetric matrix that simplifies the forcing function to a cross product about a twisting force vector $\boldsymbol{f}$ in Equation V.7. The pure twist displacement field response $\mathbf{u}_{\varepsilon,twist}(\boldsymbol{r})$ to the forcing matrix in Equation V.7 can be represented as the second type of regularized Kelvinlet functions used in this work in Equation V.8.

Superpositions of Equation V.5 and Equation V.8 are used in a registration workflow to model linear elastic deformations in the breast. These deformations are visualized on breast geometry embedded in an infinite medium with varying ε values in Figure V.1.

$$\mathbb{F}_\varepsilon^{ij}(\boldsymbol{x}) = \boldsymbol{g}_i \cdot \nabla \boldsymbol{f}_j\left[\frac{15\varepsilon^4}{8\pi}\frac{1}{r_\varepsilon^7}\right] \tag{V.6}$$

$$\left[\mathbb{F}_\varepsilon^{ij}\right]_\times(\boldsymbol{x}) = -\boldsymbol{r}\times\boldsymbol{f}\left[\frac{15\varepsilon^4}{8\pi}\frac{1}{r_\varepsilon^7}\right] \tag{V.7}$$

$$\mathbf{u}_{\varepsilon,twist}(\boldsymbol{r}) = a\left(\frac{1}{r_\varepsilon^3} + \frac{3\varepsilon^2}{2r_\varepsilon^5}\right)\boldsymbol{r}\times\boldsymbol{f} = \left[\mathbb{K}_{twist}(\boldsymbol{r})\right]_\times\boldsymbol{f} \tag{V.8}$$

V.4.2 Registration Task

For registration, $\boldsymbol{x}_0$ control point positions for k number of total regularized Kelvinlets "grab" and "twist" functions are distributed in a predetermined configuration. Then, the $\boldsymbol{f}_{grab}$ and $\boldsymbol{f}_{twist}$ vectors are optimized to

solve for a displacement field that minimizes distance error between geometric data inputs.

For a predetermined configuration of regularized Kelvinlet "grab" and "twist" functions centered at different $\boldsymbol{x}_0$ control point locations, an elastically deformed state can be represented as the summation of all regularized Kelvinlet displacement fields where $\tilde{\mathbf{u}}(\boldsymbol{x})$ is the superposed displacement vector and $k = k_{grab} + k_{twist}$ in Equation V.9. Equation V.9 can be rewritten in matrix form shown in Equation V.10, where $\boldsymbol{\alpha}$ is a concatenated vector of length $3k$ such that $\boldsymbol{\alpha} = \left[\boldsymbol{f}^1_{grab}, \boldsymbol{f}^2_{grab}, \ldots, \boldsymbol{f}^k_{twist}\right]$.

$$\tilde{\mathbf{u}}(\boldsymbol{x}) = \sum_{i=1}^{k_{grab}} \mathbf{u}^i_{\varepsilon,grab}(\boldsymbol{x}) + \sum_{i=1}^{k_{twist}} \mathbf{u}^i_{\varepsilon,twist}(\boldsymbol{x}) \tag{V.9}$$

$$\tilde{\mathbf{u}} = \mathbb{K}(\boldsymbol{x})\boldsymbol{\alpha} \tag{V.10}$$

This formulation decouples the forcing magnitudes from the Kelvinlet response matrix $\mathbb{K}(\boldsymbol{x})$, which is composed of column $\mathbf{u}_{\varepsilon,grab}(\boldsymbol{x})$ and $\mathbf{u}_{\varepsilon,twist}(\boldsymbol{x})$ vectors calculated with unit forcing vectors for each $\mathbb{K}_{grab}(\boldsymbol{x})$ and $\mathbb{K}_{twist}(\boldsymbol{x})$ function. This allows for linear scaling of $\mathbb{K}(\boldsymbol{x})$ using $\boldsymbol{\alpha}$. By setting $\boldsymbol{x}_0$ locations, ε_{grab}, and ε_{twist} as hyperparameters, deformation states can be represented by various $\boldsymbol{\alpha}$ vectors with the registration task being to solve for the optimal $\boldsymbol{\alpha}$ vector.

An objective function is formulated to minimize misalignment between the moving space $\boldsymbol{x}_{\boldsymbol{moving}}$ and fixed space $\boldsymbol{x}_{\boldsymbol{fixed}}$ through geometric data constraints. For the breast imaging datasets in this work, simulated intraoperative data features that realistically could be collected in a surgical environment are used, and these features are shown in Figure V.2. The first data feature is MR-visible skin fiducial points placed on the breast surface (Figure V.2, red). These fiducials have known point correspondence. The other two data features are an intra-fiducial point cloud of the skin surface (Figure V.2, light blue) and sparse contour samples of the chest wall surface (Figure V.2, yellow). These data features are surfaces that do not have known correspondence. These data feature designations are consistent with implementations in previous work [139; 224].

For a given deformation state, each data feature contributes to the total error measure. For the point data, the error e^i_{point} for each point i is simply the distance magnitude between corresponding points in $\boldsymbol{x}_{\boldsymbol{fixed}}$ and $\boldsymbol{x}_{\boldsymbol{moving}}$ space. For the surface data, the error $e^i_{surface}$ is calculated as the distance from every point i in the $\boldsymbol{x}_{\boldsymbol{fixed}}$ point cloud surface to the closest point in the $\boldsymbol{x}_{\boldsymbol{moving}}$ surface, projected onto the surface unit normal which allows for sliding contact between surfaces.

The optimization using the objective function in Equation V.11 includes two additions to improve the solution. The first is rigid parameters, translation $\boldsymbol{\tau}$ and rotation $\boldsymbol{\theta}$, that are optimized simultaneously with the vector $\boldsymbol{\alpha}$. $\boldsymbol{\beta}$ represents the deformation state with $\boldsymbol{\beta} = [\boldsymbol{\alpha}, \boldsymbol{\tau}, \boldsymbol{\theta}]$, and this compensates for rigid deformation between $\boldsymbol{x}_{\boldsymbol{fixed}}$ and $\boldsymbol{x}_{\boldsymbol{moving}}$. The second is a strain energy regularization term e_{SE} which penalizes deformations

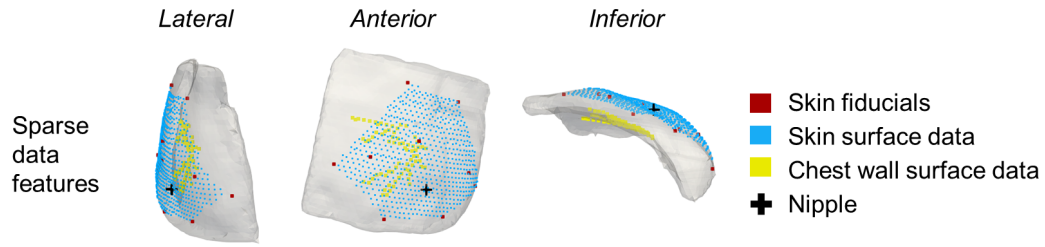

Figure V.2: Sparse data features on breast geometry in the $\boldsymbol{x_{fixed}}$ space.

with large strain energy. e_{SE} is the average strain energy density within the breast geometry, and it is computed for each $\boldsymbol{\beta}$ at every iteration. It is scaled by weight w_{SE}. The optimal state $\boldsymbol{\beta}$ is iteratively solved using Levenberg-Marquardt optimization terminating at $|\Delta\Omega(\boldsymbol{\beta})| < 10^{-12}$.

$$\Omega(\boldsymbol{\beta}) = \frac{1}{n_{point}} \sum_{i=1}^{n_{point}} (e^i_{point})^2 + \frac{1}{n_{surface}} \sum_{i=1}^{n_{surface}} (e^i_{surface})^2 + w_{SE}(e_{SE})^2 \tag{V.11}$$

V.5 Experiments and Results

In this section, two experiments are conducted. The first explores sensitivity to regularized Kelvinlet function hyperparameters $k_{grab}, k_{twist}, \varepsilon_{grab}$, and ε_{twist} and establishes optimal hyperparameters in a training dataset of 11 breast deformations. The second validates the registration method in a breast cancer patient and compares registration accuracy and computation time to previously proposed methods.

V.5.1 Hyperparameters Sensitivity Analysis

This dataset consists of supine breast MR images simulating surgical deformations of 11 breasts from 7 healthy volunteers. Volunteers (ages 23-57) were enrolled in a study approved by the Institutional Review Board at Vanderbilt University. Prior to imaging, 23-26 skin fiducials were distributed on the breast surface. MR images (0.391 x 0.391 x 1 mm^3 or 0.357 x 0.357 x 1 mm^3) were acquired with the volunteers' arms placed by their sides. This image was used as the $\boldsymbol{x_{moving}}$ space. The volunteers were then instructed to raise one arm above their heads, causing deformation of the ipsilateral breast. A second MR image in the deformed state was acquired to create simulated intraoperative physical data and to use for validation. This second image was used as the $\boldsymbol{x_{fixed}}$ space.

The breast in $\boldsymbol{x_{moving}}$ was segmented at the boundary between the chest wall and breast parenchyma to create a 3D model. The posterior surface was labeled to inform $\boldsymbol{x}_0$ control point locations. The skin fiducials and intra-fiducial surface point clouds were labeled in both images as data features. Sparse tracked ultrasound data collection patterns were projected on the posterior surface for use as the third data feature. Subsurface anatomical targets were labeled in both images and used to compute target error after registration.

Three configurations were explored to test different distributions of grab and twist regularized Kelvinlet functions - grab functions only, twist functions only, and a combination of grab and twist functions. Grab function control points were distributed evenly on the posterior surface of the breast to approximate forces from the chest wall. Twist function control points were distributed evenly within the breast to approximate internal body forces. Three hyperparameter sweeps were used:

- **Configuration 1:** $k_{grab} = \{10, 40, 70, 100\}, \varepsilon_{grab} = \{0.005, 0.05, 0.5\}$
- **Configuration 2:** $k_{twist} = \{10, 40, 70, 100\}, \varepsilon_{twist} = \{0.05, 0.1, 0.2\}$
- **Configuration 3:** $k_{grab} = 40, \varepsilon_{grab} = 0.05, k_{twist} = \{1, 5, 10, 20\}, \varepsilon_{twist} = \{0.05, 0.1, 0.2\}$

For all registrations, mechanical breast properties were set at $\nu = 0.45, E = 2100$ Pa, and $w_{SE} = 10^{-9}$ Pa^{-2} [139; 225]. Accuracy was evaluated by measuring target error (distance magnitude between targets in $\boldsymbol{x_{fixed}}$ and registered $\boldsymbol{x_{moving}}$ spaces) for all targets in 11 breast imaging sets totaling 237 targets per registration.

Target error results from hyperparameter sweep registrations are shown in Figure V.3. The registration with the lowest root mean squared error was from Configuration 3 - $k_{grab} = 40, \varepsilon_{grab} = 0.05, k_{twist} = 1, \varepsilon_{twist} = 0.1$. These hyperparameters were used on a different dataset for validating and comparing the registration method in Section V.5.2.

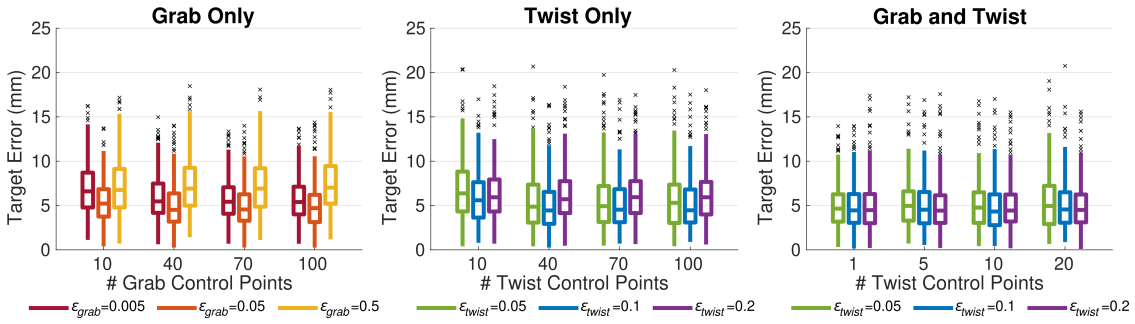

Figure V.3: Target error results from regularized Kelvinlet functions hyperparameter sweeps. Outliers are noted as (x) and are 1.5· IQR.

V.5.2 Registration Methods Comparison

This dataset consists of supine breast MR images simulating surgical deformations from one breast cancer patient. A 71-year-old patient with invasive mammary carcinoma in the left breast was enrolled in a study approved by the Institutional Review Board at Vanderbilt University. Skin fiducial placement, image acquisition, arm placement, and preprocessing steps followed the same protocol detailed in Section V.5.1. The tumor was segmented in both images by a subject matter expert, and a 3D tumor model was created to evaluate tumor overlap metrics after registration.

Regularized Kelvinlet function registration was compared to three other registration methods - rigid registration, an FEM-based image-to-physical registration method, and an image-to-image registration method. A point-based rigid registration using the skin fiducials provided a baseline comparator for accuracy without deformable correction. The FEM-based image-to-physical registration method, detailed in [20] and implemented in breast in [139], utilizes the same optimization scheme as this method but with an FEM-generated basis. $k = 40$ control points were used for the FEM-based registration. The image-to-image registration method was a symmetric diffeomorphic method with explicit B-spline regularization publicly available in the Advanced Normalization Toolkit (ANTs) repository [201; 190]. Image-to-image registration would not be possible for intraoperative registration in most surgical settings. However, it was included to demonstrate accuracy when volumetric imaging data is available, as opposed to sparse geometric point data as in the surgical application case. The rigid and image-to-physical registrations were performed on a single thread of a 3.6 GHz AMD Ryzen 7 3700X CPU. Image-to-image registration was multithreaded on 2.3 GHz Intel Xeon (E5-4610 v2) CPUs.

Registration results for the 4 methods are shown in Table V.1. The regularized Kelvinlet method accuracy was comparable (if not slightly improved) to the FEM-based method for this example case. Runtime for the regularized Kelvinlet method was improved compared to the FEM-based method. As expected, registration without deformable correction was poor, and image-to-image registration had the best accuracy. Registered tumor geometry results are shown in Figure V.4.

Table V.1: Registration performance for 4 methods. HD - Hausdorff distance.

		Rigid	**Image-to-Physical**		**Image-to-Image**
			FEM	**R. Kelvinlets**	
Point	Fiducial Error (mm)	7.4 ± 2.0	0.7 ± 0.5	1.4 ± 0.6	2.0 ± 1.7
Metrics	Target Error (mm)	6.1 ± 1.4	3.3 ± 1.1	3.0 ± 1.1	2.3 ± 1.5
Tumor	Dice Coefficient	2.3%	32.7%	49.5%	85.8%
Overlap	Centroid Distance (mm)	7.3	4.4	3.5	1.3
Metrics	Modified HD (mm)	4.1	2.2	1.7	0.6
Runtime (seconds)		<1	188	14	15,942

V.6 Discussion

The results show that regularized Kelvinlets can be used for reconstructing deformation states on an in vivo breast imaging dataset. Previous applications of regularized Kelvinlets have been confined to creating realistic in silico deformations for 2D or 3D animation. This work evaluates regularized Kelvinlets for modeling elastic deformations in the physical world. Regularized Kelvinlet deformations are computed in an infinite elastic domain that is not representative of deformations for physical elastic objects with finite material bounds. Although this is a constraint, the results here demonstrate that regularized Kelvinlets can offer computational

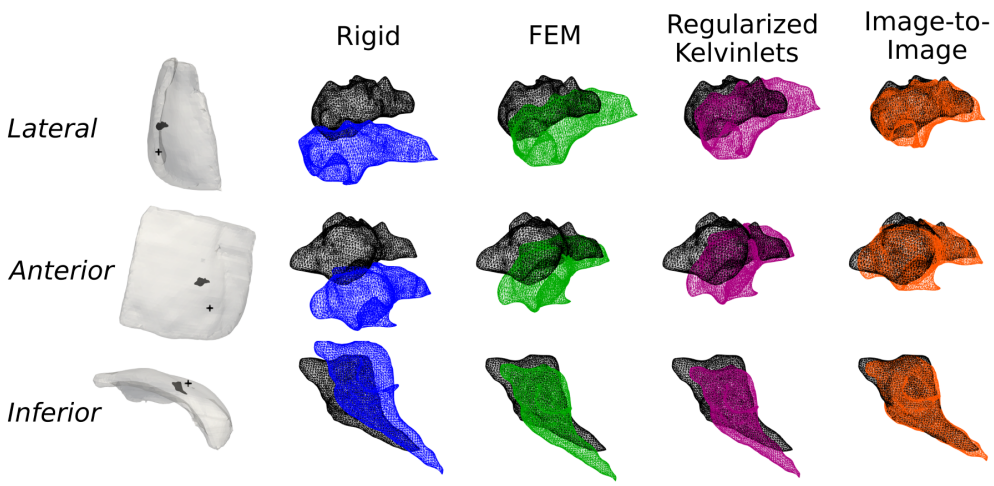

Figure V.4: Tumor overlap after registration. Black – $\boldsymbol{x}_{fixed}$ tumor used for validation. Blue – rigidly registered $\boldsymbol{x}_{moving}$ tumor. Green – FEM-based registered $\boldsymbol{x}_{moving}$ tumor. Pink – regularized Kelvinlet function registered $\boldsymbol{x}_{moving}$ tumor. Orange – image-to-image registered $\boldsymbol{x}_{moving}$ tumor.

advantages without significant degradation in accuracy specifically for sparse data organ registration problems.

One implementation consideration is the selection of the regularization radial scale ε and number of control points k parameters for a registration application where validation data is not available. Registration accuracy demonstrated little degradation (< 1 mm) within a range of ε and k values as shown in Figure V.3, showing that accuracy performance is robust for varying parameter values. Because the k parameter is directly related to precomputation and reconstruction computation time, $k = 40$ is likely an adequate choice for similar registration problems to balance between accuracy and computation time. However, the k_{grab} and k_{twist} parameters should be re-evaluated depending on the availability of sparse data inputs. With more sparse data availability, the registration problem would be more constrained. Increasing k in this scenario would allow more flexibility in resolving a larger set of possible registrations without causing an ill-conditioned inverse problem with too many degrees of freedom. Selecting an optimal k should be determined by the amount of sparse data available, and it is expected that performance suffers at very small and very large k values relative to the amount of available sparse data. For the regularization radial scale parameter ε, $\varepsilon_{grab} = 0.05$ and $\varepsilon_{twist} = 0.1$ were selected as the optimal parameters. Similar to the k parameter, ε values similar to the ones used in this work are likely sufficient for other registration applications, assuming a similar geometric scale to breast. However, the ε parameter controls the smoothness of the superposed regularized point loads and the degree of subsurface field penetration. These factors should be considered on a case-by-case basis when applying this method to new applications.

V.7 Limitations

Several limitations should be noted. Regularized Kelvinlet functions describe solutions that assume a physical embedding within an infinite elastic domain, which does not account for organ-specific geometry. This approach may not be well suited for problems where geometry has significant influence. This method is derived from a linear elastic model, and nonlinear models are known to better describe soft tissue mechanics. Additionally, this method assumes homogeneity and isotropy – it does not account for different tissue types and directional structures in the breast. With regards to clinical feasibility, supine MR imaging with skin fiducials is not the standard-of-care. However, using supine MR imaging for surgery is becoming increasingly investigated, and previous work demonstrated the potential of ink-based skin fiducial markings on the breast [5; 226]. Despite these limitations, this method's accuracy and speed may be appropriate for surgical guidance applications.

V.8 Conclusion

In this work, we demonstrated the use of regularized Kelvinlet functions for image-to-physical registration of the breast. We achieved near real-time registration with comparable accuracy to previously proposed methods. We believe that this approach is generalizable to other soft-tissue organ systems and is well-suited for improving navigation during image-guided surgeries.

Acknowledgements

This work was supported by the National Institutes of Health through Grant Nos. R01EB027498 and T32EB021937, the National Science Foundation for a Graduate Research Fellowship awarded to M.R., and the Vanderbilt Center for Human Imaging supported by Grant No. 1S10OD021771-01 for the 3T MRI.

CHAPTER VI

Image guidance system with integrated breast deformation correction

This chapter details the final Aim 3 of this dissertation, which is to present a fully integrated BCS-IGS system for prospective nonrigid registration. First, the system hardware and software components are discussed. The system includes a portable cart with optical tracking and stereo camera sensors for surgical scene monitoring. The mechanics based breast deformation model presented in Aim 2 is integrated into the system for near real-time nonrigid registration. Finally, the BCS-IGS system is demonstrated during breast phantom experiments and on one healthy volunteer.

VI.1 Abstract

Breast conserving surgery (BCS) is a common treatment option for women with early stage breast cancer, but these procedures have high and variable reoperation rates due to positive margins. Current tumor localization technologies do not provide real-time spatial information about the tumor boundary, emphasizing the need for additional navigation tools. This work proposes an image-guidance system for BCS that combines stereo camera soft tissue monitoring with nonrigid registration to account for misalignments from soft-tissue deformations. The guidance system integrates an optical tracking sensor and a 3D stereo camera sensor for surgical field monitoring. A custom user interface and display, developed using 3D Slicer, facilitates data collection and visualization of patient-specific imaging data and models. Near real-time deformable correction is driven by tissue displacement measurements and compensates for breast shape change. The feasibility and effectiveness of the guidance system are demonstrated through breast phantom deformation experiments that simulated tissue deformations. In 4 deformation states, 3D stereo camera sensor data is collected, and imaging data is deformed in near real-time. Evaluation results show a reduction in fiducial and surface registration errors after deformable correction compared to conventional rigid registration approaches. The guidance system is then demonstrated on a healthy volunteer, where data collection and nonrigid correction are performed in a mock intraoperative setting. Overall, the proposed system achieved data collection and navigation capabilities compatible with current BCS workflows. However, quantitatively measuring navigation accuracy and clinical value is not addressed here and should be the focus of future work.

VI.2 Contributions

This chapter is adapted from a conference proceedings paper, “Image Guidance System for Breast Conserving Surgery with Integrated Stereo Camera Monitoring and Deformable Correction” presented at the SPIE

Medical Imaging 2024 conference. This work is accepted and pending publication.

[227]: M. J. Ringel, W. L. Richey, J. S. Heiselman, A. Stabile, I. M. Meszoely, M. I. Miga, "Image Guidance System for Breast Conserving Surgery with Integrated Stereo Camera Monitoring and Deformable Correction" in *Proceedings of SPIE Medical Imaging,* Accepted (pending publication), 2024.

VI.3 Introduction

Breast conserving surgery (BCS) is a commonly used treatment option for early-stage breast cancer that aims to completely resect the tumor with negative margins while preserving healthy breast tissue and maintaining cosmesis. Positive margin rates for BCS range widely among surgeons and centers, impacting patient outcomes and necessitating additional treatments like reoperation procedures. Similarly, reoperation rates also vary by provider and hospital, but recent studies suggest aggregate reoperation rates range between 17-22% in the United States due to positive or close margins [11; 12]. This means that approximately 1 in every 5 women undergoing BCS will have to return to the operating room for a second surgery, causing patient stress, delays in postoperative adjuvant therapies, worse cosmetic outcomes, and additional healthcare costs.

Current tumor localization technologies including wire-guided localization and seed-based methods lack the ability to provide updated spatial information about the tumor boundary during surgery. In recent years, efforts to overcome this limitation by integrating image guidance into soft-tissue surgeries such as BCS have been underway. Registering preoperative imaging to the surgical scene can offer navigational assistance when planning tumor resections and localizing key nearby anatomical structures. However, translating registration approaches to BCS is challenging due to intraprocedural soft-tissue deformations occurring between surgical and imaging positions. The typical diagnostic imaging modality is mammography where the breast is compressed between two plates. In some circumstances, magnetic resonance (MR) imaging is performed where the patient lies prone with the breast pendant. In both of these positions, the breast positioning is considerably different from the surgical positioning where the patient lies supine with the ipsilateral arm extended and positioned away from the body. To address this, acquiring MR imaging with the patient in the supine position has been proposed, as this configuration is similar to the surgical presentation [95]. Breast MR imaging has been shown to have high sensitivity and accuracy when measuring tumor extent, which is required for the image guidance application [228]. However, even when imaging is acquired in the supine position, the breast can still undergo deformations as large as 70 mm between imaging and surgical positioning due to arm motion, emphasizing the need for an image guidance system (IGS) with deformable correction [18]. While re-imaging the patient continuously could be an option, the encumbrance and cost would prohibit its real-time use. Alternatively, monitoring the surgical field to capture breast shape changes and then using that data to

inform deformable registration algorithms could be a workflow friendly means to establish image guidance for BCS. Previous work focused on a technique for achieving this by measuring the breast geometry with stereo camera monitoring and ink-based surface fiducials [226]. Inked fiducial points and alphabetic letters were written on the breast surface and matched with labeled points in an MR image. These inked fiducials were tracked throughout a range of breast deformations, meaning that the 3D breast surface geometry could be measured noninvasively to inform nonrigid registration for BCS image guidance.

Surgical field monitoring is vital for a BCS-IGS, but just as important is an accurate algorithm for deformation correction utilizing sparse data sources. To address this problem, retrospective studies have been performed to evaluate the accuracy of nonrigid registration methods for breast image-to-physical registration. One of these algorithms is the linearized iterative boundary reconstruction (LIBR) method, first proposed for liver image-to-physical registration and adapted for breast registration [20; 139]. This method employs finite element modeling (FEM) to compute a set of predetermined organ deformations with different boundary conditions. For registration, both conventional rigid registration parameters and the linear combination of these superposed deformation states are iteratively adjusted to minimize the error between sparse breast measurements and their imaged counterparts. Recently, an adaptation to the LIBR algorithm that utilizes regularized Kelvinlet functions for a deformation basis instead of FEM has been explored [19; 213]. Regularized Kelvinlet functions provide closed-form, analytical solutions that model linear elasticity in an infinite medium. Using regularized Kelvinlet functions with the LIBR framework for registration in a BCS-IGS provides a several orders of magnitude reduction in precomputation time, allowing for near real-time registration that compensates for soft tissue deformations in the breast.

In this work, both BCS-IGS components – live stereo camera surgical field sensing and sparse data nonrigid image-to-physical registration – have been integrated to provide active deformation correction. The integrated guidance system features calibrated, co-registered optical tracking and stereo camera monitoring sensors for surgical scene surveillance. A custom user interface and display built in 3D Slicer enables data collection and visualization of patient specific imaging data and models. Finally, data from the surveillance system instantiates a system integrated, nonrigid alignment approach to compensate for soft tissue deformations. While both the surgical field monitoring and nonrigid registration have been demonstrated previously as separate algorithmic developments, this work is the first to showcase full system integration with collected stereo camera data being directly used as input data for near real-time deformation correction performed during the system demonstration. A series of breast phantom deformation experiments are performed to demonstrate guidance system capabilities and feasibility of intraoperative use. Then, the system is used on a healthy volunteer in a mock intraoperative setting to evaluate its potential as a surgical navigation tool. The purpose of this work is to assess if bedside nonrigid registration is feasible for realistic clinical use. The ques-

tion of whether the nonrigid registration reliably achieves adequate accuracy for true procedural guidance is not directly quantified in this work and should be the focus of future study.

VI.4 Methods

VI.4.1 Guidance System Hardware

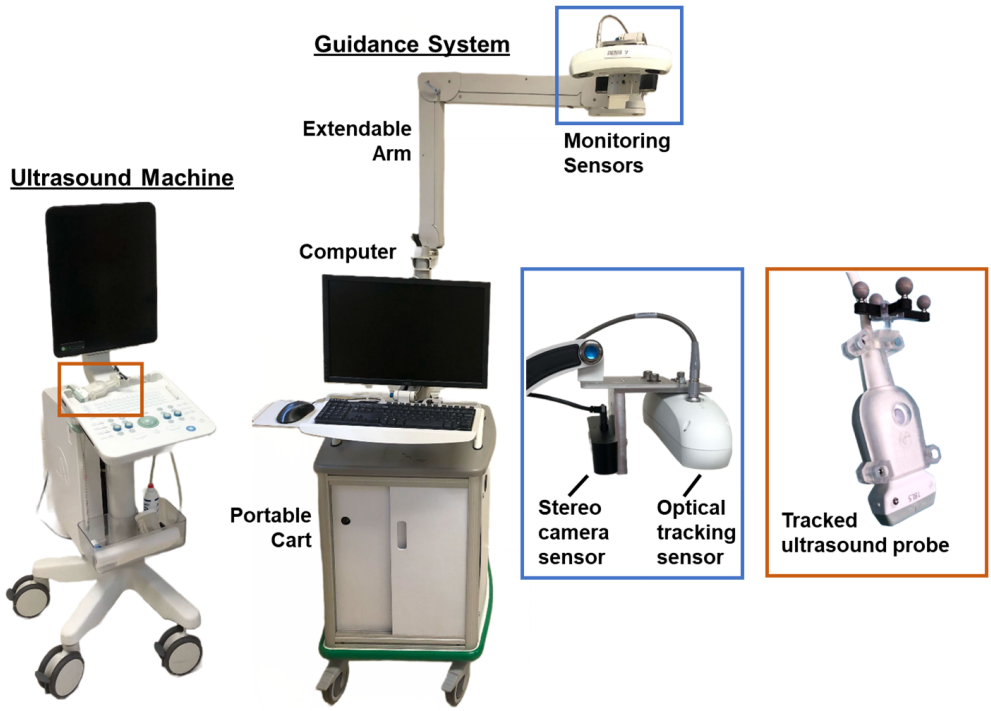

Figure VI.1: The BCS-IGS with labeled components.

The BCS-IGS is shown in Figure VI.1. It features a display monitor, computer, extendable arm, and monitoring sensors mounted on a portable cart that can be positioned for bedside data collection. The extendable arm can be raised approximately 0.75-1.5 m above operating table height, and the arm's multiple degrees of freedom allow for manual adjustment to the best field of view of the surgical scene. The PC computer and display monitor are used to run guidance system module software. The monitoring sensors include both an optical tracking sensor (Polaris Vicra Optical Tracker from Northern Digital Inc., Waterloo, ON, Canada) and a 3D stereo camera sensor (ZED 2i Stereo Camera from Stereolabs Inc., San Francisco, CA, USA) for surgical field monitoring. The optical tracking sensor has a 20 Hz frame rate for tracking up to 6 unique tools with attached reflective passive marker spheres in the field. The 3D stereo camera sensor acquires 3D video at 1080p resolution and a 30 Hz frame rate. Its depth sensing capabilities include a neural depth mode meant to improve depth reconstruction accuracy and completeness. The two sensors offer complementary information for the guidance system. The optical tracking sensor is conventionally used in image guidance systems and

offers live tracking of surgical tools for interaction with the surgical scene. The 3D stereo camera sensor offers noninvasive monitoring of tissue deformation which is useful for BCS where the breast is exposed. Both sensors are rigidly coupled with a custom-made bracket for overlapping field-of-views. A BK5000 ultrasound machine (BK Medical UK, Peabody, MA, USA) and optically tracked 18L5 linear transducer probe can be used with the guidance system to acquire tracked ultrasound imaging.

Both sensors (the 3D stereo camera sensor and the optical tracking sensor) collect spatial data relative to their individual coordinate systems. Prior to data collection, a coordinate space transformation was calculated using a calibration object to co-register the sensor coordinate systems. The calibration object was a 7x8 checkerboard with attached optical tracking passive marker spheres for simultaneous sensor detection [187]. The checkerboard square intersections were tracked in the optical tracking sensor using the attached tracking spheres, and they were tracked in the 3D stereo camera sensor using OpenCV. A separate guidance system module was developed to facilitate this calibration process (see Section III.6.1). Images of the checkerboard placed in 10 locations covering the field-of-view were captured. Conventional least-squares singular value decomposition point-based registration was performed to calculate the rigid transformation between sensor spaces, with a residual fiducial registration root mean squared error value of 1.77 mm [188].

VI.4.2 Guidance System Module

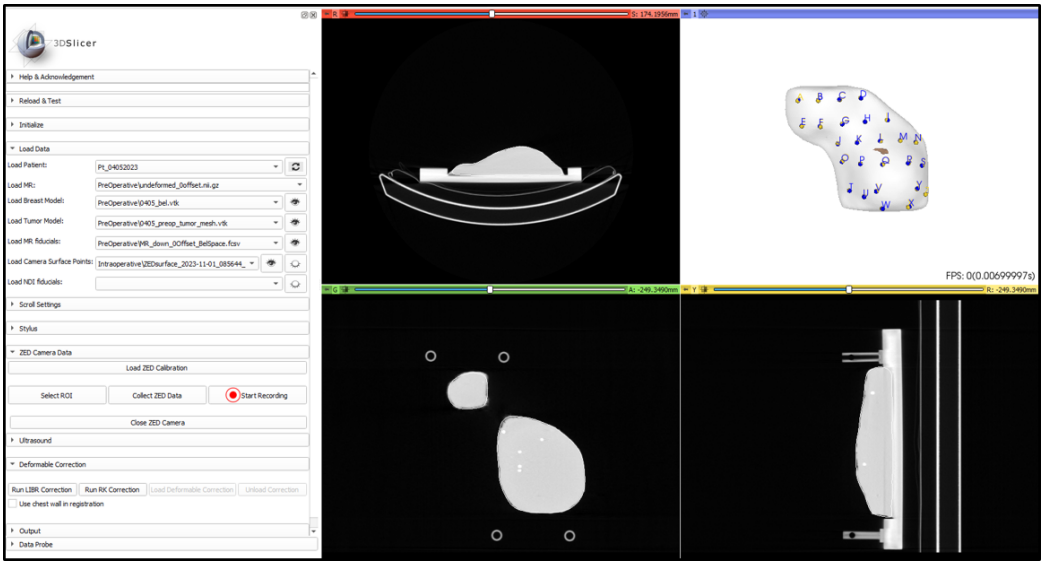

Figure VI.2: The custom guidance module user interface built in 3D Slicer, which includes a control panel (left) and a 4-panel display (right).

A custom user interface and guidance display shown in Figure VI.2 facilitates data collection and navigation for the BCS-IGS. The custom module was built in 3D Slicer [229]. It utilizes functionality developed in

SlicerIGT [230], OpenIGTLink [231], and the PLUS toolkit [232] to stream live data from both sensors into 3D Slicer. It includes user interface panels for (1) loading previously acquired imaging data and 3D models derived from imaging data including the breast model and tumor model, (2) collecting optically tracked stylus point data, (3) collecting stereo camera skin surface and point data, (4) collecting ultrasound data from the optically tracked transducer for ultrasound plane localization, and (5) performing deformation correction between imaging data and sensor data. These panels are displayed on the left pane in Figure VI.2. The guidance screen displays a 4-panel display containing the 3D scene and cross-sectional views of imaging data, which are shown for a silicone breast phantom on the right pane in Figure VI.2. Registered optically tracked tools, 3D stereo camera data, and imaging data enable real-time navigation interaction with the breast anatomy using the guidance system display. This is shown in Figure VI.3, where the 3D scene view showing the breast and tumor models with an optically tracked stylus (Figure VI.3A) is synced to the stereo camera data stream (Figure VI.3B). The distance between the stylus tip and tumor boundary is updated and displayed as the user moves the stylus. The tracked ultrasound capabilities are shown in Figure VI.4. During active imaging, the guidance module displays the B-mode ultrasound image and the imaging plane's 3D orientation relative to the breast and tumor models. The tracked ultrasound is calibrated using the N-wire ultrasound calibration technique [189]. The module facilitates data collection and guidance visualizations in test and surgical settings.

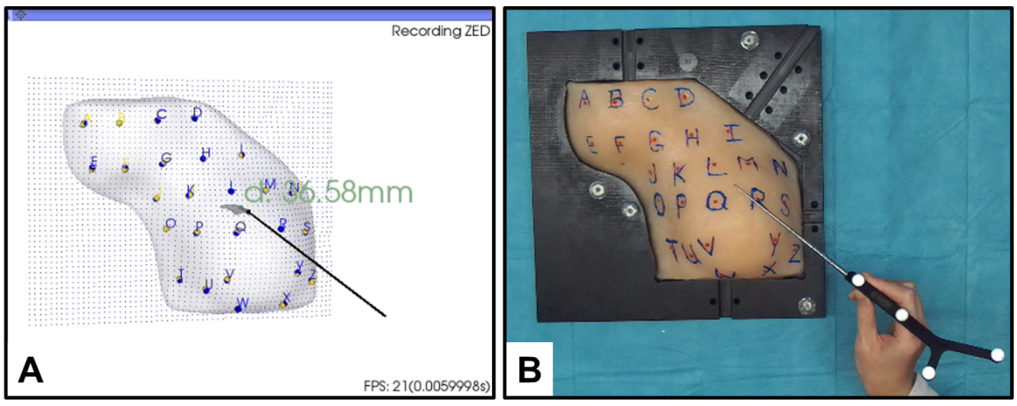

Figure VI.3: Guidance system navigation with an optically tracked stylus showing (A) the 3D scene view and (B) the left stereo camera image view. The 3D scene view includes the fiducials measured from imaging data (yellow letters), the fiducials measured from stereo camera data (blue letters), stereo camera point-cloud (blue), mock tumor (dark gray), breast phantom model (light gray), and stylus (black). Distance from stylus tip to mock tumor is displayed in green.

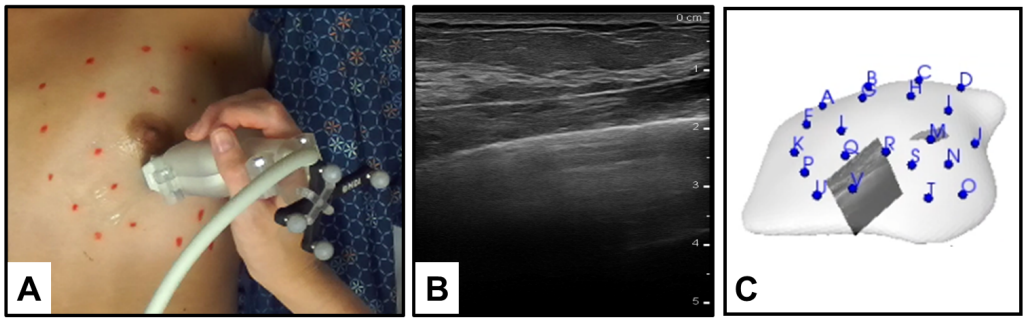

Figure VI.4: Guidance system tracked ultrasound capabilities with (A) active breast ultrasound imaging, (B) a collected B-mode image, and (C) the 3D scene view with the tracked ultrasound imaging plane.

VI.4.3 Deformable Correction

The guidance system requires a preoperatively acquired imaging volume of the breast anatomy to use in the 4-panel display. The breast and tumor geometries are segmented from this imaging volume to generate the 3D anatomical models used in the 3D scene view. However, nonrigid deformations occur between the imaging and surgical positions, meaning that aligning the imaging and 3D models to the physical scene with rigid registration alone is not sufficient for accurate navigation. Deformation correction is employed in the guidance module to augment the imaging data, the 3D breast model, and the 3D tumor model to better match the stereo camera sensor data collected in shape-change states. By doing so, the imaging data used for guidance can account for shape differences between the imaging position and the surgical positions.

To create a set of possible breast deformations to use for registration, regularized Kelvinlet functions were employed as deformation basis functions. These functions, previously used for digital sculpting, provide a closed-form solution to a linear elastic tissue response to a regularized point force in an infinite medium [19]. They can also be linearly scaled and superposed to create many different deformed geometries. $k = 45$ regularized Kelvinlet functions were centered and evenly distributed on the posterior chest wall surface of the 3D breast geometry using k-means clustering. Each regularized Kelvinlet function was parameterized with mechanical tissue material properties (Young's modulus $E = 2100$ Pa, Poisson's ratio $\nu = 0.45$) and a radial relaxation parameter $\varepsilon = 0.05$. More details about this method and its implementation for breast registration are available in previous work [213]. To calculate a displacement field that registers the imaging data to physical sparse-data inputs, the linearized iterative boundary reconstruction (LIBR) method was employed [20; 139]. This method computes the optimal linear scaling vector for each of the regularized Kelvinlet forcing functions that minimizes alignment error using Levenberg-Marquardt optimization. For this registration, the same objective function $\Omega(\boldsymbol{\beta})$ introduced in Chapter V is used. It is reprinted in Equation VI.1 below:

$$\Omega(\boldsymbol{\beta}) = \frac{1}{n_{point}} \sum_{i=1}^{n_{point}} (e^i_{point})^2 + \frac{1}{n_{surface}} \sum_{i=1}^{n_{surface}} (e^i_{surface})^2 + w_{SE}(e_{SE})^2 \tag{VI.1}$$

This objective function relies on acquiring specific data from the 3D stereo camera sensor, namely breast surface fiducial points that correspond to fiducial points labeled in the preoperatively acquired imaging volume and an intra-fiducial breast surface point cloud that represents the breast surface geometry. In Equation VI.1, $\boldsymbol{\beta}$ is the parameter vector that represents the deformation field, e^i_{point} is the distance error for each surface fiducial i, n_{point} is the number of surface fiducial points, $e^i_{surface}$ is the normal projected distance error for each surface point-cloud point i, and $n_{surface}$ is the number of surface point-cloud points. To penalize high strain energy deformations, the objective function also includes e_{SE} which is the strain energy of the deformation, and w_{SE} is a strain energy weighting factor which is set to 10^{-9} Pa^{-2}.

In some of the registrations, an additional term from tracked ultrasound data is included in the $e_{surface}$ error term. Tracked ultrasound imaging is collected and the chest wall is segmented from B-mode imaging. This sparse chest wall sampling is used to constrain the posterior region of the breast imaging volume by minimizing the normal projected distance error from the segmented ultrasound data to the chest wall surface on the breast model.

Registration is initialized with a point-based rigid registration between the imaging data fiducial points and the stereo camera fiducial points [188]. The 3D stereo camera sensor is acquired and saved with a button-click in the guidance module. Then, the deformable correction algorithm is initiated with another button-click in the guidance module, using the imaging data and stereo camera data as inputs. Once registration is complete, the deformed image volume and 3D geometry models are automatically loaded into the guidance module. The runtime for deformable correction is variable, depending on the time to convergence for each specific input data configuration. In the previous work where this algorithm was presented, registration took 14 seconds computed on a single thread of a 3.6 GHz AMD Ryzen 7 3700X CPU [213]. Similar computation times were observed when running the algorithm in the guidance system. To evaluate accuracy after registration, fiducial error was measured as the distance between the deformed imaging data fiducials and the stereo camera fiducials. Projected surface error was also measured as the normal-projected distance between the imaging data model surface and the stereo camera intra-fiducial surface point cloud. It should be noted that although these measurements describe surface alignment, they are not an adequate surrogate for measurements that quantify target accuracy. Investigation into subsurface target accuracy was explored in previous work with simulated surgical scene data [139; 213].

VI.4.4 Phantom Experiment

To demonstrate guidance system feasibility for surgical scenarios, a series of experimental tests were performed using a breast deformation phantom. The breast phantom was constructed of 75% Ecoflex 00-10 platinum cure silicone rubber, 12.5% silicone rubber thinning fluid, and 12.5% tactile mutator (Smooth-On Inc., Macungie, PA, USA). The phantom shape was modeled after the Breast Probe Model for breast ultrasound training from Simulab (Simulab Corporation, Seattle, WA, USA). 26 red-ink fiducial markers were placed on the phantom surface to mimic skin fiducials that have been proposed for skin surface tracking in previous work [226]. These red-ink fiducials were placed on top of red glass beads so that they were visible in stereo camera imaging and CT imaging. CT imaging data of the phantom with a voxel size of 0.65 x 0.65 x 0.67 mm^3 was obtained to create the imaging data and 3D mesh model to use in the guidance system. The breast geometry was segmented from the CT imaging volume using ITK-SNAP, and the fiducial points were manually labeled. A 3D mesh generation software was used to create a mesh model from the image segmentation [203]. A 3D mock breast tumor model was placed in the breast phantom model in the guidance system for demonstration purposes. All of these experimental setup and data preprocessing steps were performed prior to mock intraoperative data collection.

For data collection, the phantom was placed in a rig that applies deformations in four sections where the breast tissue would intersect with surrounding tissues in vivo. In the undeformed and each of the four deformation states, stereo camera data was collected using the guidance system. Color channel-based image processing methods outlined in previous work were utilized for automatic fiducial point detection [226]. Fiducial points were manually labeled with an alphabet letter, and falsely detected points were corrected with a GUI in the guidance system if necessary. Using the ZED SDK for Python (PyZED), 3D stereo camera data consisting of the 3D fiducial point coordinates and the intra-fiducial surface point cloud were displayed in the guidance system and used for deformable correction. After each stereo camera data capture, deformable correction was initiated. Once completed, the deformed images and 3D models were displayed in the guidance system and fiducial and surface errors were measured. Tracked ultrasound was not collected in this experiment.

VI.4.5 Volunteer Demonstration

One healthy female volunteer was enrolled in a study approved by the Institutional Review Board at Vanderbilt University to test the BCS-IGS in a mock intraoperative setting. Prior to the mock intraoperative data collection session, supine MR breast imaging was collected. 26 MR visible fiducials were placed on the left breast skin surface. The center of each fiducial was marked with a semi-permanent red ink marker pen. The volunteer was positioned in a supine position with the ipsilateral arm down by her side, and a 32-channel torso

coil was placed over the breast. A Phillips 3.0 Tesla closed bore scanner was used to acquire a fat suppression mDixon scan of the left breast with a voxel size of 0.4375 x 0.4375 x 1 mm^3. After image acquisition, the breast geometry was segmented at the chest wall boundary using ITK-SNAP, and a 3D model was created with mesh generation software like in the phantom experiment. A mock 3D tumor model was placed in the upper outer quadrant for demonstration purposes. Image acquisition and preprocessing were performed two days before the mock intraoperative session.

For data collection and guidance system demonstration, the volunteer was positioned in the supine position with the ipsilateral arm extended in a T-shape to mimic surgical positioning. The guidance system extendable arm was positioned over the left breast. 3D stereo camera data was acquired with the same fiducial point detection methods used in the phantom experiment, and deformable correction was performed. The optically tracked stylus was used to swab the breast surface and measure distance to the mock tumor after registration. The stereo camera and guidance system monitor streams were recorded during navigation, and fiducial and surface errors were measured. Six tracked ultrasound images were collected and the chest wall was manually segmented in these images. Deformable correction was performed both with and without tracked ultrasound data for comparison.

VI.5 Results

VI.5.1 Phantom Experiment Results

Data collection and deformable correction using the guidance system for the undeformed and 4 deformation states are displayed in Figure VI.5. The left camera stereo images in Figure VI.5A show the deformation states with the breast phantom rig. The collected stereo camera point fiducials and intra-fiducial surface point cloud are rigidly registered to the imaging data fiducials (black) and imaging data model (gray) in Figure VI.5B. The breast models and mock tumor models from the 4 deformation states after deformable correction are shown in Figure VI.5C, which qualitatively match the applied deformations shown in Figure VI.5A. Evaluation results are presented in Table VI.1. For all 4 deformation states, fiducial error and projected surface error decreases after deformable correction as compared to rigid registration. This is expected, given that the fiducial error and projected surface error terms are both minimized in the objective function $\Omega(\boldsymbol{\beta})$.

Table VI.1: Evaluation results for breast phantom deformation experiments. Avg $\pm$ std (maximum) mm.

	Fiducial error (mm)		**Projected surface error (mm)**	
	Rigid	**Nonrigid**	**Rigid**	**Nonrigid**
Undeformed	1.7 ± 0.6 (2.9)	-	1.1 ± 0.8 (5.1)	-
1	3.5 ± 1.4 (6.8)	0.9 ± 0.4 (1.6)	1.4 ± 1.3 (7.7)	0.7 ± 0.7 (5.9)
2	5.0 ± 2.6 (13.0)	1.0 ± 0.5 (1.9)	1.8 ± 1.6 (8.8)	0.8 ± 0.7 (6.5)
3	2.6 ± 1.1 (4.9)	1.0 ± 0.5 (2.8)	1.6 ± 1.3 (8.5)	0.7 ± 0.7 (8.4)
4	3.4 ± 1.6 (7.2)	1.0 ± 0.5 (2.5)	2.0 ± 1.4 (8.6)	0.6 ± 0.6 (7.1)

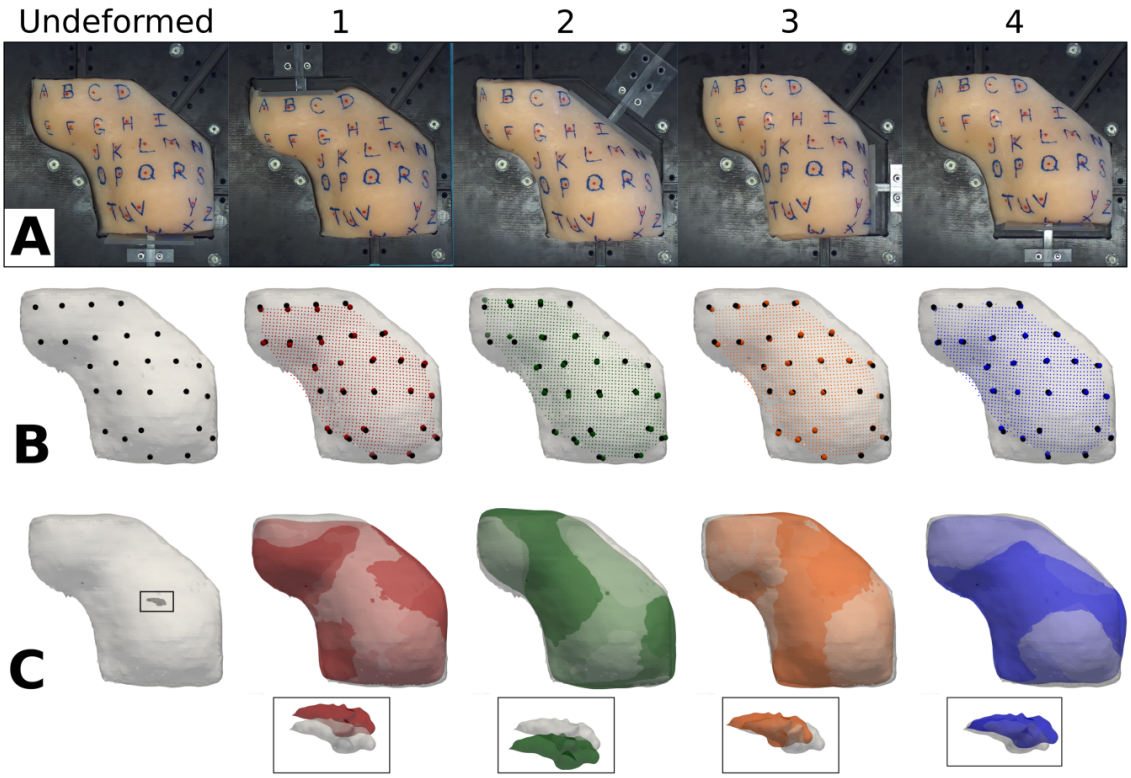

Figure VI.5: Visualization of breast phantom deformations. (A) Left stereo camera images of the breast phantom. (B) Imaging data breast model (gray) and fiducial points (black) with rigidly registered collected stereo camera fiducial and intra-fiducial point cloud data for deformation states 1-4 in red, green, orange, and blue respectively. (C) Post-deformation correction breast and tumor models for states 1-4 overlayed on undeformed models (gray).

VI.5.2 Volunteer Demonstration Results

Three timepoints from the BCS-IGS demonstration on a healthy volunteer are shown in Figure VI.6 both with and without tracked ultrasound data. The guidance system display shows successful image and model alignment to the 3D stereo camera data. As the optically tracked stylus swabs the breast surface, the displayed distance to the mock tumor surface updates according to the deformed tumor model. The stylus also controls the deformed image volume axial slice shown in the 4-panel display. The 3D scene view provides a view of the stylus relative to the breast and tumor models. Like in the phantom experiment, fiducial error and projected surface error decreases after deformable correction shown in Table VI.2.

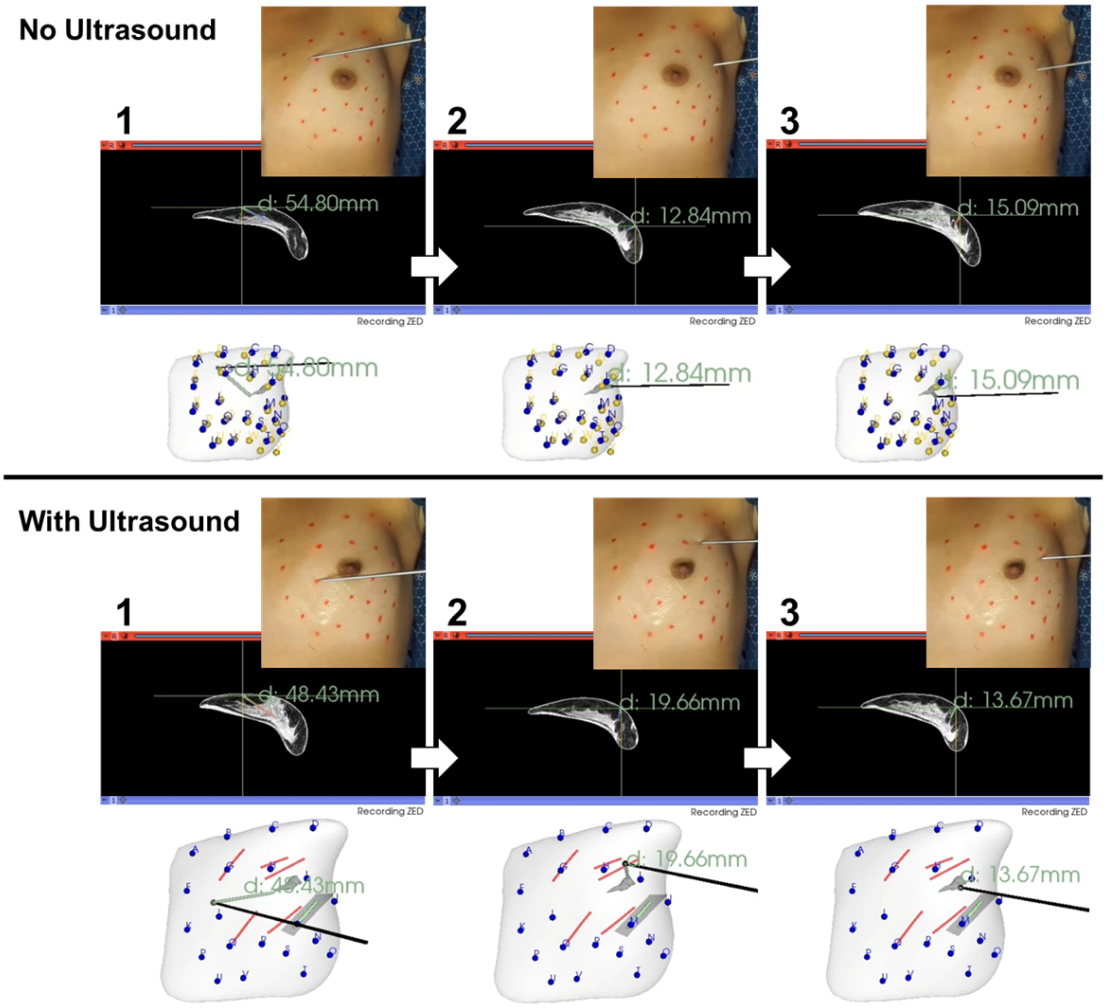

Figure VI.6: Guidance system views showing three timepoints during the healthy volunteer demonstration with and without tracked ultrasound data. Synced left stereo camera images, axial MR image slices, and the 3D scene view are displayed. The MR image, breast model, and tumor model are registered to stereo camera data of the breast geometry. The distance from the stylus tip to the mock tumor boundary during navigation is displayed in green.

Table VI.2: Evaluation results for volunteer demonstration. Avg $\pm$ std (maximum) mm.

	Fiducial error (mm)	**Projected surface error (mm)**
Rigid	7.3 $\pm$ 3.3 (18.6)	1.2 $\pm$ 1.0 (5.7)
Nonrigid (no US)	2.0 $\pm$ 0.9 (4.0)	0.4 $\pm$ 0.3 (2.2)
Nonrigid (with US)	3.4 $\pm$ 1.6 (8.3)	2.0 $\pm$ 1.3 (6.8)

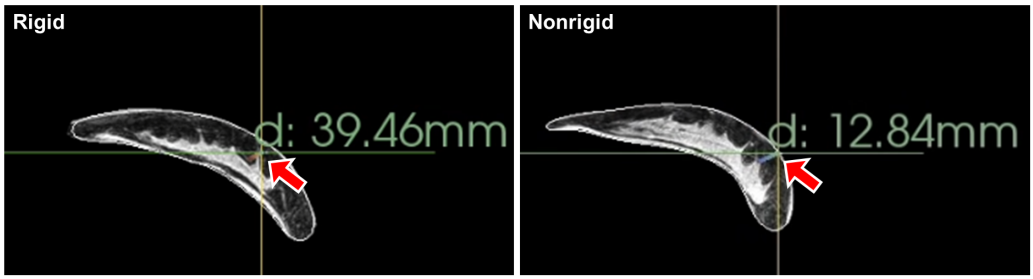

Figure VI.7: Guidance system axial MR imaging views before deformation correction (left) and after deformation correction (right).

A comparison between rigid and nonrigid alignment was also tested in the BCS-IGS. The stylus tip was placed on the volunteer's breast surface, and the axial MR imaging view was captured. Figure VI.7 shows these views, with the axial MR image on the left captured before deformation correction and the right captured after deformation correction. The crosshairs better align to the breast surface after deformation correction compared to rigid alignment.

VI.6 Discussion

Both the phantom experiment and healthy volunteer demonstration showcased an effective BCS-IGS approach. The guidance system hardware includes a portable cart with mounted overhead sensors for surgical scene monitoring. The guidance system module features a user interface to streamline data collection and deformable correction in a surgical setting. The phantom experiment and volunteer demonstration required using the 3D stereo camera sensor to collect data, and then using this data as the input to a deformable correction algorithm. Successful completion of data collection and near real-time deformable correction in these mock intraoperative settings demonstrates that the guidance system is compatible with surgical workflows.

Regarding limitations, one limitation of the presented experiments is the lack of subsurface validation for measuring deformable correction accuracy. In both the phantom and volunteer experiments, registration accuracy was measured by calculating breast surface errors. While these measures indicated correction on the breast surface, having an accurate registration at the site of the tumor is most important for navigation purposes. In previous work, subsurface accuracy was evaluated by acquiring supine breast MR images of healthy volunteers in an arm-down position and labeling targets in the breast parenchyma based on the tissue glandular features. Then, a second MR image in an arm-up position was acquired, and registration-predicted target locations were compared to imaged target locations. These studies showed acceptable deformable correction subsurface accuracy with the same registration algorithm used in this guidance system [139; 213]. However, these previous studies used simulated surgical scene data rather than actual surgical scene data acquired from a 3D stereo camera. Future studies should include rigorous nonrigid registration accuracy

evaluation to ensure that the proposed guidance system is suitable for BCS procedural requirements. Another limitation is the fact that the system was demonstrated on only one healthy volunteer. Recruiting more volunteers and breast cancer patients for study participation is important for further demonstrating guidance system utility and is the focus of ongoing work.

VI.7 Conclusion

This work demonstrates the feasibility of a novel BCS-IGS for improving navigation and tumor localization during procedures. The system features both an optical tracking sensor and a 3D stereo camera sensor for surgical scene monitoring and data collection. Using the collected geometric sensor data for deformation correction enables alignment between the imaging data and the surgical scene, which is vital for guidance in soft-tissue organs such as the breast. The rapid advancements in computer vision and computational technologies have made image guidance in BCS an achievable goal. Looking ahead, the effects of using such a system on clinical outcomes has yet to be studied, but this work puts forth a promising solution that may unlock new capabilities in surgical precision and reduce reoperation rates for BCS procedures.

Acknowledgements

This work was supported by the National Institutes of Health through Grant Nos. R01EB027498 and T32EB021937, the National Science Foundation for a Graduate Research Fellowship awarded to M.J. R., and the Vanderbilt Center for Human Imaging supported by Grant No. 1S10OD021771-01 for the 3T MRI.

CHAPTER VII

Future Directions

This dissertation highlights progress towards developing an image guidance system for breast surgeries. However, nontrivial challenges persist in achieving clinical translation and realizing its full potential. This section outlines two key areas for future development of the guidance system. The first is investigating alternate system hardware designs to minimize workflow interruption in surgery. Although the current system design sufficed for this dissertation and initial testing, future revisions of the cart overhead arm and display monitor could improve data collection and guidance visualization. The second is expanding registration capabilities to accommodate updates during the surgical procedure. While the initial emphasis was on tissue monitoring before invasion and excision, this restricts guidance and tumor localization to the planning stage of the procedure. Future work should investigate nonrigid registration methods that could be applied after incision, which would expand the system's potential use. Finally, the new methods presented here may have applications outside of breast surgery. Other potential use cases for the regularized Kelvinlet functions in medical imaging are discussed.

VII.1 System Design

As described in Section VI.4.1, the image guidance system includes a portable cart with an overhead surgical arm, display monitor, and computer. This design was informed by previously developed research grade image guidance systems and met the needs for the volunteer studies conducted in this work. Future system designs should be informed by the needs and constraints of using the system during surgery. To inform the system design improvements proposed here, the image guidance system was brought into the operating room and used for data collection during lumpectomy surgeries. Two patients undergoing breast conserving surgery were enrolled in a study for developing an image-guided lumpectomy system approved by the Vanderbilt Institutional Review Board. One patient was a 37-year-old woman undergoing a right lumpectomy, and one patient was a 73-year-old woman undergoing a left lumpectomy. Supine MR imaging with skin fiducials was not acquired for these patients. The guidance system cart was set up in the operating room after the patient was anesthetized but before the field was sterilized. Stereo camera video and depth point cloud data were recorded during key portions of the procedure. Because supine MR imaging was not acquired, it was not possible register MR imaging to the surgical field and test tumor localization with the system guidance module. Instead, this preliminary data acquisition was meant to test guidance system data acquisition in the operating room and steer future system development. These data acquisition sessions highlighted system

usability challenges that were not evident during volunteer studies, and potential system design solutions to address these challenges are presented in this section.

VII.1.1 Overhead Surveillance Positions

The current guidance system features an adjustable overhead surgical arm. This configuration allows for the mounted surveillance sensors to be manually adjusted to provide the best view of the surgical scene. In the volunteer studies, the guidance system and ultrasound machine were positioned directly next to the volunteer with one additional person as the guidance system user and no additional equipment. During preliminary system testing in the operating room, there were more constraints on positioning the guidance system than during volunteer studies. At times, there were up to four people assisting with the operation – the attending surgeon, resident surgeon, surgical technician, and medical student. Having up to four people assisting with the operation led to more field of view obstructions throughout the procedure than anticipated. Also, there were other equipment carts that needed to be positioned next to the patient during the procedure. These carts included an intraoperative ultrasound machine, the headlamp light source mounted on a rolling stand, the magnetic seed localization system cart, and the sterile tray. In practice, the positioning of these carts during the procedure limited the guidance system view. These factors made it difficult to constantly adjust the overhead arm throughout the procedure to acquire surgical field depth measurements. The tested guidance system configuration in the OR and camera views displaying both unobstructed and obstructed views are shown in Figure VII.1.

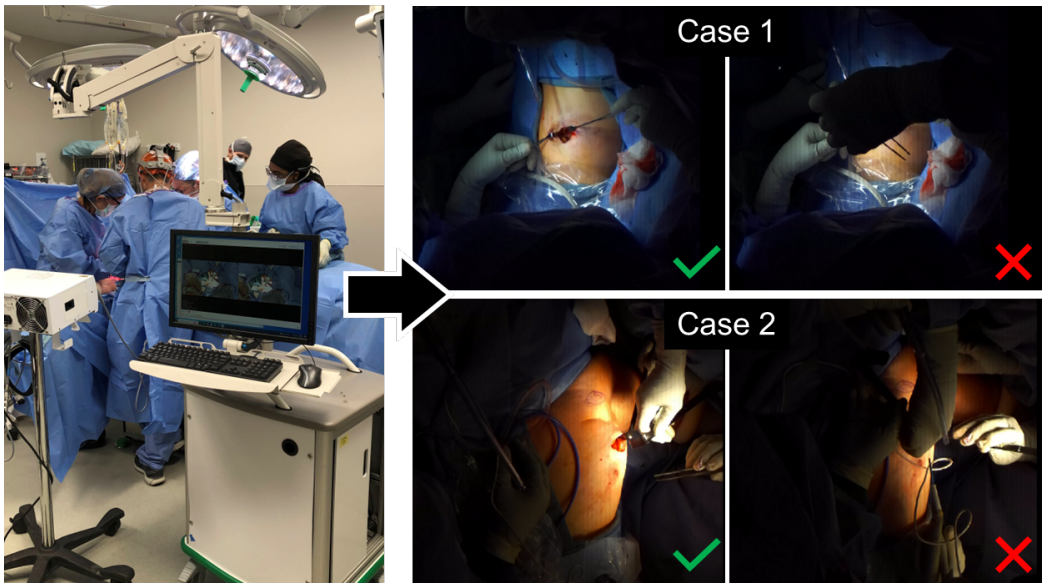

Figure VII.1: Tested guidance system setup during breast surgery. Camera views display unobstructed (middle) and obstructed (right) views during different timepoints of the procedure.

For future development, alternative overhead surveillance positions that improve the guidance system field of view should be explored. One possible surveillance position may be to position the guidance system cart at the patient's head. The adjustable overhead arm would be positioned over the sterile drape that separates the surgical field and anesthesia. This positioning may be able to offer a less obstructed view of the surgical scene. This configuration would need to be tested to ensure that the guidance system footprint does not interfere with the anesthesia equipment. Some commercially available surgical overhead lighting products, like the StrykeCam HD (Stryker Corporation, Kalamazoo, MI, USA) and the 7D Surgical System (SeaSpine, Carlsbad, CA, USA), offer integrated camera mounting where a camera is rigidly attached to the center of one of the overhead surgical lights. These setups allow for unobstructed overhead views of the surgical field. Another possible configuration for the guidance system would be to design a mounting bracket that could attach the surveillance sensors to the overhead surgical light. This viewpoint may offer a better vantage point for collecting depth measurements and localizing tracked tools in the field. Finally, one of the reasons why acquiring a continuously unobstructed view is challenging is because lumpectomy surgeries are dynamic. The surgeons frequently manipulate and reposition the breast throughout the procedure. To truly adapt to the dynamic field, a third alternative configuration could be to mount the surveillance sensors to a robotic arm whose position could be easily adjusted during surgery. For this configuration, repositioning the field of view would not rely on an additional operator to manually move the overhead arm during the procedure. Instead, the surgical scene could be tracked, and the positions of the surveillance sensors adjusted automatically to prevent scene obstructions. While automatic sensor repositioning would be optimal from a workflow perspective, even a robotic arm that is passively updated by an additional operator through a software interface would be an improvement compared to having to manually adjust the overhead arm. Robotic arms that may be well suited for this application include the LBR Med 7 R800 robot from KUKA (KUKA, Augsburg, Germany) and the VS-S2 Series robot from DENSO Robotics (DENSO Robotics, Long Beach, CA, USA). These models have either been used in surgical applications or been approved for medical device use cases, and they offer working volumes with enough degrees of freedom to correct for obstructions in the field.

VII.1.2 Display Visualization

Currently, the guidance module features a 4-panel display for visualization. The 4 panels show either the MR axial, sagittal, and coronal views and a 3D rendering view, or the MR coronal view is replaced with the live ultrasound imaging feed view. The settings panel is displayed on the left of the screen. While adequate for initial testing and data collection, these display options should be revisited so that they are more informative for intraoperative guidance. Preliminary qualitative feedback from users suggests that the additional sagittal

and coronal MR panels do not add much value for tumor localization. Primarily, users report relying on the axial MR panel and the 3D rendering view to orient themselves spatially and use the guidance system. Thus, a more optimal display may be a 2-panel display that features just these views. A user study that asks users to locate a mock tumor with the guidance system in a breast phantom and mark the incision location could be conducted to better inform these system design considerations.

In the present system, the display monitor is rigidly attached to the base of the cart, which limits the display monitor positioning in the OR. A display monitor mounted on a separate stand may be more convenient for surgeons using the guidance system. Utilizing existing but unused display monitors available in the OR may be another convenient option for displaying the guidance system module. Both options should be explored as more end users test the guidance system in OR studies.

VII.1.3 Augmented Reality

The system display presented in this work requires the user to divert their gaze from the surgical field to view the guidance system module on a monitor. Having a display monitor for the navigation system requires the surgeon to split focus between the display monitor and the surgical field. This user experience has been shown to distract from the surgical workflow and increase cognitive load [233]. Alternative display solutions should be explored to improve usability. Augmented reality (AR) devices offer head mounted optical see-through displays that are placed in front of the user's line of sight. Using stereoscopy, these displays render holograms as if they were present in the physical environment. They can show virtual elements that are superimposed on top of the surgical field. Internal spatial sensors track the device's location and allow the 3D rendered holograms to appear stationary to the user, which creates immersive visualizations overlayed on the physical environment. Commercially available AR devices that have been explored for surgical applications in recent years include the Microsoft HoloLens (Microsoft Corporation, Redmond, WA, USA), Magic Leap (Magic Leap, Plantation, FL, USA), and Moverio Smart Glasses (Epson America, Inc., Long Beach, CA, USA), although the HoloLens is the platform of choice for the vast majority of research papers published about AR for surgical guidance [234]. For the BCS guidance application, AR may offer benefits demonstrated in other surgeries by previous studies. These benefits include better perception, reduced cognitive workload, and improved usability [235].

Two potential AR display options could be investigated to advance this guidance system. The first proposed AR display features the same 4-panel display overlayed as a semi-transparent 2D screen in the top right corner of the user's field of view, analogous to a picture-in-picture view (Figure VII.2A). This display option would present the guidance system display in the surgeon's peripheral vision for them to easily reference when needed, while not obstructing the surgical field of view. This consistent display view is not

easily achievable when using a monitor in a crowded operating room. The second proposed display would take full advantage of AR capabilities by projecting the 3D rendering view registered to the breast (Figure VII.2B). Overlaying the 3D breast and tumor models directly onto the anatomy in the physical scene so that surgeons can see the tumor shape and location in 3D space may improve spatial reasoning compared to using the 3D rendering view with a monitor and tracked stylus. Other AR visualization variations could include a 2-panel picture-in-picture view that would obstruct less of the visual field, or trajectory visualizations that embed 3D spatial information without full 3D model overlays. Currently, the commercially available AR devices on their own have spatial localization errors on the order of several centimeters, which is inadequate for many clinical registration needs. AR devices used in combination with an external optical or electromagnetic tracker have been shown to correct localization errors to millimeters instead of centimeters, which is acceptable for surgical guidance tasks [236]. Future AR device advancements may improve localization errors such that external tracking devices are no longer needed for millimeter-scale accuracy [237]. While AR for surgical guidance holds promise as a tool for improved visualization, the clinical value of the technology has yet to be demonstrated. Because many surgical AR studies are conducted in the pre-clinical setting, there is little evidence of improved patient outcomes when using AR devices compared to traditional surgical methods [238].

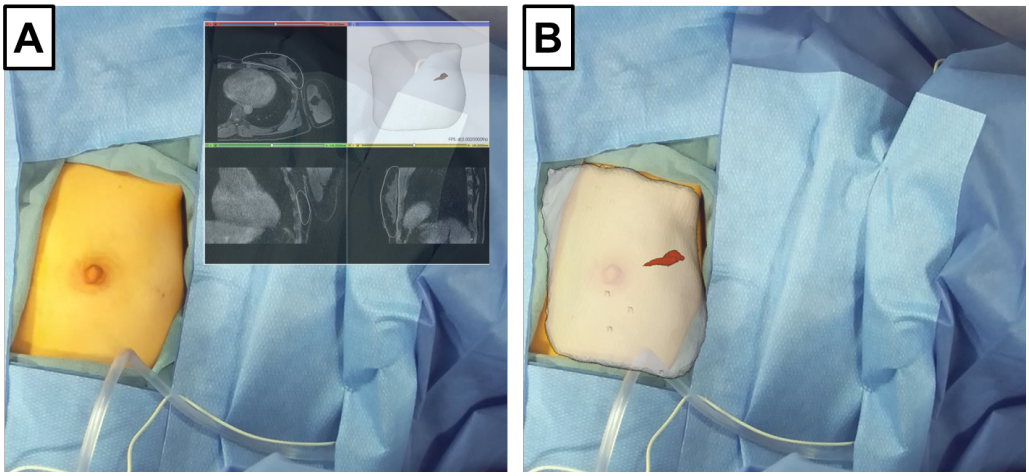

Figure VII.2: Proposed guidance system with AR. (A) Mock-up of AR system with 4-panel display in top right corner. (B) Mock-up of AR system with overlayed 3D breast and tumor models.

VII.2 Intraprocedural Guidance System Use

The current guidance system offers nonrigid registration to correct for breast shape change between imaging and surgical positions. The proposed nonrigid registration method, outlined in Chapter V, deforms preoperative models and imaging for better alignment to the breast shape in the operating room. This alignment

may be useful for visualizing the tumor location and extent during the planning stage of surgery when the surgeon marks the incision location. However, the presented nonrigid registration method depends on collecting a breast skin surface point cloud and breast skin fiducial points before tissue incision and invasion. This method is not designed for intraprocedural updates. Nonrigid registration to compensate for deformations after tissue incision and invasion has not been thoroughly explored. This means that in its current state, the guidance system cannot be used to reliably locate the tumor during the procedure. Methods that expand the nonrigid registration capabilities so that the breast model, tumor model, and preoperative imaging can be aligned to the surgical field during the surgery would enable true intraprocedural image guidance. This capability may allow for better tumor localization through continual updates, rather than localization only during the planning stage of the procedure. Nonrigid registration methods that can accurately account for surgical dynamics and intraprocedural breast deformations may improve the utility of the guidance system and should be pursued in future work. Preliminary investigation into (1) the nature of the intraprocedural point clouds, (2) registration method alterations to accommodate incision, and (3) presenting margin predictions after resection are presented in the following sections.

VII.2.1 Intraprocedural Data Collection

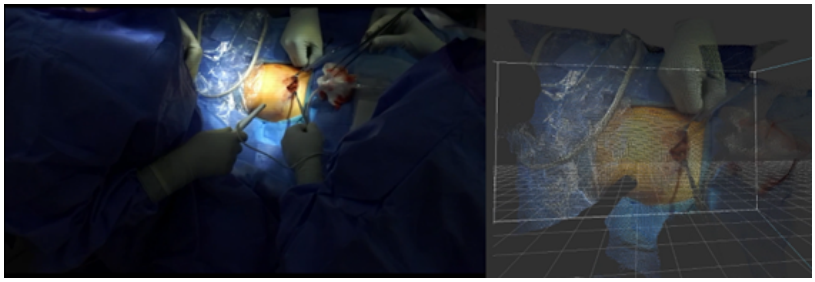

Figure VII.3: Sample intraprocedural breast surface point cloud data with a skin surface and dissection cavity point cloud.

Intraoperative sparse data sources collected for the work in this dissertation include a breast skin surface point cloud, breast skin fiducial points, and a chest wall surface point cloud acquired with tracked ultrasound. During the procedure, the breast skin surface point cloud changes due to incision and surgical dynamics. Instead of a smooth skin surface, this point cloud contains the skin surface and the dissection cavity. Intraprocedural data collection capabilities were explored during the preliminary data acquisition study in the operating room. An example breast surface point cloud acquired after incision but before specimen excision is shown in Figure VII.3. The presented breast surface point cloud was extracted at a moment in the procedure which had minimal obstructions from surgical tools in the field. Even so, acquiring breast surface point clouds without obstructions was difficult due to the challenges outlined in Section VII.1.1 and the dynamic nature

of these procedures. Nevertheless, the breast surface point cloud in Figure VII.3 shows both the breast skin surface and a point cloud representation of the dissection cavity. In future work, configurations for collecting reliable intraprocedural point cloud data should be explored. This may involve briefly pausing the procedure and having the surgeons remove their tools and retractors from the field to acquire data for a guidance system update. Alternatively, if the intraprocedural point cloud data is not reliable, surface data could be collected by sweeping a tracked stylus over the area of interest. Further investigation into the variability and reliability of these data collection methods is needed in future work to assess the feasibility of intraprocedural image guidance.

VII.2.2 Registration Methods After Incision

Achieving intraprocedural guidance system updates not only relies on data collection, but also on having registration methods to accommodate surgical dynamics like retraction and dissection. Methods for post-incision registration with simulated intraprocedural data have been investigated with preliminary phantom experiments [10]. The methods and results from these investigations were presented in a conference paper at SPIE Medical Imaging in 2023. Parts of this section are adapted and reprinted with permission from,

[10]: A. Espinosa, M. J. Ringel, J. S. Heiselman, K. Pereira, F. Servin, W. L. Richey, I. Meszoely, and M. I. Miga, "Modeling retraction for breast conserving surgery guidance," in *Proceedings of SPIE Medical Imaging,* vol. 12466, 2023.

In the phantom experiments, an incision phantom (Figure VII.4), was constructed from 75% Ecoflex silicone mixed with 12.5% silicone thinner and 12.5% slacker tactile mutator. The phantom shape was modeled after the Breast Probe Model for breast ultrasound training from Simulab (Simulab Corporation, Seattle, WA, USA). 26 surface fiducials and 39 subsurface targets were used, with 11 of these 39 targets concentrated in one area to mimic a tumor. The incision was cut in the medial-lateral direction, and the tissue was retracted in the inferior-superior direction. The preliminary retractor rig was 3D printed and secured to a rigid board for imaging. High resolution CT images of the breast phantom in the undeformed and retracted states were acquired with an image voxel size of 0.65 x 0.65 x 0.67 mm.

This phantom was used to explore a potential post-incision registration method, which was adapted from the LIBR method outlined in Chapter V. An incision plane that represented the retraction phantom incision cut was used to split the mesh. A mesh-splitting technique where nodes on either side of the incision plane were duplicated was used to separate the domain [239]. The LIBR method with a FEM displacement basis was used to reconstruct retraction conditions. Eight control points were placed on the inside surface of the incision cavity with four control points on either side of the incision plane. Five additional control points were placed

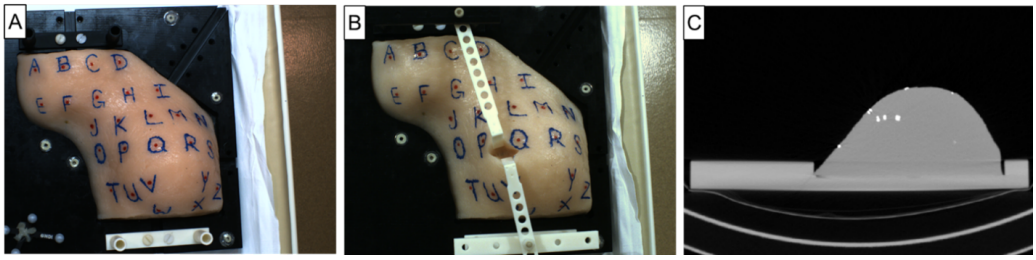

Figure VII.4: Breast phantom for modeling retraction in the (A) undeformed state without retractors and (B) in the retracted state. (C) An example CT image slice of the phantom with the embedded subsurface targets and surface fiducial beads.

on the posterior surface of the phantom which is consistent with a previous implementation of the LIBR method for modeling breast deformations [139]. Displacement modes were computed as FEM forward-solve, homogeneous isotropic elastic boundary value problems with Young's Modulus $E = 2100$ Pa and Poisson ratio $\nu = 0.45$. The optimal linear combination of the displacement modes generated from these 13 total control points that minimized the distances between the model retracted surface fiducial bead locations and the measured retracted surface fiducial bead locations was found using Levenberg-Marquardt optimization. A strain energy regularization term was also included in the optimization to penalize deformations with high strain energy.

Fiducial registration error (FRE) using the phantom surface beads and target registration error (TRE) using the phantom subsurface beads were calculated to evaluate model performance. Given that retraction is a local deforming event, FRE and TRE measurements were limited to a region of interest (ROI). Using an ROI designated as a sphere with a 40 mm radius centered at the incision midpoint, 3 surface beads and 12 subsurface beads were found to fall in the ROI sphere. The FRE after retraction modeling of the 3 surface beads in the ROI was 0.5 ± 0.1 mm with a maximum of 0.5 mm. The TRE after retraction modeling of the 12 subsurface beads in the ROI was 1.2 ± 0.6 mm with a maximum of 2.6 mm. Volumetrically, the LIBR reconstruction pulled the incision plane in the inferior direction which resulted in the separation of the incision plane. The model-predicted displacement magnitudes were largest in the area surrounding the incision. This is consistent with the expected displacements caused by retraction in this scenario. The phantom mesh, incision plane, control point placements, and deformed mesh after registration are visualized in Figure VII.5.

For future work, several improvements are needed to expand this preliminary post-incision registration method for true intraprocedural use. First, the deformed model state was calculated by optimizing surface fiducials only. Incorporating a skin surface point cloud and a dissection cavity point cloud, in addition to surface fiducial points, would likely improve registration accuracy. More investigation into how to properly accommodate the dissection cavity point cloud into a registration method is needed. Similarly, in the model

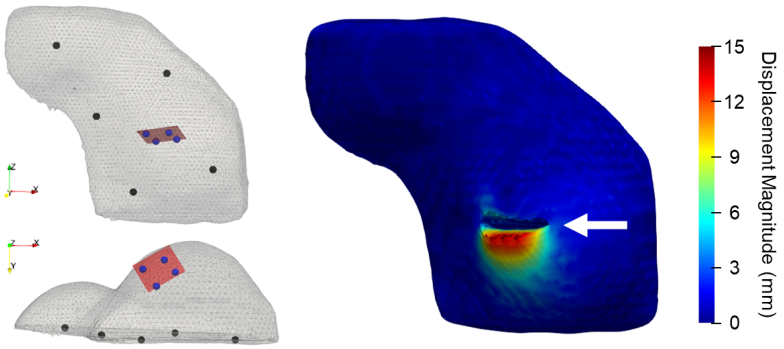

Figure VII.5: (Left) The undeformed breast phantom mesh (gray), posterior control point placement (black), incision control point placement (blue), and incision plane (red) for retraction modeling. (Right) Deformed mesh after modeling retraction showing displacement magnitude. Arrow indicates the incision area of interest. Image reprinted from [10] with permission.

mesh, the dissection cavity was represented as an incision plane. This representation is not entirely realistic, and the dissection cavity should be represented with a more complex geometry.

Additionally, the preliminary approach is not ideal for near real-time intraprocedural updates. This is because it requires additional computation time after incision to calculate the additional FEM displacement modes. Also, it requires a mesh cutting strategy to duplicate elements with virtual nodes at the incision boundary. Both requirements make this strategy cumbersome for near real-time implementation. Rapid methods for accommodating dissection should be explored in future work. One possible solution may be to implement a regularized Kelvinlet displacement basis, which does not require additional computation. Unlike FEM modeling, it does not require a mesh to compute a displacement solution. Instead, a different approach could be used to separate the domain at the incision boundary. Two different sets of regularized Kelvinlet control points could be placed on opposing sides of the dissection boundary, and points in the domain could be selectively assigned to these sets of control points. Points in the positive normal direction to the incision would be assigned to one set of control points, points in the negative normal direction would be assigned to another set of control points, and points below the incision would be assigned to both. This assignment strategy may allow for independent deformations at the incision boundary and model the geometry as if there were a discontinuity in the domain. More investigation is needed to evaluate the feasibility of this approach and other alternative approaches for intraprocedural nonrigid registration model updates after incision.

VII.2.3 Cavity Shaving Guidance

The directions for future exploration thus far have focused on tumor localization for either planning prior to incision or intraprocedural guidance during resection. Another area of interest and potential application is using the system after resection to guide cavity shaving. In BCS after the first pass excision, intraoperative

margin assessment methods are used to evaluate if an additional specimen resection, also known as cavity shaving, is needed. These methods include X-ray or micro-CT imaging to visualize the tumor and intraoperative frozen section histology to evaluate margin status. These methods are rapid assessments that take less than 30 minutes such that they can be performed intraoperatively while the patient is still under anesthesia. Intraoperative margin assessment is performed separately from postoperative margin assessment with hematoxylin and eosin (H&E) histology, which is the gold standard for margin evaluation and requires several days to receive results after surgery. If intraoperative margin assessment shows involved margins, the surgeon will perform a cavity shaving and excise a second specimen. Identifying the excision area in the cavity is challenging and is identified with anatomical directions (i.e., excise an additional inferior-posterior specimen). A future application of this guidance system may be to better inform cavity shaving areas of interest beyond anatomical directions.

The concept of using the guidance system to better inform cavity shaving localization is explored with a proof-of-concept registration experiment. In theory, a 3D specimen model could be acquired by scanning the specimen after excision with a stereo camera or by using 3D micro-CT data acquired during intraoperative margin assessment. A stereo camera 3D point cloud of an excised specimen is shown in Figure VII.6A. For this experiment, a 3D mesh model of a mock excised tumor specimen was created. Then, deformations were applied to the 3D specimen model and a 3D model of a breast mesh after resection to simulate the challenging intraoperative environment. Isotropic shrinkage was applied to the 3D specimen model to simulate specimen dehydration after excision. Deformation caused by gravity was applied to the breast mesh to simulate cavity collapse. Next, data to use for registration from the 3D specimen model and from the excision cavity was created. This data included a sparse point cloud of the collapsed cavity that could be acquired with a tracked stylus, and 6 corresponding points on the 3D specimen model and the cavity representing the anatomical directions. Finally, LIBR reconstruction was used to register the deformed 3D specimen model back to the deformed breast cavity. Note that this is different from previous applications of LIBR where the breast model is deformed. In this application, deformation is applied to the excised specimen model. The registration inputs and results from this experiment are visualized in Figure VII.6B.

The utility of registering a 3D specimen model back to the resection cavity is that it may aid in identifying the region of the cavity wall for re-excision. After intraoperative margin assessment, the positive margin area can be indicated on the 3D specimen model. After registration, this positive margin area can be directly mapped onto the cavity wall. This may help orient surgeons and aid in excising a second specimen that removes remaining tumor tissue. Additionally, if surgeons have more certainty and confidence in localizing the re-excision area, they may be able to excise a smaller second specimen and improve cosmesis. This proof-of-concept registration experiment demonstrates cavity shaving guidance for a simulated specimen and

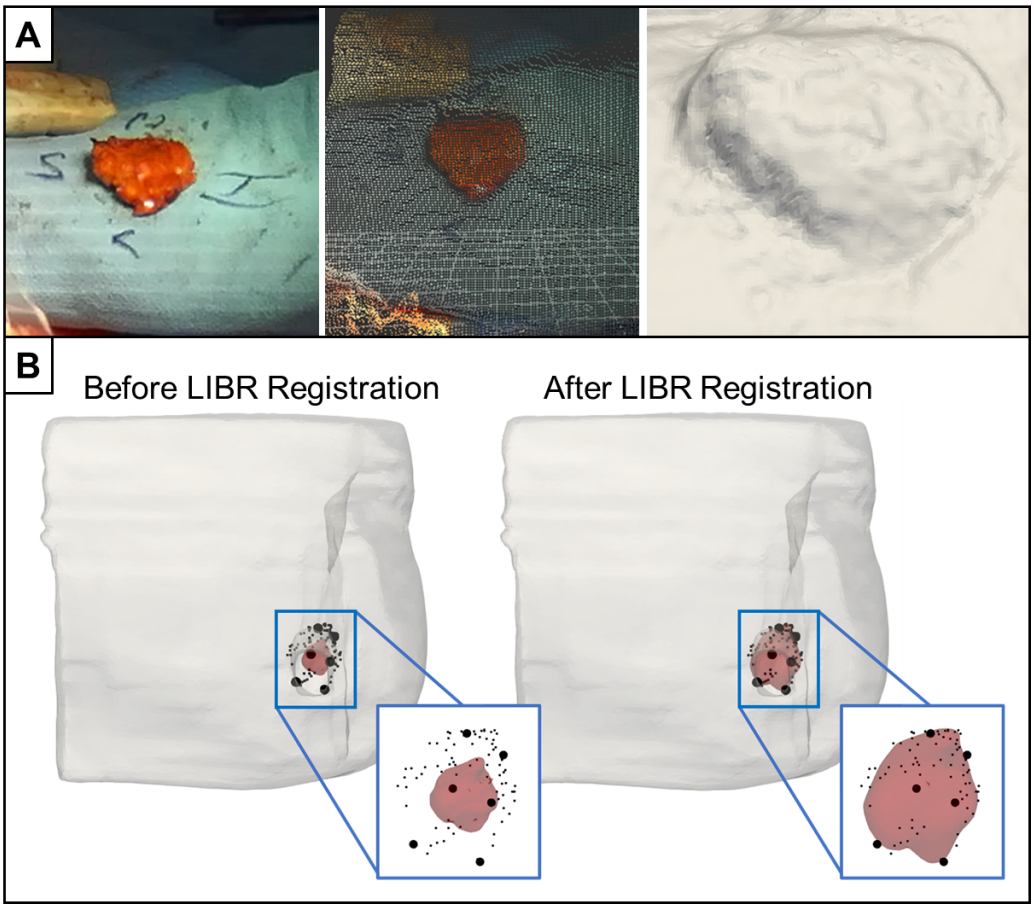

Figure VII.6: Proposed cavity shaving registration for guidance. (A) A stereo camera image (left), point cloud (middle), and 3D model (right) of an excised BCS specimen acquired during surgery. (B) LIBR registration of a simulated specimen aligned to a breast resection cavity showing the breast mesh (gray), sparse data inputs (black), and tumor specimen (red). Specimen-to-cavity alignment is shown before (left) and after (right) registration.

cavity. In future work, this registration should be tested using intraoperative data to assess the feasibility of this method. More investigation is needed to evaluate the practicality and clinical value of using the guidance system to help with cavity shaving localization. This application could be a research direction for future work in BCS image guidance.

VII.3 Regularized Kelvinlet Applications

Chapter V introduced regularized Kelvinlet functions, which are closed-form, analytical solutions to the Navier Cauchy equations for linear elasticity in an infinite medium for a concentrated point load. These functions were used as the deformation basis for an image-to-physical registration method for the BCS image guidance system. This section details other regularized Kelvinlet variations derived from Green's function solutions that may be of interest for medical imaging or biomechanical modeling applications. It also discusses

using regularized Kelvinlets for registration in other organ systems besides breast and for image volume warping.

VII.3.1 Regularized Kelvinlet Variations

Anisotropy with Regularized Kelvinlets

One limitation of using regularized Kelvinlets for modeling biological tissue is that the medium is assumed to be isotropic. Follow-up work by Chen et al. in 2022 derived general Green's function solutions, which can be applied to any regularization scheme, not just the smoothed body load used in the first regularized Kelvinlets paper [240; 19]. This general form is also compatible with any linear elastic material defined by its fourth-rank elasticity tensor $\mathbf{C}$, not just an isotropic linear elastic material defined by its two material property parameters E and ν. This loss of simplicity prevents derivation of closed-form solutions like in the original regularized Kelvinlets paper, but spherical harmonic decomposition is used to rapidly compute displacements for these sculpting brushes with anisotropic materials in practice. The results are elasticity solutions compatible with directionally variable materials.

For breast biomechanical modeling, computationally fast elasticity solutions for anisotropic materials may be especially useful. As explored in Chapter IV, breast tissue exhibits heterogeneous and anisotropic material properties that, when incorporated, improved modeling accuracy. This tissue characterization was abandoned in favor of a simpler and computationally faster modeling method in Chapter V with regularized Kelvinlets for the image guided surgery system. Future work could explore possible modeling improvements by implementing a regularized Kelvinlet function with a transverse isotropic material. This may help expand the use cases of regularized Kelvinlet functions to applications where preserving tissue anisotropy is required.

Regularized Half-Space Solutions

Another limitation of regularized Kelvinlets is the fact that they represent displacements in an infinite medium and do not account for discrete domains. Conventionally, incorporating geometry requires domain discretization. However, other closed-form solutions (aside from the Kelvinlet solution) may present opportunities to include geometric boundaries. In addition to closed-form solutions to point forces in an infinite solid, closed-form solutions to point forces applied to an infinite half-space in the normal and tangential forcing directions exist in elastostatics literature, and these solutions are sometimes referred to as the Boussinesq–Cerruti solutions [153]. Like the Kelvinlet solution, these solutions are singular at the forcing location. However, it may be possible to derive half-space solutions with a regularized, smoothed forcing load analogous to the regularized Kelvinlet. These regularized half-space solutions may offer a more accurate representation of elasticity at discrete organ boundaries, even though it still would not incorporate the full organ geometry.

More investigation into deriving and testing regularized half-space solutions is needed, but they may offer an improved method for analytically modeling elasticity at domain boundaries.

VII.3.2 Additional Organ Systems

In this work, regularized Kelvinlet functions were proposed in the context of registration for BCS image guidance. However, the methodology outlined in Chapter V is generally organ agnostic and can be adapted for image guidance or registration applications in other soft tissue organ systems. Outside of breast, regularized Kelvinlets were employed for registration in liver. The optimal control point and relaxation radius parameters used in liver were different than those used in breast. The sensitivity to these parameters and the liver registration results are described in detail in Appendix A. To date, regularized Kelvinlet functions were also submitted as a method to the Sparse Data Challenge, which compares sparse data registration method performance on a common dataset. Results are reported in published work [241; 242].

To adapt regularized Kelvinlets for registration in other organ systems, several factors should be considered. The first of these factors is how regularized Kelvinlet control points are distributed on the organ geometry. For breast registration, this distribution was informed by the chest wall geometry and loading conditions. In other organ systems, control points should be deployed based on the likely deformations and expected forces for that organ. The organ system environment, such as interstitial pressure changes that occur during neurosurgery procedures or pressure changes from insufflation during minimally invasive procedures, should be considered in this context. Another factor is the relaxation radius parameter ε. This parameter controls the radius of the smoothing function extent, and it generally should correlate with the organ geometry size. With other organ systems, this parameter may need to be adjusted to achieve realistic registration results. For example, one might hypothesize that the ε parameter should be reduced for kidney registration compared to the optimal ε for breast, given that the average breast has a larger extent and volume than the average kidney. The ε factor should be verified for each application when applying regularized Kelvinlets for registration of other organs. Finally, grab and twist regularized Kelvinlet functions were utilized for breast registration. Again, this configuration could be altered depending on the organ of interest. Regularized Kelvinlet registration may be of interest in several organs where registration for image guidance or soft tissue biomechanical modeling is an active research area. Organ systems where regularized Kelvinlet registration may be applicable include brain, prostate, kidney, lung, pancreas, and others. Future work should focus on expanding these methods to apply to a broader set of registration problems and evaluating organ specific deployments on a case-by-case basis.

VII.3.3 Image Volume Warping

For the image guided surgery application in this work, warped image volumes after registration were presented as masked volumes. The transformation was applied only to the volume area contained in the 3D mesh. This masked volume presentation may be distracting for surgeons accustomed to viewing full 3D volumes with surrounding anatomy. Regularized Kelvinlet functions could be used to extrapolate the organ transformation to the dense, full 3D volume instead of only the masked region. The full transformation can be easily computed because regularized Kelvinlet functions are embedded in an infinite domain. In contrast, an FEM-computed registration solves for displacements inside of the mesh only. Extrapolating to the full image volume would require an interpolative decay function outside of the masked area.

A warped image volume example that utilizes regularized Kelvinlets to transform the image region outside of the breast is shown in Figure VII.7. More investigation is needed to determine user preference between masked, partially deformed image volumes and unmasked, fully deformed image volumes. Although the unmasked image volumes include additional anatomical structures (in the case of supine breast imaging, the pectoral muscles and ribs are visible), the imparted deformations on these structures may be unrealistic. Presenting registration results in this way, instead of with masked volumes, may be an area of future interest for image guidance applications.

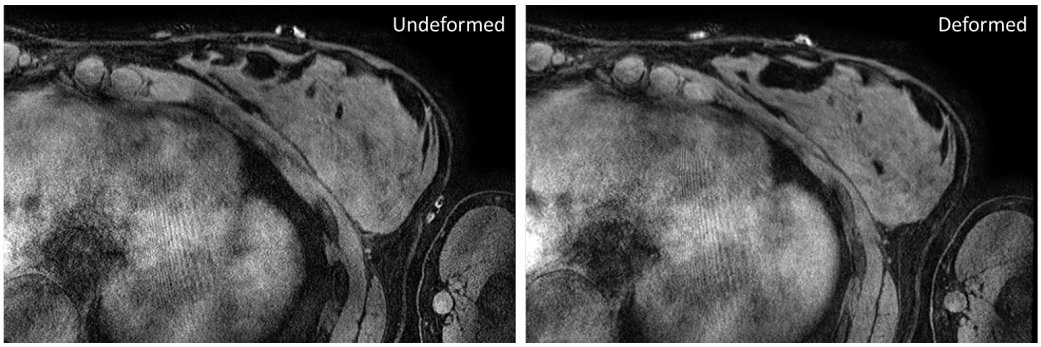

Figure VII.7: Undeformed image volume (left) compared to a deformed image volume (right) where the regularized Kelvinlet deformation field was applied to voxels outside of the breast mesh.

VII.4 Closing Remarks

This dissertation details advancements towards an image guidance system for BCS. State of the art methods in breast biomechanical tissue modeling (Chapter IV), rapid sparse data registration (Chapter V), and system development (Chapter VI) are employed. By presenting this work, the intention is to improve patient outcomes and further the integration of advanced technology in BCS procedures, while simultaneously inspiring novel research avenues in the image guided surgery field.

APPENDIX A

Regularized Kelvinlet functions for liver deformation modeling

A.1 Introduction

The methods in Chapter V are presented in the context of breast deformation modeling for integration into a BCS guidance system. However, these methods can be easily adapted for registration problems in other soft tissue organ systems. Hepatic surgeries also suffer from large soft tissue deformations caused by insufflation and organ manipulation. Without nonrigid registration, these deformations confound the use of image guidance systems. This section details the adaptation of the image-to-physical registration method with regularized Kelvinlet functions to register a liver phantom dataset. It also compares registration using regularized Kelvinlet functions to registration performance using the finite element method (FEM) to create the deformation basis. This section is adapted from, "Comparing Regularized Kelvinlet Functions and the Finite Element Method for Registration of Medical Images to Sparse Organ Data," which is released on arXiv and currently in review at Medical Image Analysis [214]. This method was also submitted as an entry in the Image-to-Physical Liver Registration Sparse Data Challenge, which compares state of the art registration methods on a common dataset [242].

A.2 Methods

The sparse data registration method features two phases: a precomputation phase where a basis of displacement solutions is generated on a specific liver model geometry, and a reconstruction phase where the displacement basis is used to deform the liver model to match sparse data inputs. First, the regularized Kelvinlets displacement solutions detailed in de Goes et al. are proposed for generating a realistic biomechanical displacement basis in the precomputation phase [19]. To assess fidelity, the regularized Kelvinlets displacement basis is compared to a displacement basis generated using a more conventional FEM model from previous work in Heiselman et al. [20]. Finally, the algorithm for the reconstruction phase from [20] is used for both biomechanical model displacement bases realizations for direct comparison. Equation notation is written such that constants are italicized, vectors are bolded, and matrices are double-struck letters.

A.2.1 Regularized Kelvinlets Displacement Solution

The same methodology outlined in Section V.4.1 for regularized Kelvinlet registration in the breast is used in the liver. Solving for the analytical solution to the equations for linear elasticity with a smoothed forcing function yields the formula for regularized Kelvinlets proposed in [19] and reproduced as follows:

$$\mathbf{u}_\varepsilon(\boldsymbol{r}) = \left[\frac{a-b}{r_\varepsilon}\mathbb{I} + \frac{b}{r_\varepsilon^3}\boldsymbol{r}\boldsymbol{r}^t + \frac{a}{2}\frac{\varepsilon^2}{r_\varepsilon^3}\mathbb{I}\right]\boldsymbol{f} \tag{A.1}$$

The solution in Equation A.1 assumes an infinite elastic medium, and it does not account for the geometry of the domain. In Equation A.1, $r_\varepsilon = \sqrt{r^2+\varepsilon^2}$ is the regularized distance, ε is the regularization radial scale, and a and b are material parameter coefficients equal to $a = \frac{(1+\nu)}{2\pi E}$ and $b = \frac{a}{4(1-\nu)}$. $\mathbb{I}$ is the identity matrix.

The $\boldsymbol{r}$ vectors and corresponding $\mathbf{u}_\varepsilon(\boldsymbol{r})$ vectors from a regularized Kelvinlet displacement solution can be computed for every individual node in a liver mesh. The $\mathbf{u}_\varepsilon(\boldsymbol{r})$ vectors can be concatenated to form a displacement vector:

$$\boldsymbol{d}_{RK} = \begin{bmatrix} \mathbf{u}_\varepsilon(\boldsymbol{r}_1) \\ \mathbf{u}_\varepsilon(\boldsymbol{r}_2) \\ \cdots \\ \mathbf{u}_\varepsilon(\boldsymbol{r}_M) \end{bmatrix} \tag{A.2}$$

where vector $\boldsymbol{d}_{RK}$ is length $3M$ and M is the number of nodes in the mesh.

A.2.2 Finite Element Method Displacement Solution

The regularized Kelvinlet displacements are compared to displacement solutions derived from a conventional elastic FEM model. For FEM model realization, liver volumes are discretized with tetrahedral meshes with 4 mm element edge lengths. The Galerkin weighted residual method with linear Lagrange basis functions is applied to integrate the partial differential equations associated with the Navier Cauchy equations. This process produces a coupled set of differential equations as:

$$\mathbf{u}_{FEM} = \mathbb{K}^{-1}\mathbf{F} \tag{A.3}$$

where $\mathbb{K}$ is the global stiffness matrix, $\mathbf{u}_{FEM}$ is the vector of displacements, and $\mathbf{F}$ is the vector containing forcing terms and boundary conditions.

To create a non-singular FEM displacement solution response to a distributed point load, the methodology described in [20] perturbs and relaxes a singular boundary mesh point, rendering a comparable solution to regularized Kelvinlets. For this displacement solution, a series of control points are distributed evenly on the control surface of the organ. The control point at the load location $\boldsymbol{x}_0$ is perturbed while all other control points are fixed. After perturbation, the Voronoi tile region surrounding the point load location is relaxed, and a distributed load that results in identical far-field displacements is computed in accordance with the Saint-Venant principle. The resulting displacement vector after relaxation is denoted as $\boldsymbol{d}_{FEM}$ which is of length

$3M$ where M is the number of nodes in the mesh.

The displacement and strain norm fields from the relaxed FEM displacement solution and the regularized Kelvinlets displacement solution at one point load location on the liver are shown in Figure A.1. Two values of the radial scale parameter ε are shown for the regularized Kelvinlets displacement solutions. Both the relaxed FEM and regularized Kelvinlets displacement solutions are approximations of deformation responses to point load forces. As shown in Figure A.1, both solutions exhibit a local response centered on the point at which the perturbation is applied. However, the relaxed FEM displacement solution accounts for organ geometry, and it is also influenced by the mesh resolution and all other control point locations that are fixed during perturbation. The regularized Kelvinlet solution is computed as if the organ is embedded in an infinite elastic medium, and it does not account for organ specific geometry.

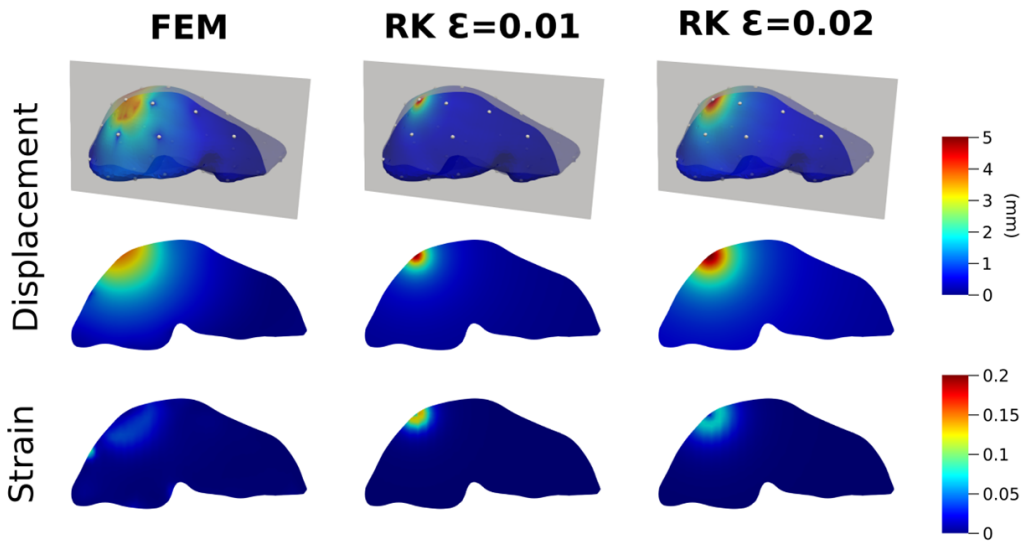

Figure A.1: Comparison of displacement and strain norm fields generated from perturbation of a singular control point using the FEM method and the Regularized Kelvinlets (RK) method with two radial scale ε values on liver geometry. Each field is normalized to have a maximum displacement value of 5 mm.

A.2.3 Sparse Data Registration

From the sections above, two linear elastic modeling methods have been presented for representing the displacements caused by a distributed point load force. The linearized iterative boundary reconstruction (LIBR) method, detailed in [20], uses a displacement basis composed of FEM displacement solutions and solves for an optimal linear combination of these solution vectors to minimize model-data error and achieve a sparse-data-driven nonrigid registration. In this work, the method proposed in [20] (referred to as LIBR+FEM) has been re-engineered to employ regularized Kelvinlets displacement solutions as the displacement basis (referred to as LIBR+RK) in lieu of FEM. Both LIBR+FEM and LIBR+RK displacement bases methods

are linearly superposed and combined within an optimization framework to recover an optimal registration displacement state.

To create the LIBR+FEM displacement basis, each control point is perturbed and relaxed in the x, y, and z directions to create a series of $\boldsymbol{d}_{FEM}$ basis vectors. In total, $3k$ basis vectors are generated where k is the number of control points. As detailed in [20], the registered deformation state $\tilde{\mathbf{u}}_{FEM}$ can be approximated as:

$$\tilde{\mathbf{u}}_{FEM} = \mathbb{J}_{u-FEM}\boldsymbol{\alpha}_{FEM} = \begin{bmatrix} | & | & & | \\ \boldsymbol{d}_{FEM-1} & \boldsymbol{d}_{FEM-2} & \dots & \boldsymbol{d}_{FEM-3} \\ | & | & & | \end{bmatrix} \boldsymbol{\alpha}_{FEM} \tag{A.4}$$

where $\tilde{\mathbf{u}}_{FEM}$ approximates the deformation state based on the linear combination of the displacement basis functions written as the displacement response matrix $\mathbb{J}_{u-FEM}$ (size $3M$ x $3k$), and $\boldsymbol{\alpha}_{FEM}$ is the displacement basis function weights of length $3k$. Along with displacement, a $6M$ x $3k$ stress response matrix $\mathbb{J}_{stress-FEM}$ and $6M$ x $3k$ strain response matrix $\mathbb{J}_{strain-FEM}$ are formulated at mesh elements and interpolated onto nodes using the conventional linear elasticity stress-strain and strain-displacement relationships. These response matrices allow for a linearized representation of the stress and strain values for any given displacement basis function weights $\boldsymbol{\alpha}_{FEM}$.

To create an analogous LIBR+RK displacement basis, the unit forcing vectors are used in Equation A.1 to formulate a set of $\boldsymbol{d}_{RK}$ basis vectors that represent the displacement response to the unit forcing vectors at every k control point. The $\tilde{\mathbf{u}}_{RK}$ approximate deformation state can be written as:

$$\tilde{\mathbf{u}}_{RK} = \mathbb{J}_{u-RK}\boldsymbol{\alpha}_{RK} = \begin{bmatrix} | & | & & | \\ \boldsymbol{d}_{RK-1} & \boldsymbol{d}_{RK-2} & \dots & \boldsymbol{d}_{RK-3} \\ | & | & & | \end{bmatrix} \boldsymbol{\alpha}_{RK} \tag{A.5}$$

where $\mathbb{J}_{u-RK}$, $\mathbb{J}_{stress-RK}$, and $\mathbb{J}_{strain-RK}$ are the displacement, stress, and strain response matrices and $\boldsymbol{\alpha}_{RK}$ is the weight vector.

The registration task is to solve for the optimal $\boldsymbol{\alpha}_{FEM}$ or $\boldsymbol{\alpha}_{RK}$ vector, combined with rigid transformation parameters $\boldsymbol{\tau}$ (translation) and $\boldsymbol{\theta}$ (rotation), that minimizes model-data error and the strain energy of the deformation. The approach proposed in [20] for formulating the objective function, establishing correspondences for calculating model-data error, incorporating a rigid transformation, and calculating the strain energy term is kept identical for the LIBR+FEM and LIBR+RK methods. This algorithmic consistency allows for a direct comparison of the two biomechanical models without the influence of other variables. The objective function as described in [20] is as follows:

$$\Omega(\boldsymbol{\beta}) = \sum_{F} \frac{w_F}{N_F} \sum_{i=1}^{N_F} f_i^2 + w_E f_E^2 \tag{A.6}$$

where $\boldsymbol{\beta} = [\boldsymbol{\alpha}_{FEM}, \boldsymbol{\tau}, \boldsymbol{\theta}]$ or $\boldsymbol{\beta} = [\boldsymbol{\alpha}_{RK}, \boldsymbol{\tau}, \boldsymbol{\theta}]$ depending on the chosen basis functions. Two competing squared error terms, f_i^2 and f_E^2, are included in the objective function. The first error term, , f_i^2, corresponds to the model-data error which controls the organ deformation. f_i is the model-data displacement error at datapoint i, w_F is the weight of data feature F, and N_F is the total number of data points in feature F. The data features are chosen to mimic data that could theoretically be acquired in a surgical environment for intraoperative registration and are discussed in more detail for liver registration in the next section. The second error term, f_E^2, is a regularization term that prevents large strain-energy deformations. f_E is the average strain energy density across the mesh, computed as the sum of the nodal strain energy densities normalized by the number of mesh nodes M, and w_E is the strain energy regularization weight. f_E is computed with either equation below depending on the method (LIBR+FEM or LIBR+RK).

$$f_E = \frac{1}{2M} \boldsymbol{\alpha}_{FEM}^T (\mathbb{J}_{strain-FEM}^T \mathbb{J}_{stress-FEM}) \boldsymbol{\alpha}_{FEM} \tag{A.7}$$

$$f_E = \frac{1}{2M} \boldsymbol{\alpha}_{RK}^T (\mathbb{J}_{strain-RK}^T \mathbb{J}_{stress-RK}) \boldsymbol{\alpha}_{RK} \tag{A.8}$$

Levenberg-Marquardt optimization is used to iteratively solve for $\boldsymbol{\beta}$ by minimizing the objective function with a termination criterion of $|\Delta\Omega(\boldsymbol{\beta})| < 10^{-12}$.

A.2.4 Phantom Liver Dataset

The phantom liver dataset was obtained from the Sparse Data Challenge for image-guided liver surgery [243; 217]. The challenge dataset includes a liver geometry mesh, 112 sparse data feature configurations, and 159 targets. The sparse data feature configurations were generated from contact and non-contact intraoperative data collections. The liver phantom was composed of a silicone material cast from a mold that was obtained from a human patient CT image volume and emulated the stiffness of liver tissue. Deformations were applied to the phantom's posterior surface. Parameter values of $E = 2100$ Pa, $\nu = 0.45$, and $w_E = 10^{-8}$ Pa^{-2} were used for both the LIBR+FEM and LIBR+RK methods based on parameter values used in previous work [20].

A.2.5 Experimental Setup

Registrations using the LIBR+FEM and LIBR+RK methods were performed on the liver dataset. 3D point locations on the organ mesh surfaces were designated as control points. Two control point distribution strategies were tested - placing control points distributed evenly just on the posterior surface of the organ and

placing control points distributed evenly everywhere on the organ surface. K-means clustering was used to distribute control points evenly on the organ's surface, which partitioned the organ's control surface into Voronoi cells. This control point distribution created deformations that evenly perturbed different regions of the organ surface. A parameter sweep of the number of control points k was performed iterating between 10-190 in increments of 30. For the LIBR+RK method, a parameter sweep of the radial scale parameter ε was performed iterating through the values $\varepsilon = [0.001, 0.002, 0.005, 0.01, 0.02, 0.05, 0.1, 0.2, 0.5]$ meters. Registration performance was evaluated by calculating the root mean squared (RMS) target registration error (TRE), which is the root mean squared error of all individual target errors in one registration case. The precomputation phase for the LIBR+FEM method was parallelized on 8 threads of an AMD Ryzen 7 3700X CPU. All other computations (LIBR+FEM reconstruction and LIBR+RK precomputation and reconstruction) were performed on a single thread of an AMD Ryzen 7 3700X CPU.

A.3 Results

A.3.1 Parameter Sweep Results

The registration accuracy results from the parameter sweep are shown in Figure A.2. Each square denotes the average RMS TRE for a parameter sweep combination averaged across the 112 data configurations for the liver dataset. Average RMS TRE is displayed as a function of registration method (LIBR+FEM or LIBR+RK), control point placement strategy (either distributed on the organ's posterior surface or on the entire organ surface), radial scale ε for LIBR+RK registrations (x-axis), and number of control points (y-axis).

The optimal number of control points and radial scale ε parameters for each method, control point placement, and dataset are reported in Table A.1. The overall optimal registration for the liver dataset was with the LIBR+FEM method with $k = 40$ control points distributed on the posterior surface, resulting in an average RMS TRE of 3.2 ± 0.8 mm. The best registration accuracy for the liver dataset with the LIBR+RK method was 4.6 ± 1.0 mm which occurred with $k = 160$ control points distributed everywhere with $\varepsilon = 0.01$.

Examining the parameter sweep overall, many of the parameter combinations resulted in average RMS TRE values that were within a 1 mm range of the optimal RMS TRE values. These parameter combinations are indicated in Figure A.2 by the inner black borders. For the number of control points, the optimal parameter combination for the LIBR+RK implementation had a higher number of control points than the LIBR+FEM implementation. For the radial scale parameter ε, the extremes of the parameter sweep resulted in worse average RMS TRE showing the importance of selecting an ε parameter appropriate for the scale of the geometric organ. The average registration accuracy for the LIBR+RK method fell within the 4-7 mm range for most parameter combinations, while the accuracy using the LIBR+FEM method fell in the 3-4 mm range.

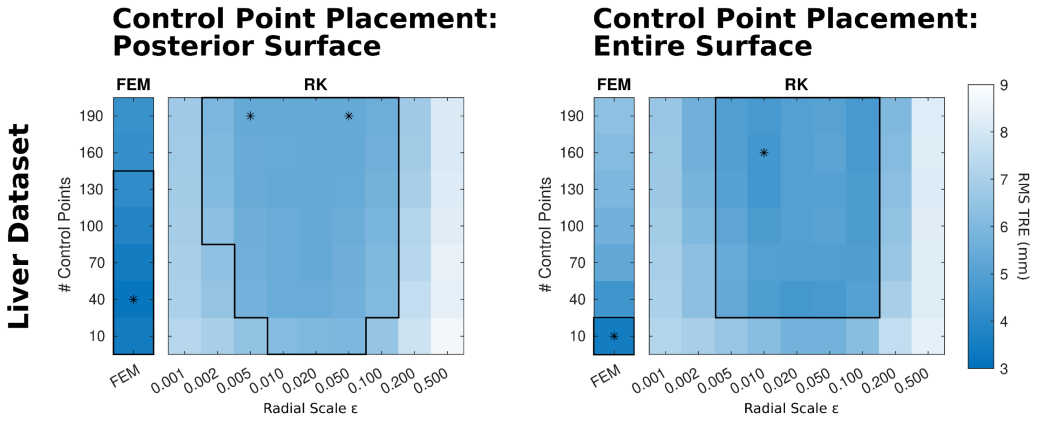

Figure A.2: Parameter sweep results for the liver dataset. Control points were distributed on the posterior (left) and entire (right) surface of the organ. Average RMS TRE values are plotted as a function of the number of control points and radial scale parameter ε. Optimal average RMS TRE values are denoted by asterisks, and numerical values are reported in Table A.1. The black border denotes areas where RMS TRE values are within 1 mm of the minimum.

Table A.1: Optimal average RMS TRE values resulting from the parameter sweep.

Control Point Placement	**Method**	**Optimal Average RMS TRE $\pm$ std (mm)**	**# Control Points**	**Radial Scale ε**
Posterior surface	FEM	3.2 ± 0.8	40	-
	RK	5.4 ± 1.1	190	0.005, 0.05
Entire surface	FEM	3.5 ± 0.9	10	-
	RK	4.6 ± 1.0	160	0.01

A.3.2 Registration Accuracy

The optimal parameters for the LIBR+FEM and LIBR+RK registration methods were then used to compare organ deformations and individual target errors for example cases. The following optimal registrations were examined: 1) $k = 40$, posterior surface distribution for LIBR+FEM method on the liver dataset and 2) $k = 160, \varepsilon = 0.01$, entire surface distribution for the LIBR+RK method on the liver dataset. Individual target ground-truth locations for 35 targets in 4 out of the 112 deformations (deformations 44, 57, 67, and 84 denoted as L1-L4) are provided as a part of the Sparse Data Challenge for visualization, calculation, and examination of individual target errors. The global organ deformations for the LIBR+FEM (green) and the LIBR+RK (purple) methods are shown on the liver geometries in Figure A.3. The registered deformation states using both methods appear qualitatively similar. In addition to using RMS TRE as a metric for evaluating registration performance, comparing the organ mesh shape after registration confirms that both methods are producing similar global deformations.

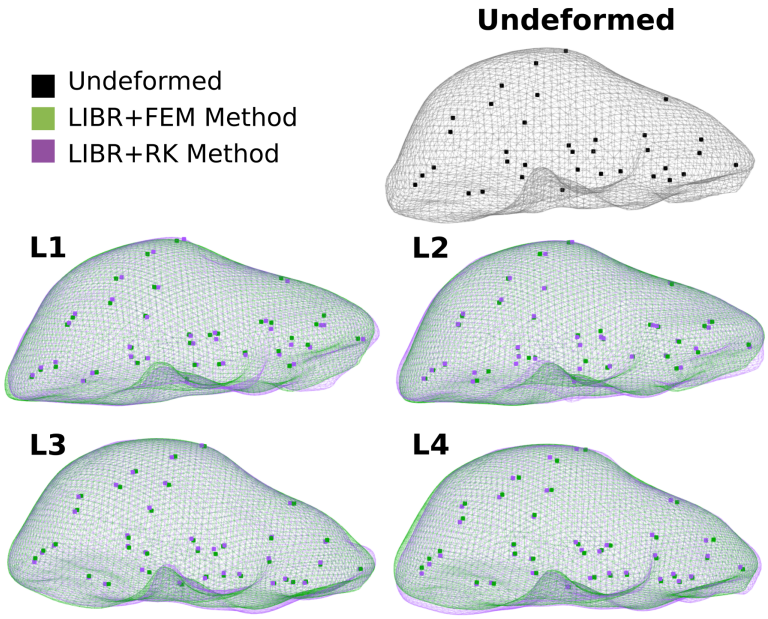

Figure A.3: Registered organs and targets from 4 example liver registrations (L1-L4). The undeformed geometry (black) is compared to the deformed geometry using the LIBR+FEM method (green) and the LIBR+RK method (purple).

A.3.3 Image Deformation

For image-guided surgery, deforming a volumetric image may be useful for visualizing the deformed anatomy. As noted above, the Sparse Data Challenge liver phantom geometry was derived from a patient's liver CT image volume. Despite deformations being based on a silicone phantom counterpart, the original liver image volume can be deformed using the deformation fields from our applied registration methods as a means to compare image similarity among all imaging volumes (original and deformed). This process is shown in Figure A.4 for the 4 example liver data configurations for the LIBR+FEM method (green), the LIBR+RK method (purple), and the undeformed original organ for reference (yellow). Vasculature features within the liver segmentations for the deformed images look qualitatively similar when comparing the resulting deformed images from the two registration methods.

A.4 Conclusion

In this work, regularized Kelvinlet functions are used for reconstructing deformation states on an elastic tissue-mimicking liver phantom dataset. This method is evaluated against a more traditional FEM registration method as a comparator. The accuracy of both registration methods is generally comparable, with the average optimal RMS TRE values ranging between 3-7 mm for both methods shown in Figure A.2. The

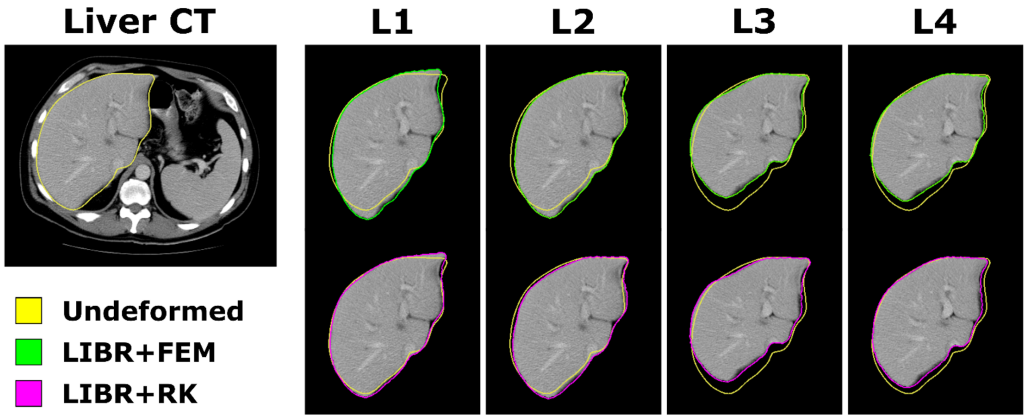

Figure A.4: Image deformation results from the phantom liver dataset. An axial slice of the undeformed segmented liver (yellow) shows the original anatomy. The LIBR+FEM and LIBR+RK methods are used to deform the volume and segmentation contours (green and purple) for 4 example data configurations (L1-L4).

optimal RMS TRE values were lower when using the LIBR+FEM method with 40 control points distributed on the organ's posterior surface than when using the LIBR+RK method with 160 control points and $\varepsilon = 0.01$ distributed on the entire organ's surface. The Sparse Data Challenge liver dataset was designed as a controlled experiment with well-defined materials and loading conditions. The phantom was composed of a linear elastic silicone material, and deformations were caused by adding and removing padding under the posterior surface of the liver phantom. The LIBR+FEM method models the unique geometry of the liver phantom. Placing control points on the posterior surface with the LIBR+FEM method designates the anterior surface of the organ as stress free and accurately represents the experimental conditions. The LIBR+RK method models deformations in an infinite elastic domain and cannot represent the experimental conditions as accurately as the LIBR+FEM method, which may be a cause of the degradation in TRE results. Overall, the application of this method on the liver dataset demonstrates its utility on another organ system outside of breast registration. Overall, using regularized Kelvinlet functions for sparse data registration is a promising method for performing nonrigid, near real-time correction in image-guided surgery applications.

BIBLIOGRAPHY

[1] E. García, Y. Diez, O. Diaz, X. Lladó, R. Martí, J. Martí, and A. Oliver, "A step-by-step review on patient-specific biomechanical finite element models for breast mri to x-ray mammography registration," *Medical Physics*, vol. 45, Dec. 2017.

[2] "Breast cancer facts and figures 2022-2024," *American Cancer Society*, 2022.

[3] "About breast magnetic resonance imaging (https://www.mskcc.org/cancer-care/patient-education/breast-magnetic-resonance-imaging-mri-breast)," *Memorial Sloan Kettering Cancer Center*, 2024.

[4] "Performing an mr scan (https://mriquestions.com/what-are-the-steps.html)," *Courtesy of Allen D. Elster, MRIquestions.com*, 2024.

[5] E. C. Gombos, J. Jayender, D. M. Richman, D. L. Caragacianu, M. A. Mallory, F. A. Jolesz, and M. Golshan, "Intraoperative supine breast mr imaging to quantify tumor deformation and detection of residual breast cancer: Preliminary results," *Radiology*, vol. 281, p. 720–729, Dec. 2016.

[6] S. B. Mondal, S. Gao, N. Zhu, R. Liang, V. Gruev, and S. Achilefu, *Real-Time Fluorescence Image-Guided Oncologic Surgery*, p. 171–211. Elsevier, 2014.

[7] J. M. Chakedis, A. Tang, G. E. Kuehner, B. Vuong, L. L. Lyon, L. A. Romero, B. M. Raber, M. M. Mortenson, V. C. Shim, N. M. Datrice-Hill, J. R. McEvoy, V. A. Arasu, D. J. Wisner, and S. B. Chang, "Implementation of intraoperative ultrasound localization for breast-conserving surgery in a large, integrated health care system is feasible and effective," *Annals of Surgical Oncology*, vol. 28, p. 5648–5656, Aug. 2021.

[8] R. J. Barth, V. Krishnaswamy, K. D. Paulsen, T. B. Rooney, W. A. Wells, C. V. Angeles, R. A. Zuurbier, K. Rosenkranz, S. Poplack, and T. D. Tosteson, "A randomized prospective trial of supine mri-guided versus wire-localized lumpectomy for breast cancer," *Annals of Surgical Oncology*, vol. 26, p. 3099–3108, July 2019.

[9] K. M. Gaskin, G. E. Peoples, and D. E. McGhee, "The fibro-adipose structure of the female breast: A dissection study," *Clinical Anatomy*, vol. 33, p. 146–155, Nov. 2019.

[10] A. Espinosa, M. J. Ringel, J. S. Heiselman, K. Pereira, F. Servin, W. L. Richey, I. Meszoely, and M. I. Miga, "Modeling retraction for breast conserving surgery guidance," in *Medical Imaging 2023: Image-Guided Procedures, Robotic Interventions, and Modeling* (C. A. Linte and J. H. Siewerdsen, eds.), vol. 12466, p. 1246628, International Society for Optics and Photonics, SPIE, 2023.

[11] K. Kaczmarski, P. Wang, R. Gilmore, H. N. Overton, D. M. Euhus, L. K. Jacobs, M. Habibi, M. Camp, M. J. Weiss, and M. A. Makary, "Surgeon re-excision rates after breast-conserving surgery: A measure of low-value care," *Journal of the American College of Surgeons*, vol. 228, pp. 504–512e2, Apr. 2019.

[12] D. R. Leff, E. R. St John, and Z. Takats, "Reducing the margins of error during breast-conserving surgery: Disruptive technologies or traditional disruptions?," *JAMA Surgery*, vol. 152, p. 517, June 2017.

[13] M. A. Mallory, Y. Sagara, F. Aydogan, S. DeSantis, J. Jayender, D. Caragacianu, E. Gombos, K. G. Vosburgh, F. A. Jolesz, and M. Golshan, "Feasibility of intraoperative breast mri and the role of prone versus supine positioning in surgical planning for breast-conserving surgery," *The Breast Journal*, vol. 23, p. 713–717, Mar. 2017.

[14] F. Alam, S. U. Rahman, S. Ullah, and K. Gulati, "Medical image registration in image guided surgery: Issues, challenges and research opportunities," *Biocybernetics and Biomedical Engineering*, vol. 38, no. 1, p. 71–89, 2018.

[15] R. M. Mann, N. Cho, and L. Moy, "Breast mri: State of the art," *Radiology*, vol. 292, p. 520–536, Sept. 2019.

[16] S. Joukainen, A. Masarwah, M. Könönen, M. Husso, A. Sutela, V. Kärjä, R. Vanninen, and M. Sudah, "Feasibility of mapping breast cancer with supine breast mri in patients scheduled for oncoplastic surgery," *European Radiology*, vol. 29, p. 1435–1443, Aug. 2018.

[17] L. A. Carbonaro, P. Tannaphai, R. M. Trimboli, N. Verardi, M. P. Fedeli, and F. Sardanelli, "Contrast enhanced breast mri: Spatial displacement from prone to supine patient's position. preliminary results," *European Journal of Radiology*, vol. 81, p. e771–e774, June 2012.

[18] W. L. Richey, J. S. Heiselman, M. Luo, I. M. Meszoely, and M. I. Miga, "Impact of deformation on a supine-positioned image-guided breast surgery approach," *International Journal of Computer Assisted Radiology and Surgery*, vol. 16, p. 2055–2066, Aug. 2021.

[19] F. De Goes and D. L. James, "Regularized kelvinlets: Sculpting brushes based on fundamental solutions of elasticity," *ACM Trans. Graph.*, vol. 36, jul 2017.

[20] J. S. Heiselman, W. R. Jarnagin, and M. I. Miga, "Intraoperative correction of liver deformation using sparse surface and vascular features via linearized iterative boundary reconstruction," *IEEE Transactions on Medical Imaging*, vol. 39, p. 2223–2234, June 2020.

[21] S. Agarwal, L. Pappas, L. Neumayer, K. Kokeny, and J. Agarwal, "Effect of breast conservation therapy vs mastectomy on disease-specific survival for early-stage breast cancer," *JAMA Surgery*, vol. 149, p. 267, Mar. 2014.

[22] J. Landercasper, B. Bennie, H. F. Ahmad, and J. H. Linebarger, "Opportunities to reduce reoperations and to improve inter-facility profiling after initial breast-conserving surgery for cancer. a report from the ncdb," *European Journal of Surgical Oncology*, vol. 45, p. 2026–2036, Nov. 2019.

[23] "Cancer facts and figures 2024," *American Cancer Society*, 2024.

[24] L. Rahib, M. R. Wehner, L. M. Matrisian, and K. T. Nead, "Estimated projection of us cancer incidence and death to 2040," *JAMA Network Open*, vol. 4, p. e214708, Apr. 2021.

[25] A. E. Giuliano, S. B. Edge, and G. N. Hortobagyi, "Eighth edition of the ajcc cancer staging manual: Breast cancer," *Annals of Surgical Oncology*, vol. 25, p. 1783–1785, Apr. 2018.

[26] S. Chootipongchaivat, N. T. van Ravesteyn, X. Li, H. Huang, H. Weedon-Fekjær, M. D. Ryser, D. L. Weaver, E. S. Burnside, B. M. Heckman-Stoddard, H. J. de Koning, and S. J. Lee, "Modeling the natural history of ductal carcinoma in situ based on population data," *Breast Cancer Research*, vol. 22, May 2020.

[27] A. D. Corben, "Pathology of invasive breast disease," *Surgical Clinics of North America*, vol. 93, p. 363–392, Apr. 2013.

[28] J. Makki, "Diversity of breast carcinoma: Histological subtypes and clinical relevance," *Clinical Medicine Insights: Pathology*, vol. 8, p. CPath.S31563, Jan. 2015.

[29] M. C. Cheang, M. Martin, T. O. Nielsen, A. Prat, D. Voduc, A. Rodriguez-Lescure, A. Ruiz, S. Chia, L. Shepherd, M. Ruiz-Borrego, L. Calvo, E. Alba, E. Carrasco, R. Caballero, D. Tu, K. I. Pritchard, M. N. Levine, V. H. Bramwell, J. Parker, P. S. Bernard, M. J. Ellis, C. M. Perou, A. Di Leo, and L. A. Carey, "Defining breast cancer intrinsic subtypes by quantitative receptor expression," *The Oncologist*, vol. 20, p. 474–482, Apr. 2015.

[30] A. G. Waks and E. P. Winer, "Breast cancer treatment: A review," *JAMA*, vol. 321, p. 288, Jan. 2019.

[31] M. D. Ryser, D. L. Weaver, F. Zhao, M. Worni, L. J. Grimm, R. Gulati, R. Etzioni, T. Hyslop, S. J. Lee, and E. S. Hwang, "Cancer outcomes in dcis patients without locoregional treatment," *JNCI: Journal of the National Cancer Institute*, vol. 111, p. 952–960, Feb. 2019.

[32] EBCTCG, S. Darby, P. McGale, C. Correa, C. Taylor, R. Arriagada, M. Clarke, D. Cutter, C. Davies, M. Ewertz, J. Godwin, R. Gray, L. Pierce, T. Whelan, Y. Wang, and R. Peto, "Effect of radiotherapy after breast-conserving surgery on 10-year recurrence and 15-year breast cancer death: meta-analysis of individual patient data for 10,801 women in 17 randomised trials," *Lancet*, vol. 378, pp. 1707–1716, Nov. 2011.

[33] K. Chen, J. Liu, L. Zhu, F. Su, E. Song, and L. K. Jacobs, "Comparative effectiveness study of breast-conserving surgery and mastectomy in the general population: A ncdb analysis," *Oncotarget*, vol. 6, p. 40127–40140, Oct. 2015.

[34] O. D. Gentilini, M.-J. Cardoso, and P. Poortmans, "Less is more. breast conservation might be even better than mastectomy in early breast cancer patients," *The Breast*, vol. 35, p. 32–33, Oct. 2017.

[35] E. Silva and M. Tan, "The impact of margin status on breast conservation rates," *Annals of Surgical Oncology*, vol. 26, p. 3931–3938, Sept. 2019.

[36] R. Nash, M. Goodman, C. C. Lin, R. A. Freedman, L. S. Dominici, K. Ward, and A. Jemal, "State variation in the receipt of a contralateral prophylactic mastectomy among women who received a diagnosis of invasive unilateral early-stage breast cancer in the united states, 2004-2012," *JAMA Surgery*, vol. 152, p. 648, July 2017.

[37] K. L. Kummerow, L. Du, D. F. Penson, Y. Shyr, and M. A. Hooks, "Nationwide trends in mastectomy for early-stage breast cancer," *JAMA Surgery*, vol. 150, p. 9, Jan. 2015.

[38] C. R. Albornoz, E. Matros, C. N. Lee, C. A. Hudis, A. L. Pusic, E. Elkin, P. B. Bach, P. G. Cordeiro, and M. Morrow, "Bilateral mastectomy versus breast-conserving surgery for early-stage breast cancer: The role of breast reconstruction," *Plastic and Reconstructive Surgery*, vol. 135, p. 1518–1526, June 2015.

[39] N. Johns and J. Dixon, "Should patients with early breast cancer still be offered the choice of breast conserving surgery or mastectomy?," *European Journal of Surgical Oncology (EJSO)*, vol. 42, p. 1636–1641, Nov. 2016.

[40] American College of Surgeons, *National Accrediation Program for Breast Centers (NAPBC) Standards Manual 2018 Edition*, 2018.

[41] K. C. Oeffinger, E. T. H. Fontham, R. Etzioni, A. Herzig, J. S. Michaelson, Y.-C. T. Shih, L. C. Walter, T. R. Church, C. R. Flowers, S. J. LaMonte, A. M. D. Wolf, C. DeSantis, J. Lortet-Tieulent, K. Andrews, D. Manassaram-Baptiste, D. Saslow, R. A. Smith, O. W. Brawley, and R. Wender, "Breast cancer screening for women at average risk: 2015 guideline update from the american cancer society," *JAMA*, vol. 314, p. 1599, Oct. 2015.

[42] D. Wiese, A. M. Stroup, F. Islami, M. Mattes, E. Baylor, F. P. Boscoe, and K. A. Henry, "Geographic diffusion of digital mammography in the united states," *Cancer*, vol. 129, p. 2144–2151, Mar. 2023.

[43] S. M. Friedewald, *Breast Cancer Screening: The Debate that Never Ends*, p. 31–38. Springer International Publishing, 2018.

[44] S. W. Duffy, L. Tabár, A. M. Yen, P. B. Dean, R. A. Smith, H. Jonsson, S. Törnberg, S. L. Chen, S. Y. Chiu, J. C. Fann, M. M. Ku, W. Y. Wu, C. Hsu, Y. Chen, G. Svane, E. Azavedo, H. Grundström, P. Sundén, K. Leifland, E. Frodis, J. Ramos, B. Epstein, A. Åkerlund, A. Sundbom, P. Bordás, H. Wallin, L. Starck, A. Björkgren, S. Carlson, I. Fredriksson, J. Ahlgren, D. Öhman, L. Holmberg, and T. H. Chen, "Mammography screening reduces rates of advanced and fatal breast cancers: Results in 549, 091 women," *Cancer*, vol. 126, p. 2971–2979, May 2020.

[45] K. Kerlikowske, W. Zhu, A. N. Tosteson, B. L. Sprague, J. A. Tice, C. D. Lehman, and D. L. Miglioretti, "Identifying women with dense breasts at high risk for interval cancer: A cohort study," *Annals of Internal Medicine*, vol. 162, p. 673–681, May 2015.

[46] M. Bahl, S. Mercaldo, A. M. McCarthy, and C. D. Lehman, "Imaging surveillance of breast cancer survivors with digital mammography versus digital breast tomosynthesis," *Radiology*, vol. 298, p. 308–316, Feb. 2021.

[47] K. Kerlikowske, Y.-R. Su, B. L. Sprague, A. N. A. Tosteson, D. S. M. Buist, T. Onega, L. M. Henderson, N. Alsheik, M. C. S. Bissell, E. S. O'Meara, C. I. Lee, and D. L. Miglioretti, "Association of screening with digital breast tomosynthesis vs digital mammography with risk of interval invasive and advanced breast cancer," *JAMA*, vol. 327, p. 2220, June 2022.

[48] I. B. Richman, J. R. Hoag, X. Xu, H. P. Forman, R. Hooley, S. H. Busch, and C. P. Gross, "Adoption of digital breast tomosynthesis in clinical practice," *JAMA internal medicine*, vol. 179, no. 9, pp. 1292–1295, 2019.

[49] G. L. Menezes, "Magnetic resonance imaging in breast cancer: A literature review and future perspectives," *World Journal of Clinical Oncology*, vol. 5, no. 2, p. 61, 2014.

[50] C. K. Kuhl, A. Keulers, K. Strobel, H. Schneider, N. Gaisa, and S. Schrading, "Not all false positive diagnoses are equal: On the prognostic implications of false-positive diagnoses made in breast mri versus in mammography / digital tomosynthesis screening," *Breast Cancer Research*, vol. 20, Feb. 2018.

[51] H. Hussein, E. Abbas, S. Keshavarzi, R. Fazelzad, K. Bukhanov, S. Kulkarni, F. Au, S. Ghai, A. Alabousi, and V. Freitas, "Supplemental breast cancer screening in women with dense breasts and negative mammography: A systematic review and meta-analysis," *Radiology*, vol. 306, Mar. 2023.

[52] A. Fausto, A. Fanizzi, L. Volterrani, F. G. Mazzei, C. Calabrese, D. Casella, M. Marcasciano, R. Massafra, D. La Forgia, and M. A. Mazzei, "Feasibility, image quality and clinical evaluation of contrast-enhanced breast mri performed in a supine position compared to the standard prone position," *Cancers*, vol. 12, p. 2364, Aug. 2020.

[53] P. Siegler, C. M. Holloway, P. Causer, G. Thevathasan, and D. B. Plewes, "Supine breast mri," *Journal of Magnetic Resonance Imaging*, vol. 34, p. 1212–1217, Sept. 2011.

[54] C.-B. Wang, S. Lee, T. Kim, D. Hong, G. B. Kim, G. Y. Yoon, H. H. Kim, N. Kim, and B. Ko, "Breast tumor movements analysis using mri scans in prone and supine positions," *Scientific Reports*, vol. 10, Mar. 2020.

[55] B. K. Byrd, V. Krishnaswamy, J. Gui, T. Rooney, R. Zuurbier, K. Rosenkranz, K. Paulsen, and R. J. Barth, "The shape of breast cancer," *Breast Cancer Research and Treatment*, vol. 183, p. 403–410, July 2020.

[56] M. Sakakibara, T. Nagashima, T. Sangai, R. Nakamura, H. Fujimoto, M. Arai, T. Kazama, H. Hashimoto, Y. Nakatani, and M. Miyazaki, "Breast-conserving surgery using projection and reproduction techniques of surgical-position breast mri in patients with ductal carcinoma in situ of the breast," *Journal of the American College of Surgeons*, vol. 207, p. 62–68, July 2008.

[57] M. Abe, T. Kiryu, K. Sonoda, and Y. Kashiki, "Magnetic resonance imaging-guided navigation with a thermoplastic shell for breast-conserving surgery," *European Journal of Surgical Oncology (EJSO)*, vol. 37, p. 950–955, Nov. 2011.

[58] G. Kutomi, H. Shima, D. Kyuno, F. Satomi, A. Wada, Y. Kuga, M. Okazaki, A. Okazaki, H. Masuoka, T. Mikami, Y. Yuyama, T. Matsuno, T. Ohmura, H. Kameshima, T. Mizuguchi, and I. Takemasa, "Positional advantages of supine mri for diagnosis prior to breast-conserving surgery," *Molecular and Clinical Oncology*, vol. 18, Apr. 2023.

[59] A. Fausto, M. Bernini, D. La Forgia, A. Fanizzi, M. Marcasciano, L. Volterrani, D. Casella, and M. A. Mazzei, "Six-year prospective evaluation of second-look us with volume navigation for mri-detected additional breast lesions," *European Radiology*, vol. 29, p. 1799–1808, Oct. 2018.

[60] L. Shang, Z. Liu, Y. Rong, T. Zhou, and L. Zuo, "Mri in breast cancer radiotherapy in prone and supine positions," *Front Biosci*, vol. 22, pp. 570–9, 2017.

[61] S. Iranmakani, T. Mortezazadeh, F. Sajadian, M. F. Ghaziani, A. Ghafari, D. Khezerloo, and A. E. Musa, "A review of various modalities in breast imaging: technical aspects and clinical outcomes," *Egyptian Journal of Radiology and Nuclear Medicine*, vol. 51, Apr. 2020.

[62] L. Yang, S. Wang, L. Zhang, C. Sheng, F. Song, P. Wang, and Y. Huang, "Performance of ultrasonography screening for breast cancer: a systematic review and meta-analysis," *BMC Cancer*, vol. 20, June 2020.

[63] N. Aristokli, I. Polycarpou, S. Themistocleous, D. Sophocleous, and I. Mamais, "Comparison of the diagnostic performance of magnetic resonance imaging (mri), ultrasound and mammography for detection of breast cancer based on tumor type, breast density and patient's history: A review," *Radiography*, vol. 28, p. 848–856, Aug. 2022.

[64] R. Guo, G. Lu, B. Qin, and B. Fei, "Ultrasound imaging technologies for breast cancer detection and management: A review," *Ultrasound in Medicine and Biology*, vol. 44, p. 37–70, Jan. 2018.

[65] M. Specht, "Left lumpectomy with wireless seed localization for ductal carcinoma in situ," *Journal of Medical Insight*, June 2021.

[66] M. S. Moran, S. J. Schnitt, A. E. Giuliano, J. R. Harris, S. A. Khan, J. Horton, S. Klimberg, M. Chavez-MacGregor, G. Freedman, N. Houssami, P. L. Johnson, and M. Morrow, "Society of surgical oncology–american society for radiation oncology consensus guideline on margins for breast-conserving surgery with whole-breast irradiation in stages i and ii invasive breast cancer," *Journal of Clinical Oncology*, vol. 32, p. 1507–1515, May 2014.

[67] M. Morrow, K. J. Van Zee, L. J. Solin, N. Houssami, M. Chavez-MacGregor, J. R. Harris, J. Horton, S. Hwang, P. L. Johnson, M. L. Marinovich, S. J. Schnitt, I. Wapnir, and M. S. Moran, "Society of surgical oncology–american society for radiation oncology–american society of clinical oncology consensus guideline on margins for breast-conserving surgery with whole-breast irradiation in ductal carcinoma in situ," *Practical Radiation Oncology*, vol. 6, p. 287–295, Sept. 2016.

[68] A. A. Heelan Gladden, S. Sams, A. Gleisner, C. Finlayson, N. Kounalakis, P. Hosokawa, R. Brown, T. Chong, D. Mathes, and C. Murphy, "Re-excision rates after breast conserving surgery following the 2014 sso-astro guidelines," *The American Journal of Surgery*, vol. 214, p. 1104–1109, Dec. 2017.

[69] B. W. Maloney, D. M. McClatchy, B. W. Pogue, K. D. Paulsen, W. A. Wells, and R. J. Barth, "Review of methods for intraoperative margin detection for breast conserving surgery," *Journal of Biomedical Optics*, vol. 23, p. 1, Oct. 2018.

[70] J. M. Jorns, D. Visscher, M. Sabel, T. Breslin, P. Healy, S. Daignaut, J. L. Myers, and A. J. Wu, "Intraoperative frozen section analysis of margins in breast conserving surgery significantly decreases reoperative rates," *American Journal of Clinical Pathology*, vol. 138, p. 657–669, Nov. 2012.

[71] A. B. Chagpar, M. Butler, B. K. Killelea, N. R. Horowitz, K. Stavris, and D. R. Lannin, "Does three-dimensional intraoperative specimen imaging reduce the need for re-excision in breast cancer patients? a prospective cohort study," *The American Journal of Surgery*, vol. 210, p. 886–890, Nov. 2015.

[72] W. Li and X. Li, "Development of intraoperative assessment of margins in breast conserving surgery: a narrative review," *Gland Surgery*, vol. 11, p. 258–269, Jan. 2022.

[73] V. J. Reid, J. S. Falk, A. M. Police, C. A. Ridgeway, L. L. Cadena, and S. P. Povoski, "Minimizing re-excision after breast conserving surgery – a review of radiofrequency spectroscopy for real-time, intraoperative margin assessment," *Expert Review of Medical Devices*, vol. 18, p. 1057–1068, Nov. 2021.

[74] F. Schnabel, S. K. Boolbol, M. Gittleman, T. Karni, L. Tafra, S. Feldman, A. Police, N. B. Friedman, S. Karlan, D. Holmes, S. C. Willey, M. Carmon, K. Fernandez, S. Akbari, J. Harness, L. Guerra, T. Frazier, K. Lane, R. M. Simmons, A. Estabrook, and T. Allweis, "A randomized prospective study of lumpectomy margin assessment with use of marginprobe in patients with nonpalpable breast malignancies," *Annals of Surgical Oncology*, vol. 21, p. 1589–1595, Mar. 2014.

[75] S. Fisher, Y. Yasui, K. Dabbs, and M. Winget, "Re-excision and survival following breast conserving surgery in early stage breast cancer patients: a population-based study," *BMC Health Services Research*, vol. 18, Feb. 2018.

[76] L. G. Wilke, T. Czechura, C. Wang, B. Lapin, E. Liederbach, D. P. Winchester, and K. Yao, "Repeat surgery after breast conservation for the treatment of stage 0 to ii breast carcinoma: A report from the national cancer data base, 2004-2010," *JAMA Surgery*, vol. 149, p. 1296, Dec. 2014.

[77] L. E. McCahill, R. M. Single, E. J. Aiello Bowles, H. S. Feigelson, T. A. James, T. Barney, J. M. Engel, and A. A. Onitilo, "Variability in reexcision following breast conservation surgery," *JAMA*, vol. 307, p. 467, Feb. 2012.

[78] M. L. Marinovich, N. Noguchi, M. Morrow, and N. Houssami, "Changes in reoperation after publication of consensus guidelines on margins for breast-conserving surgery: A systematic review and meta-analysis," *JAMA Surgery*, vol. 155, p. e203025, Oct. 2020.

[79] M. Azu, P. Abrahamse, S. J. Katz, R. Jagsi, and M. Morrow, "What is an adequate margin for breast-conserving surgery? surgeon attitudes and correlates," *Annals of Surgical Oncology*, vol. 17, p. 558–563, Oct. 2009.

[80] S. L. Blair, K. Thompson, J. Rococco, V. Malcarne, P. D. Beitsch, and D. W. Ollila, "Attaining negative margins in breast-conservation operations: Is there a consensus among breast surgeons?," *Journal of the American College of Surgeons*, vol. 209, p. 608–613, Nov. 2009.

[81] H. H. Abidi, E. B. Littleton, P. F. McAuliffe, R. R. Johnson, J. G. Steiman, and E. J. Diego, "Unpacking the surgical approach to nonpalpable breast lesions: bridging the knowledge gap between educators and trainees," *Global Surgical Education - Journal of the Association for Surgical Education*, vol. 3, Dec. 2023.

[82] S. Q. Vrouwe, R. B. Somogyi, L. Snell, C. McMillan, D. Vesprini, and J. E. Lipa, "Patient-reported outcomes following breast conservation therapy and barriers to referral for partial breast reconstruction," *Plastic and Reconstructive Surgery*, vol. 141, p. 1–9, Jan. 2018.

[83] S. E. Abe, J. S. Hill, Y. Han, K. Walsh, J. T. Symanowski, L. Hadzikadic-Gusic, T. Flippo-Morton, T. Sarantou, M. Forster, and R. L. White, "Margin re-excision and local recurrence in invasive breast cancer: A cost analysis using a decision tree model," *Journal of Surgical Oncology*, vol. 112, p. 443–448, Aug. 2015.

[84] E. Cheang, R. Ha, C. M. Thornton, and V. L. Mango, "Innovations in image-guided preoperative breast lesion localization," *The British Journal of Radiology*, p. 20170740, Feb. 2018.

[85] J. D. Luiten, M. A. Beek, A. C. Voogd, P. D. Gobardhan, and E. J. T. Luiten, "Iodine seed- versus wire-guided localization in breast-conserving surgery for non-palpable ductal carcinoma in situ," *British Journal of Surgery*, vol. 102, p. 1665–1669, Oct. 2015.

[86] B. in 't Hout, K. Schenk, A. van der Linden, and R. Roumen, "Efficacy of localization of non-palpable, invasive breast cancer: Wire localization vs. iodine-125 seed: A historical comparison," *The Breast*, vol. 29, p. 8–13, Oct. 2016.

[87] I. T. Rubio, A. Esgueva-Colmenarejo, M. Espinosa-Bravo, J. P. Salazar, I. Miranda, and V. Peg, "Intraoperative ultrasound-guided lumpectomy versus mammographic wire localization for breast cancer patients after neoadjuvant treatment," *Annals of Surgical Oncology*, vol. 23, p. 38–43, Oct. 2015.

[88] L. Langhans, M.-B. Jensen, M.-L. M. Talman, I. Vejborg, N. Kroman, and T. F. Tvedskov, "Reoperation rates in ductal carcinoma in situ vs invasive breast cancer after wire-guided breast-conserving surgery," *JAMA Surgery*, vol. 152, p. 378, Apr. 2017.

[89] C. I. Theunissen, E. A. Rust, M. A. Edens, C. Bandel, J. G. van't Ooster-van den Berg, P. L. Jager, E. M. Noorda, and A. B. Francken, "Radioactive seed localization is the preferred technique in nonpalpable breast cancer compared with wire-guided localization and radioguided occult lesion localization," *Nuclear Medicine Communications*, vol. 38, p. 396–401, May 2017.

[90] V. T. Tran, J. David, E. Patocskai, M. Zummo-Soucy, R. Younan, L. Lalonde, M. Labelle, M. El Khoury, A. Robidoux, and I. Trop, "Comparative evaluation of iodine-125 radioactive seed localization and wire localization for resection of breast lesions," *Canadian Association of Radiologists Journal*, vol. 68, p. 447–455, Nov. 2017.

[91] S. N. Patel, V. L. Mango, P. Jadeja, L. Friedlander, E. Desperito, R. Wynn, S. Feldman, and R. Ha, "Reflector-guided breast tumor localization versus wire localization for lumpectomies: A comparison of surgical outcomes," *Clinical Imaging*, vol. 47, p. 14–17, Jan. 2018.

[92] L. Stelle, T. Schoenheit, A. Brubaker, X. Tang, P. Qu, K. Cradock, and A. Higham, "Radioactive seed localization versus wire localization for nonpalpable breast lesions: A two-year initial experience at a large community hospital," *Annals of Surgical Oncology*, vol. 25, p. 131–136, Nov. 2017.

[93] K. Zacharioudakis, S. Down, Z. Bholah, S. Lee, T. Khan, A. J. Maxwell, M. Howe, and J. Harvey, "Is the future magnetic? magseed localisation for non palpable breast cancer. a multi-centre non randomised control study," *European Journal of Surgical Oncology*, vol. 45, p. 2016–2021, Nov. 2019.

[94] X. Hu, S. Li, Y. Jiang, W. Wei, Y. Ji, Q. Li, and Z. Jiang, "Intraoperative ultrasound-guided lumpectomy versus wire-guided excision for nonpalpable breast cancer," *Journal of International Medical Research*, vol. 48, p. 030006051989670, Jan. 2020.

[95] S. Joukainen, H. Okuma, O. Kaarela, E. Laaksonen, V. Kärjä, R. Vanninen, A. Masarwah, and M. Sudah, "Can supine breast magnetic resonance imaging help hit the target in extreme oncoplastic surgery?," *European Journal of Surgical Oncology*, vol. 47, p. 2788–2796, Nov. 2021.

[96] J. S. Montrey, J. A. Levy, and R. J. Brenner, "Wire fragments after needle localization.," *American Journal of Roentgenology*, vol. 167, p. 1267–1269, Nov. 1996.

[97] M. Sheetz and C. Steiner, "Compliance with the u.s. nuclear regulatory commission revised licensing guidance for radioactive seed localization," *Health Physics*, vol. 115, p. 402–408, Sept. 2018.

[98] J. O. Murphy, T.-A. Moo, T. A. King, K. J. Van Zee, K. A. Villegas, M. Stempel, A. Eaton, J. M. St. Germain, E. Morris, and M. Morrow, "Radioactive seed localization compared to wire localization in breast-conserving surgery: Initial 6-month experience," *Annals of Surgical Oncology*, vol. 20, p. 4121–4127, Aug. 2013.

[99] M. van der Noordaa, K. Pengel, E. Groen, E. van Werkhoven, E. Rutgers, C. Loo, W. Vogel, and M. Vrancken Peeters, "The use of radioactive iodine-125 seed localization in patients with nonpalpable breast cancer," *European Journal of Surgical Oncology (EJSO)*, vol. 41, p. 553–558, Apr. 2015.

[100] N. Krekel, B. Zonderhuis, S. Muller, H. Bril, H.-J. van Slooten, E. de Lange de Klerk, P. van den Tol, and S. Meijer, "Excessive resections in breast-conserving surgery: A retrospective multicentre study: Excessive resections in breast-conserving surgery," *The Breast Journal*, vol. 17, p. 602–609, Nov. 2011.

[101] E. Parvez, S. D. Cornacchi, N. Hodgson, A. Thoma, I. Kong, G. Foster, J. Cheng, C. H. Goldsmith, D. Dao, and P. J. Lovrics, "A cosmesis outcome substudy in a prospective, randomized trial comparing radioguided seed localization with standard wire localization for nonpalpable, invasive, and in situ breast carcinomas," *The American Journal of Surgery*, vol. 208, p. 711–718, Nov. 2014.

[102] E. V. Bloomquist, N. Ajkay, S. Patil, A. E. Collett, T. G. Frazier, and A. V. Barrio, "A randomized prospective comparison of patient-assessed satisfaction and clinical outcomes with radioactive seed localization versus wire localization," *The Breast Journal*, vol. 22, p. 151–157, Dec. 2015.

[103] A. E. Micha, V. Sinnett, K. Downey, S. Allen, B. Bishop, L. R. Hector, E. P. Patrick, R. Edmonds, P. A. Barry, K. D. C. Krupa, and J. E. Rusby, "Patient and clinician satisfaction and clinical outcomes of magseed compared with wire-guided localisation for impalpable breast lesions," *Breast Cancer*, vol. 28, p. 196–205, Sept. 2020.

[104] L. R. Lamb, M. Bahl, M. C. Specht, H. A. D'Alessandro, and C. D. Lehman, "Evaluation of a nonradioactive magnetic marker wireless localization program," *American Journal of Roentgenology*, vol. 211, p. 940–945, Oct. 2018.

[105] D. Thekkinkattil, M. Kaushik, M. Hoosein, M. Al-Attar, S. Pilgrim, A. Gvaramadze, L. Hyklova, and A. Jibril, "A prospective, single-arm, multicentre clinical evaluation of a new localisation technique using non-radioactive magseeds for surgery of clinically occult breast lesions," *Clinical Radiology*, vol. 74, pp. 974.e7–974.e11, Dec. 2019.

[106] E. R. Price, A. L. Khoury, L. J. Esserman, B. N. Joe, and M. D. Alvarado, "Initial clinical experience with an inducible magnetic seed system for preoperative breast lesion localization," *American Journal of Roentgenology*, vol. 210, p. 913–917, Apr. 2018.

[107] J. Reid, S. Tovey, E. Campbell, S. Pareek, J. Kelly, P. Law, J. Coldeway, E. Mumba, and S. Elgammal, "29. the magseed® experience: One year on," *European Journal of Surgical Oncology*, vol. 45, p. 884, May 2019.

[108] M. K. Hayes, "Update on preoperative breast localization," *Radiologic Clinics of North America*, vol. 55, p. 591–603, May 2017.

[109] C. E. Cox, N. Garcia-Henriquez, M. J. Glancy, P. Whitworth, J. M. Cox, M. Themar-Geck, R. Prati, M. Jung, S. Russell, K. Appleton, J. King, and S. C. Shivers, "Pilot study of a new nonradioactive surgical guidance technology for locating nonpalpable breast lesions," *Annals of Surgical Oncology*, vol. 23, p. 1824–1830, Feb. 2016.

[110] C. E. Cox, S. Russell, V. Prowler, E. Carter, A. Beard, A. Mehindru, P. Blumencranz, K. Allen, M. Portillo, P. Whitworth, K. Funk, J. Barone, D. Norton, J. Schroeder, A. Police, E. Lin, F. Combs, F. Schnabel, H. Toth, J. Lee, B. Anglin, M. Nguyen, L. Canavan, A. Laidley, M. J. Warden, R. Prati, J. King, and S. C. Shivers, "A prospective, single arm, multi-site, clinical evaluation of a nonradioactive surgical guidance technology for the location of nonpalpable breast lesions during excision," *Annals of Surgical Oncology*, vol. 23, p. 3168–3174, July 2016.

[111] P. H. Jadeja, V. Mango, S. Patel, L. Friedlander, E. Desperito, E. Ayala-Bustamante, R. Wynn, M. Chen-Seetoo, B. Taback, S. Feldman, and R. Ha, "Utilization of multiple savi scout surgical guidance system reflectors in the same breast: A single-institution feasibility study," *The Breast Journal*, vol. 24, p. 531–534, Dec. 2017.

[112] N. Janssen, R. van la Parra, C. Loo, E. Groen, M. van den Berg, H. Oldenburg, J. Nijkamp, and M. Vrancken Peeters, "Breast conserving surgery for extensive dcis using multiple radioactive seeds," *European Journal of Surgical Oncology*, vol. 44, p. 67–73, Jan. 2018.

[113] K. A. Carlson, C. Checka, K. K. Hunt, J. Jung, C. Bridges, P. Singh, A. Refinetti, T. Moseley, F. Perez, C. Mayo, and N. Tamirisa, "Evaluation of a surgical navigation system for localization and excision of nonpalpable lesions in breast and axillary surgery," *The Breast Journal*, vol. 2023, p. 1–7, Dec. 2023.

[114] H. Karanlik, I. Ozgur, D. Sahin, M. Fayda, S. Onder, and E. Yavuz, "Intraoperative ultrasound reduces the need for re-excision in breast-conserving surgery," *World Journal of Surgical Oncology*, vol. 13, Nov. 2015.

[115] J. Volders, M. Haloua, N. Krekel, V. Negenborn, R. Kolk, A. Lopes Cardozo, A. Bosch, L. de Widt-Levert, H. van der Veen, H. Rijna, A. Taets van Amerongen, K. Jóźwiak, S. Meijer, and M. van den Tol, "Intraoperative ultrasound guidance in breast-conserving surgery shows superiority in oncological outcome, long-term cosmetic and patient-reported outcomes," *European Journal of Surgical Oncology (EJSO)*, vol. 43, p. 649–657, Apr. 2017.

[116] G. Karadeniz Cakmak, A. U. Emre, O. Tascilar, B. Bahadir, and S. Ozkan, "Surgeon performed continuous intraoperative ultrasound guidance decreases re-excisions and mastectomy rates in breast cancer," *The Breast*, vol. 33, p. 23–28, June 2017.

[117] A. D. Gerrard and A. Shrotri, "Surgeon-led intraoperative ultrasound localization for nonpalpable breast cancers: Results of 5 years of practice," *Clinical Breast Cancer*, vol. 19, p. e748–e752, Dec. 2019.

[118] M. Ferrucci, F. Milardi, D. Passeri, L. F. Mpungu, A. Francavilla, M. Cagol, T. Saibene, S. Michieletto, M. Toffanin, P. Del Bianco, U. Grossi, and A. Marchet, "Intraoperative ultrasound-guided conserving surgery for breast cancer: No more time for blind surgery," *Annals of Surgical Oncology*, vol. 30, p. 6201–6214, Aug. 2023.

[119] P. Argacha, T. Cortadellas, J. Acosta, X. Gonzalez-Farré, and M. Xiberta, "Comparison of ultrasound guided surgery and radio-guided occult lesions localization (roll) for nonpalpable breast cancer excision," *Gland Surgery*, vol. 12, p. 1233–1241, Sept. 2023.

[120] N. M. Krekel, M. H. Haloua, A. M. Lopes Cardozo, R. H. de Wit, A. M. Bosch, L. M. de Widt-Levert, S. Muller, H. van der Veen, E. Bergers, E. S. de Lange de Klerk, S. Meijer, and M. P. van den Tol, "Intraoperative ultrasound guidance for palpable breast cancer excision (cobalt trial): a multicentre, randomised controlled trial," *The Lancet Oncology*, vol. 14, p. 48–54, Jan. 2013.

[121] M. H. Haloua, J. H. Volders, N. M. A. Krekel, A. M. F. Lopes Cardozo, W. K. de Roos, L. M. de Widt-Levert, H. van der Veen, H. Rijna, E. Bergers, K. Jóźwiak, S. Meijer, and M. P. van den Tol, "Intraoperative ultrasound guidance in breast-conserving surgery improves cosmetic outcomes and patient satisfaction: Results of a multicenter randomized controlled trial (cobalt)," *Annals of Surgical Oncology*, vol. 23, p. 30–37, Oct. 2015.

[122] K. M. Davis, C.-H. Hsu, M. E. Bouton, K. L. Wilhelmson, and I. K. Komenaka, "Intraoperative ultrasound can decrease the re-excision lumpectomy rate in patients with palpable breast cancers," *The American Surgeon*, vol. 77, p. 720–725, June 2011.

[123] N. Krekel, A. Lopes Cardozo, S. Muller, E. Bergers, S. Meijer, and M. van den Tol, "Optimising surgical accuracy in palpable breast cancer with intra-operative breast ultrasound – feasibility and surgeons' learning curve," *European Journal of Surgical Oncology (EJSO)*, vol. 37, p. 1044–1050, Dec. 2011.

[124] V. S. Klimberg, "Advances in the diagnosis and excision of breast cancer," *The American Surgeon*, vol. 69, p. 11–14, Jan. 2003.

[125] M. K. Shetty and A. B. Watson Jr., "Sonographically occult screen detected breast masses: a retrospective analysis of cases undergoing biopsy," *Clinical Imaging*, vol. 32, p. 28–31, Jan. 2008.

[126] W. Jakubowski, K. Dobruch-Sobczak, and B. Migda, "Errors and mistakes in breast ultrasound diagnostics," *Journal of Ultrasonography*, vol. 12, p. 286–298, Sept. 2012.

[127] T. Uematsu, "Non-mass-like lesions on breast ultrasonography: a systematic review," *Breast Cancer*, vol. 19, p. 295–301, Mar. 2012.

[128] J. A. Baker, M. S. Soo, and E. L. Rosen, "Artifacts and pitfalls in sonographic imaging of the breast," *American Journal of Roentgenology*, vol. 176, p. 1261–1266, May 2001.

[129] M. Carmon, O. Olsha, D. Gekhtman, I. Nikitin, Y. Cohen, M. Messing, N. Lioubashevsky, R. Abu Dalo, T. Hadar, and E. Golomb, "Detectability of hygroscopic clips used in breast cancer surgery," *Journal of Ultrasound in Medicine*, vol. 36, p. 401–408, Dec. 2016.

[130] C. Peng, Q. Cai, M. Chen, and X. Jiang, "Recent advances in tracking devices for biomedical ultrasound imaging applications," *Micromachines*, vol. 13, p. 1855, Oct. 2022.

[131] T. Ungi, G. Gauvin, A. Lasso, C. T. Yeo, P. Pezeshki, T. Vaughan, K. Carter, J. Rudan, C. J. Engel, and G. Fichtinger, "Navigated breast tumor excision using electromagnetically tracked ultrasound and surgical instruments," *IEEE Transactions on Biomedical Engineering*, vol. 63, p. 600–606, Mar. 2016.

[132] R. J. Barth, V. Krishnaswamy, K. D. Paulsen, T. B. Rooney, W. A. Wells, E. Rizzo, C. V. Angeles, J. D. Marotti, R. A. Zuurbier, and C. C. Black, "A patient-specific 3d-printed form accurately transfers supine mri-derived tumor localization information to guide breast-conserving surgery," *Annals of Surgical Oncology*, vol. 24, p. 2950–2956, Aug. 2017.

[133] Z.-Y. Wu, H. J. Kim, J. Lee, I. Y. Chung, J. Kim, S. Lee, B. H. Son, S.-H. Ahn, H. H. Kim, J. B. Seo, J. H. Jeong, G. Gong, N. Kim, and B. Ko, "Breast-conserving surgery with 3d-printed surgical guide: a single-center, prospective clinical study," *Scientific Reports*, vol. 11, Jan. 2021.

[134] S. L. Perkins, M. A. Lin, S. Srinivasan, A. J. Wheeler, B. A. Hargreaves, and B. L. Daniel, "A mixed-reality system for breast surgical planning," in *2017 IEEE International Symposium on Mixed and Augmented Reality (ISMAR-Adjunct)*, IEEE, Oct. 2017.

[135] P. F. Gouveia, J. Costa, P. Morgado, R. Kates, D. Pinto, C. Mavioso, J. Anacleto, M. Martinho, D. S. Lopes, A. R. Ferreira, V. Vavourakis, M. Hadjicharalambous, M. A. Silva, N. Papanikolaou, C. Alves, F. Cardoso, and M. J. Cardoso, "Breast cancer surgery with augmented reality," *The Breast*, vol. 56, p. 14–17, Apr. 2021.

[136] L. Lan, Y. Xia, R. Li, K. Liu, J. Mai, J. A. Medley, S. Obeng-Gyasi, L. K. Han, P. Wang, and J.-X. Cheng, "A fiber optoacoustic guide with augmented reality for precision breast-conserving surgery," *Light: Science and Applications*, vol. 7, May 2018.

[137] J. Ock, S. Moon, M. Kim, B. S. Ko, and N. Kim, "Evaluation of the accuracy of an augmented reality-based tumor-targeting guide for breast-conserving surgery," *Computer Methods and Programs in Biomedicine*, vol. 245, p. 108002, Mar. 2024.

[138] R. H. Conley, I. M. Meszoely, J. A. Weis, T. S. Pheiffer, L. R. Arlinghaus, T. E. Yankeelov, and M. I. Miga, "Realization of a biomechanical model-assisted image guidance system for breast cancer surgery using supine mri," *International Journal of Computer Assisted Radiology and Surgery*, vol. 10, p. 1985–1996, June 2015.

[139] W. L. Richey, J. S. Heiselman, M. J. Ringel, I. M. Meszoely, and M. I. Miga, "Computational imaging to compensate for soft-tissue deformations in image-guided breast conserving surgery," *IEEE Transactions on Biomedical Engineering*, vol. 69, no. 12, pp. 3760–3771, 2022.

[140] A. J. Darlington, *Anatomy of the Breast*, p. 3–10. Springer International Publishing, 2015.

[141] N. G. Ramião, P. S. Martins, R. Rynkevic, A. A. Fernandes, M. Barroso, and D. C. Santos, "Biomechanical properties of breast tissue, a state-of-the-art review," *Biomechanics and Modeling in Mechanobiology*, vol. 15, p. 1307–1323, Feb. 2016.

[142] E. Chen, J. Novakofski, W. Jenkins, and W. O'Brien, "Young's modulus measurements of soft tissues with application to elasticity imaging," *IEEE Transactions on Ultrasonics, Ferroelectrics and Frequency Control*, vol. 43, p. 191–194, Jan. 1996.

[143] M. T. Islam, S. Tang, C. Liverani, S. Saha, E. Tasciotti, and R. Righetti, "Non-invasive imaging of young's modulus and poisson's ratio in cancers in vivo," *Scientific Reports*, vol. 10, Apr. 2020.

[144] T. A. Krouskop, T. M. Wheeler, F. Kallel, B. S. Garra, and T. Hall, "Elastic moduli of breast and prostate tissues under compression," *Ultrasonic Imaging*, vol. 20, p. 260–274, Oct. 1998.

[145] T. Matsumura, T. Umemoto, Y. Fujihara, E. Ueno, M. Yamakawa, T. Shiina, and T. Mitake, "Measurement of elastic property of breast tissue for elasticity imaging," in *2009 IEEE International Ultrasonics Symposium*, pp. 1451–1454, 2009.

[146] X. Li, J.-N. Wang, Z.-Y. Fan, S. Kang, Y.-J. Liu, Y.-X. Zhang, and X.-M. Wang, "Determination of the elasticity of breast tissue during the menstrual cycle using real-time shear wave elastography," *Ultrasound in Medicine and Biology*, vol. 41, p. 3140–3147, Dec. 2015.

[147] B. K. Patel, N. Samreen, Y. Zhou, J. Chen, K. Brandt, R. Ehman, and K. Pepin, "Mr elastography of the breast: Evolution of technique, case examples, and future directions," *Clinical Breast Cancer*, vol. 21, p. e102–e111, Feb. 2021.

[148] R. H. Griesenauer, J. A. Weis, L. R. Arlinghaus, I. M. Meszoely, and M. I. Miga, "Toward quantitative quasistatic elastography with a gravity-induced deformation source for image-guided breast surgery," *Journal of Medical Imaging*, vol. 5, no. 1, p. 015003, 2018.

[149] J. Zhou, Z. Yang, W. Zhan, Y. Dong, and C. Zhou, "Anisotropic properties of breast tissue measured by acoustic radiation force impulse quantification," *Ultrasound in Medicine and Biology*, vol. 42, p. 2372–2382, Oct. 2016.

[150] R. Sinkus, M. Tanter, S. Catheline, J. Lorenzen, C. Kuhl, E. Sondermann, and M. Fink, "Imaging anisotropic and viscous properties of breast tissue by magnetic resonance-elastography," *Magnetic Resonance in Medicine*, vol. 53, p. 372–387, Jan. 2005.

[151] N. Briot, G. Chagnon, L. Burlet, H. Gil, E. Girard, and Y. Payan, "Experimental characterisation and modelling of breast cooper's ligaments," *Biomechanics and Modeling in Mechanobiology*, vol. 21, p. 1157–1168, Apr. 2022.

[152] L. Ruggiero, H. Sol, H. Sahli, S. Adriaenssens, and N. Adriaenssens, "The effect of material modeling on finite element analysis of human breast biomechanics," *Journal of Applied Biomaterials and Functional Materials*, vol. 12, p. 27–34, Jan. 2014.

[153] A. F. Bower, *Applied mechanics of solids*. CRC press, 2009.

[154] P. Wellman, R. D. Howe, E. Dalton, and K. A. Kern, "Breast tissue stiffness in compression is correlated to histological diagnosis," *Harvard BioRobotics Laboratory Technical Report*, vol. 1, 1999.

[155] A. Samani, J. Bishop, M. Yaffe, and D. Plewes, "Biomechanical 3-d finite element modeling of the human breast using mri data," *IEEE Transactions on Medical Imaging*, vol. 20, p. 271–279, Apr. 2001.

[156] P. R. Bakic, *Breast tissue description and modeling in mammography*. Lehigh University, 2001.

[157] J. Lorenzen, R. Sinkus, M. Lorenzen, M. Dargatz, C. Leussler, P. Röschmann, and G. Adam, "Mr elastography of the breast:preliminary clinical results," *RöFo - Fortschritte auf dem Gebiet der Röntgenstrahlen und der bildgebenden Verfahren*, vol. 174, p. 830–834, July 2002.

[158] J. Schnabel, C. Tanner, A. Castellano-Smith, A. Degenhard, M. Leach, D. Hose, D. Hill, and D. Hawkes, "Validation of nonrigid image registration using finite-element methods: application to breast mr images," *IEEE Transactions on Medical Imaging*, vol. 22, p. 238–247, Feb. 2003.

[159] M. Eder, S. Raith, J. Jalali, A. Volf, M. Settles, H.-G. Machens, and L. Kovacs, "Comparison of different material models to simulate 3-d breast deformations using finite element analysis," *Annals of Biomedical Engineering*, vol. 42, p. 843–857, Dec. 2013.

[160] F. S. Azar, D. N. Metaxas, and M. D. Schnall, "A deformable finite element model of the breast for predicting mechanical deformations under external perturbations," *Academic Radiology*, vol. 8, p. 965–975, Oct. 2001.

[161] A. Samani and D. Plewes, "A method to measure the hyperelastic parameters ofex vivobreast tissue samples," *Physics in Medicine and Biology*, vol. 49, p. 4395–4405, Sept. 2004.

[162] A. Samani, J. Zubovits, and D. Plewes, "Elastic moduli of normal and pathological human breast tissues: an inversion-technique-based investigation of 169 samples," *Physics in Medicine and Biology*, vol. 52, p. 1565–1576, Feb. 2007.

[163] C. Tanner, J. A. Schnabel, D. L. G. Hill, D. J. Hawkes, M. O. Leach, and D. R. Hose, "Factors influencing the accuracy of biomechanical breast models: Factors influencing the accuracy of biomechanical breast models," *Medical Physics*, vol. 33, p. 1758–1769, May 2006.

[164] A. P. del Palomar, B. Calvo, J. Herrero, J. López, and M. Doblaré, "A finite element model to accurately predict real deformations of the breast," *Medical Engineering and Physics*, vol. 30, p. 1089–1097, Nov. 2008.

[165] V. Rajagopal, A. Lee, J.-H. Chung, R. Warren, R. P. Highnam, M. P. Nash, and P. M. Nielsen, "Creating individual-specific biomechanical models of the breast for medical image analysis," *Academic Radiology*, vol. 15, p. 1425–1436, Nov. 2008.

[166] A. Lapuebla-Ferri, A. P. del Palomar, J. Herrero, and A.-J. Jiménez-Mocholí, "A patient-specific fe-based methodology to simulate prosthesis insertion during an augmentation mammoplasty," *Medical Engineering and Physics*, vol. 33, p. 1094–1102, Nov. 2011.

[167] D. E. McGhee and J. R. Steele, "Breast biomechanics: What do we really know?," *Physiology*, vol. 35, p. 144–156, Mar. 2020.

[168] V. Rajagopal, P. M. F. Nielsen, and M. P. Nash, "Modeling breast biomechanics for multi-modal image analysis—successes and challenges," *WIREs Systems Biology and Medicine*, vol. 2, p. 293–304, Apr. 2010.

[169] C. Tanner, M. White, S. Guarino, M. A. Hall-Craggs, M. Douek, and D. J. Hawkes, "Large breast compressions: Observations and evaluation of simulations," *Medical Physics*, vol. 38, p. 682–690, Jan. 2011.

[170] L. Han, J. H. Hipwell, C. Tanner, Z. Taylor, T. Mertzanidou, J. Cardoso, S. Ourselin, and D. J. Hawkes, "Development of patient-specific biomechanical models for predicting large breast deformation," *Physics in Medicine and Biology*, vol. 57, p. 455–472, Dec. 2011.

[171] C. M. L. Hsu, M. L. Palmeri, W. P. Segars, A. I. Veress, and J. T. Dobbins, "An analysis of the mechanical parameters used for finite element compression of a high-resolution 3d breast phantom: Mechanical parameter analysis for compressing 3d breast phantom," *Medical Physics*, vol. 38, p. 5756–5770, Sept. 2011.

[172] A. W. Lee, V. Rajagopal, T. P. Babarenda Gamage, A. J. Doyle, P. M. Nielsen, and M. P. Nash, "Breast lesion co-localisation between x-ray and mr images using finite element modelling," *Medical Image Analysis*, vol. 17, p. 1256–1264, Dec. 2013.

[173] T. Hopp, M. Dietzel, P. Baltzer, P. Kreisel, W. Kaiser, H. Gemmeke, and N. Ruiter, "Automatic multimodal 2d/3d breast image registration using biomechanical fem models and intensity-based optimization," *Medical Image Analysis*, vol. 17, p. 209–218, Feb. 2013.

[174] T. Mertzanidou, J. Hipwell, S. Johnsen, L. Han, B. Eiben, Z. Taylor, S. Ourselin, H. Huisman, R. Mann, U. Bick, N. Karssemeijer, and D. Hawkes, "Mri to x-ray mammography intensity-based registration with simultaneous optimisation of pose and biomechanical transformation parameters," *Medical Image Analysis*, vol. 18, p. 674–683, May 2014.

[175] J. A. Solves-Llorens, M. J. Rupérez, C. Monserrat, E. Feliu, M. García, and M. Lloret, "A complete software application for automatic registration of x-ray mammography and magnetic resonance images," *Medical Physics*, vol. 41, July 2014.

[176] E. García, A. Oliver, O. Diaz, Y. Diez, A. Gubern-Mérida, R. Martí, and J. Martí, "Mapping 3d breast lesions from full-field digital mammograms using subject-specific finite element models," in *Medical Imaging 2017: Image-Guided Procedures, Robotic Interventions, and Modeling* (R. J. Webster and B. Fei, eds.), SPIE, Mar. 2017.

[177] A. Mîra, A.-K. Carton, S. Muller, and Y. Payan, "A biomechanical breast model evaluated with respect to mri data collected in three different positions," *Clinical Biomechanics*, vol. 60, p. 191–199, Dec. 2018.

[178] C. Xue, F.-H. Tang, C. W. K. Lai, L. J. Grimm, and J. Y. Lo, "Multimodal patient-specific registration for breast imaging using biomechanical modeling with reference to ai evaluation of breast tumor change," *Life*, vol. 11, p. 747, July 2021.

[179] N. Ruiter, *Registration of X-ray Mammograms and MR-volumes of the Female Breast Based on Simulated Mammographic Deformation*. Mensch-und-Buch-Verlag, 2004.

[180] P. R. Bakic, M. Albert, D. Brzakovic, and A. D. A. Maidment, "Mammogram synthesis using a 3d simulation. i. breast tissue model and image acquisition simulation," *Medical Physics*, vol. 29, p. 2131–2139, Aug. 2002.

[181] L. W. Zhang, A. S. Ademiloye, and K. M. Liew, "Meshfree and particle methods in biomechanics: Prospects and challenges," *Archives of Computational Methods in Engineering*, vol. 26, p. 1547–1576, Sept. 2018.

[182] F. Martínez-Martínez, M. Rupérez-Moreno, M. Martínez-Sober, J. Solves-Llorens, D. Lorente, A. Serrano-López, S. Martínez-Sanchis, C. Monserrat, and J. Martín-Guerrero, "A finite element-based machine learning approach for modeling the mechanical behavior of the breast tissues under compression in real-time," *Computers in Biology and Medicine*, vol. 90, p. 116–124, Nov. 2017.

[183] K. Wang and T. Kesavadas, "Real-time fea-based breast deformation simulation using artificial neural network," *Computer Methods and Programs in Biomedicine Update*, vol. 2, p. 100052, 2022.

[184] C. E. Miller, J. H. Jordan, A. Thomas, and J. A. Weis, "Developing a biomechanical model-based elasticity imaging method for assessing hormone receptor positive breast cancer treatment-related myocardial stiffness changes," *Journal of Medical Imaging*, vol. 8, Sept. 2021.

[185] R. Cortez, L. Fauci, and A. Medovikov, "The method of regularized stokeslets in three dimensions: Analysis, validation, and application to helical swimming," *Physics of Fluids*, vol. 17, Feb. 2005.

[186] J. Hadamard, "Sur les problèmes aux dérivées partielles et leur signification physique," *Princeton university bulletin*, pp. 49–52, 1902.

[187] A. W. Stabile, M. J. Ringel, W. L. Richey, J. S. Heiselman, I. Meszoely, and M. I. Miga, "Stereovision registration using a tracked checkerboard calibration object for a breast surgery image guidance system," in *Medical Imaging 2023: Image-Guided Procedures, Robotic Interventions, and Modeling* (C. A. Linte and J. H. Siewerdsen, eds.), SPIE, Apr. 2023.

[188] K. S. Arun, T. S. Huang, and S. D. Blostein, "Least-squares fitting of two 3-d point sets," *IEEE Transactions on Pattern Analysis and Machine Intelligence*, vol. PAMI-9, p. 698–700, Sept. 1987.

[189] T. K. Chen, A. D. Thurston, R. E. Ellis, and P. Abolmaesumi, "A real-time freehand ultrasound calibration system with automatic accuracy feedback and control," *Ultrasound in Medicine and Biology*, vol. 35, p. 79–93, Jan. 2009.

[190] M. J. Ringel, W. L. Richey, J. S. Heiselman, M. Luo, I. M. Meszoely, and M. I. Miga, "Supine magnetic resonance image registration for breast surgery: insights on material mechanics," *Journal of Medical Imaging*, vol. 9, no. 6, p. 065001, 2022.

[191] M. J. Ringel, W. L. Richey, J. S. Heiselman, I. M. Meszoely, and M. I. Miga, "Incorporating heterogeneity and anisotropy for surgical applications in breast deformation modeling," *Clinical Biomechanics*, vol. 104, p. 105927, Apr. 2023.

[192] H. Mehrabian, L. Richmond, Y. Lu, and A. L. Martel, "Deformable registration for longitudinal breast mri screening," *Journal of Digital Imaging*, vol. 31, p. 718–726, Apr. 2018.

[193] S. Thakran, E. Cohen, N. Jahani, S. P. Weinstein, L. Pantalone, N. Hylton, D. Newitt, A. DeMichele, C. Davatzikos, and D. Kontos, "Impact of deformable registration methods for prediction of recurrence free survival response to neoadjuvant chemotherapy in breast cancer: Results from the ispy 1/acrin 6657 trial," *Translational Oncology*, vol. 20, p. 101411, June 2022.

[194] J. A. Weis, M. I. Miga, and T. E. Yankeelov, "Three-dimensional image-based mechanical modeling for predicting the response of breast cancer to neoadjuvant therapy," *Computer Methods in Applied Mechanics and Engineering*, vol. 314, p. 494–512, Feb. 2017.

[195] T. P. B. Gamage, R. Boyes, V. Rajagopal, P. M. F. Nielsen, and M. P. Nash, *Modelling Prone to Supine Breast Deformation Under Gravity Loading Using Heterogeneous Finite Element Models*, p. 29–38. Springer New York, 2012.

[196] B. Eiben, L. Han, J. Hipwell, T. Mertzanidou, S. Kabus, T. Buelow, C. Lorenz, G. Newstead, H. Abe, M. Keshtgar, S. Ourselin, and D. Hawkes, "Biomechanically guided prone-to-supine image registration of breast mri using an estimated reference state," in *2013 IEEE 10th International Symposium on Biomedical Imaging*, IEEE, Apr. 2013.

[197] L. Han, J. H. Hipwell, B. Eiben, D. Barratt, M. Modat, S. Ourselin, and D. J. Hawkes, "A nonlinear biomechanical model based registration method for aligning prone and supine mr breast images," *IEEE Transactions on Medical Imaging*, vol. 33, p. 682–694, Mar. 2014.

[198] E. García, Y. Diez, O. Diaz, X. Lladó, A. Gubern-Mérida, R. Martí, J. Martí, and A. Oliver, "Breast mri and x-ray mammography registration using gradient values," *Medical Image Analysis*, vol. 54, p. 76–87, May 2019.

[199] C. Goodbrake, D. S. Li, H. Aghakhani, A. Contreras, G. P. Reece, M. K. Markey, and M. S. Sacks, "On the three-dimensional mechanical behavior of human breast tissue," *Annals of Biomedical Engineering*, vol. 50, p. 601–613, Mar. 2022.

[200] J. H. Hipwell, V. Vavourakis, L. Han, T. Mertzanidou, B. Eiben, and D. J. Hawkes, "A review of biomechanically informed breast image registration," *Physics in Medicine and Biology*, vol. 61, p. R1–R31, Jan. 2016.

[201] N. J. Tustison and B. B. Avants, "Explicit b-spline regularization in diffeomorphic image registration," *Frontiers in Neuroinformatics*, vol. 7, 2013.

[202] N. Otsu, "A threshold selection method from gray-level histograms," *IEEE Transactions on Systems, Man, and Cybernetics*, vol. 9, p. 62–66, Jan. 1979.

[203] J. M. Sullivan, G. Charron, and K. D. Paulsen, "A three-dimensional mesh generator for arbitrary multiple material domains," *Finite Elements in Analysis and Design*, vol. 25, p. 219–241, Apr. 1997.

[204] R. Amelon, K. Cao, K. Ding, G. E. Christensen, J. M. Reinhardt, and M. L. Raghavan, "Three-dimensional characterization of regional lung deformation," *Journal of Biomechanics*, vol. 44, p. 2489–2495, Sept. 2011.

[205] N. Jahani, E. Cohen, M.-K. Hsieh, S. P. Weinstein, L. Pantalone, N. Hylton, D. Newitt, C. Davatzikos, and D. Kontos, "Prediction of treatment response to neoadjuvant chemotherapy for breast cancer via early changes in tumor heterogeneity captured by dce-mri registration," *Scientific Reports*, vol. 9, Aug. 2019.

[206] R. F. Woolson, "Wilcoxon signed-rank test," Sept. 2008.

[207] Y. Ou, S. P. Weinstein, E. F. Conant, S. Englander, X. Da, B. Gaonkar, M. Hsieh, M. Rosen, A. DeMichele, C. Davatzikos, and D. Kontos, "Deformable registration for quantifying longitudinal tumor changes during neoadjuvant chemotherapy," *Magnetic Resonance in Medicine*, vol. 73, p. 2343–2356, July 2014.

[208] X. Li, B. M. Dawant, E. B. Welch, A. B. Chakravarthy, D. Freehardt, I. Mayer, M. Kelley, I. Meszoely, J. C. Gore, and T. E. Yankeelov, "A nonrigid registration algorithm for longitudinal breast mr images and the analysis of breast tumor response," *Magnetic Resonance Imaging*, vol. 27, p. 1258–1270, Nov. 2009.

[209] Y. Guo, R. Sivaramakrishna, C.-C. Lu, J. S. Suri, and S. Laxminarayan, "Breast image registration techniques: a survey," *Medical and Biological Engineering and Computing*, vol. 44, p. 15–26, Feb. 2006.

[210] N. Briot, G. Chagnon, C. Masri, E. Girard, and Y. Payan, "Ex-vivo mechanical characterisation of the breast cooper's ligaments," *Computer Methods in Biomechanics and Biomedical Engineering*, vol. 23, p. S49–S51, Oct. 2020.

[211] A. M. McCarthy, B. M. Keller, L. M. Pantalone, M.-K. Hsieh, M. Synnestvedt, E. F. Conant, K. Armstrong, and D. Kontos, "Racial differences in quantitative measures of area and volumetric breast density," *Journal of the National Cancer Institute*, vol. 108, p. djw104, Apr. 2016.

[212] M. J. Plaza, E. A. Morris, and S. B. Thakur, "Diffusion tensor imaging in the normal breast: influences of fibroglandular tissue composition and background parenchymal enhancement," *Clinical Imaging*, vol. 40, p. 506–511, May 2016.

[213] M. Ringel, J. Heiselman, W. Richey, I. Meszoely, and M. Miga, *Regularized Kelvinlet Functions to Model Linear Elasticity for Image-to-Physical Registration of the Breast*, p. 344–353. Springer Nature Switzerland, 2023.

[214] M. Ringel, J. Heiselman, W. Richey, I. Meszoely, W. Jarnagin, and M. Miga, "Comparing regularized kelvinlet functions and the finite element method for registration of medical images to sparse organ data," 2023.

[215] P. Gavriilidis, B. Edwin, E. Pelanis, E. Hidalgo, N. de'Angelis, R. Memeo, L. Aldrighetti, and R. P. Sutcliffe, "Navigated liver surgery: State of the art and future perspectives," *Hepatobiliary and Pancreatic Diseases International*, vol. 21, p. 226–233, June 2022.

[216] F. A. Schmidt, M. Mullally, M. Lohmann, P. Hiepe, S. Kirnaz, S. Chidambaram, C. Wipplinger, and R. Härtl, "Elastic image fusion software to coregister preoperatively planned pedicle screws with intraoperative computed tomography data for image-guided spinal surgery," *International Journal of Spine Surgery*, vol. 15, p. 295–301, Mar. 2021.

[217] J. A. Collins, J. A. Weis, J. S. Heiselman, L. W. Clements, A. L. Simpson, W. R. Jarnagin, and M. I. Miga, "Improving registration robustness for image-guided liver surgery in a novel human-to-phantom data framework," *IEEE Transactions on Medical Imaging*, vol. 36, p. 1502–1510, July 2017.

[218] O. Zettinig, A. Shah, C. Hennersperger, M. Eiber, C. Kroll, H. Kübler, T. Maurer, F. Milletarì, J. Rackerseder, C. Schulte zu Berge, E. Storz, B. Frisch, and N. Navab, "Multimodal image-guided prostate fusion biopsy based on automatic deformable registration," *International Journal of Computer Assisted Radiology and Surgery*, vol. 10, p. 1997–2007, June 2015.

[219] M. Pfeiffer, C. Riediger, S. Leger, J.-P. Kühn, D. Seppelt, R.-T. Hoffmann, J. Weitz, and S. Speidel, *Non-Rigid Volume to Surface Registration Using a Data-Driven Biomechanical Model*, p. 724–734. Springer International Publishing, 2020.

[220] Y. Fu, Y. Lei, T. Wang, P. Patel, A. B. Jani, H. Mao, W. J. Curran, T. Liu, and X. Yang, "Biomechanically constrained non-rigid mr-trus prostate registration using deep learning based 3d point cloud matching," *Medical Image Analysis*, vol. 67, p. 101845, Jan. 2021.

[221] G. Balakrishnan, A. Zhao, M. R. Sabuncu, J. Guttag, and A. V. Dalca, "Voxelmorph: A learning framework for deformable medical image registration," *IEEE Transactions on Medical Imaging*, vol. 38, p. 1788–1800, Aug. 2019.

[222] I. Peterlík, H. Courtecuisse, R. Rohling, P. Abolmaesumi, C. Nguan, S. Cotin, and S. Salcudean, "Fast elastic registration of soft tissues under large deformations," *Medical Image Analysis*, vol. 45, p. 24–40, Apr. 2018.

[223] T. Belytschko, Y. Y. Lu, and L. Gu, "Element-free galerkin methods," *International Journal for Numerical Methods in Engineering*, vol. 37, p. 229–256, Jan. 1994.

[224] W. L. Richey, J. S. Heiselman, M. J. Ringel, I. M. Meszoely, and M. I. Miga, "Tumor deformation correction for an image guidance system in breast conserving surgery," in *Medical Imaging 2022: Image-Guided Procedures, Robotic Interventions, and Modeling* (C. A. Linte and J. H. Siewerdsen, eds.), SPIE, Apr. 2022.

[225] R. H. Griesenauer, J. A. Weis, L. R. Arlinghaus, I. M. Meszoely, and M. I. Miga, "Breast tissue stiffness estimation for surgical guidance using gravity-induced excitation," *Physics in Medicine and Biology*, vol. 62, p. 4756–4776, May 2017.

[226] W. L. Richey, J. S. Heiselman, M. J. Ringel, I. M. Meszoely, and M. I. Miga, "Soft tissue monitoring of the surgical field: Detection and tracking of breast surface deformations," *IEEE Transactions on Biomedical Engineering*, vol. 70, p. 2002–2012, July 2023.

[227] M. J. Ringel, W. L. Richey, J. S. Heiselman, A. Stabile, I. M. Meszoely, and M. I. Miga, "Image guidance system for breast conserving surgery with integrated stereo camera monitoring and deformable correction," in *Medical Imaging 2024: Image-Guided Procedures, Robotic Interventions, and Modeling* (C. A. Linte and J. H. Siewerdsen, eds.), SPIE, 2024.

[228] M. Van Goethem, W. Tjalma, K. Schelfout, I. Verslegers, I. Biltjes, and P. Parizel, "Magnetic resonance imaging in breast cancer," *European Journal of Surgical Oncology (EJSO)*, vol. 32, p. 901–910, Nov. 2006.

[229] A. Fedorov, R. Beichel, J. Kalpathy-Cramer, J. Finet, J.-C. Fillion-Robin, S. Pujol, C. Bauer, D. Jennings, F. Fennessy, M. Sonka, J. Buatti, S. Aylward, J. V. Miller, S. Pieper, and R. Kikinis, "3d slicer as an image computing platform for the quantitative imaging network," *Magnetic Resonance Imaging*, vol. 30, p. 1323–1341, Nov. 2012.

[230] T. Ungi, A. Lasso, and G. Fichtinger, "Open-source platforms for navigated image-guided interventions," *Medical Image Analysis*, vol. 33, p. 181–186, Oct. 2016.

[231] J. Tokuda, G. S. Fischer, X. Papademetris, Z. Yaniv, L. Ibanez, P. Cheng, H. Liu, J. Blevins, J. Arata, A. J. Golby, T. Kapur, S. Pieper, E. C. Burdette, G. Fichtinger, C. M. Tempany, and N. Hata, "Openigtlink: an open network protocol for image-guided therapy environment," *The International Journal of Medical Robotics and Computer Assisted Surgery*, vol. 5, p. 423–434, July 2009.

[232] A. Lasso, T. Heffter, A. Rankin, C. Pinter, T. Ungi, and G. Fichtinger, "Plus: Open-source toolkit for ultrasound-guided intervention systems," *IEEE Transactions on Biomedical Engineering*, vol. 61, p. 2527–2537, Oct. 2014.

[233] E. Léger, S. Drouin, D. L. Collins, T. Popa, and M. Kersten-Oertel, "Quantifying attention shifts in augmented reality image-guided neurosurgery," *Healthcare Technology Letters*, vol. 4, p. 188–192, Sept. 2017.

[234] M. Birlo, P. E. Edwards, M. Clarkson, and D. Stoyanov, "Utility of optical see-through head mounted displays in augmented reality-assisted surgery: A systematic review," *Medical Image Analysis*, vol. 77, p. 102361, 2022.

[235] J. Ramalhinho, S. Yoo, T. Dowrick, B. Koo, M. Somasundaram, K. Gurusamy, D. J. Hawkes, B. Davidson, A. Blandford, and M. J. Clarkson, "The value of augmented reality in surgery — a usability study on laparoscopic liver surgery," *Medical Image Analysis*, vol. 90, p. 102943, 2023.

[236] C. M. Andrews, A. B. Henry, I. M. Soriano, M. K. Southworth, and J. R. Silva, "Registration techniques for clinical applications of three-dimensional augmented reality devices," *IEEE Journal of Translational Engineering in Health and Medicine*, vol. 9, pp. 1–14, 2021.

[237] C. T. Morley, D. M. Arreola, L. Qian, A. L. Lynn, Z. P. Veigulis, and T. F. Osborne, "Mixed reality surgical navigation system; positional accuracy based on food and drug administration standard," *Surgical Innovation*, vol. 31, p. 48–57, Nov. 2023.

[238] J. H. Matthews and J. S. Shields, "The clinical application of augmented reality in orthopaedics: Where do we stand?," *Current Reviews in Musculoskeletal Medicine*, vol. 14, pp. 316–319, Oct 2021.

[239] M. Miga, D. Roberts, F. Kennedy, L. Platenik, A. Hartov, K. Lunn, and K. Paulsen, "Modeling of retraction and resection for intraoperative updating of images," *Neurosurgery*, vol. 49, pp. 75–84; discussion 84–5, Jul 2001.

[240] J. Chen and M. Desbrun, "Go green: General regularized green's functions for elasticity," in *ACM SIGGRAPH 2022 Conference Proceedings*, SIGGRAPH '22, (New York, NY, USA), Association for Computing Machinery, 2022.

[241] J. S. Heiselman, J. A. Collins, M. J. Ringel, W. R. Jarnagin, and M. I. Miga, "Comparison study of sparse data-driven soft tissue registration: preliminary results from the image-to-physical liver registration sparse data challenge," in *Medical Imaging 2023: Image-Guided Procedures, Robotic Interventions, and Modeling* (C. A. Linte and J. H. Siewerdsen, eds.), vol. 12466, p. 124660M, International Society for Optics and Photonics, SPIE, 2023.

[242] J. S. Heiselman, J. A. Collins, M. J. Ringel, T. P. Kingham, W. R. Jarnagin, and M. I. Miga, "The Image-to-Physical Liver Registration Sparse Data Challenge: comparison of state-of-the-art using a common dataset," *Journal of Medical Imaging*, vol. 11, no. 1, p. 015001, 2024.

[243] M. I. Miga, E. L. Brewer, L. W. Clements, J. A. Collins, D. J. Doss, J. S. Heiselman, C. D. Pavas, and E. H. Wisdom, "The image-to-physical liver registration sparse data challenge," in *Medical Imaging 2019: Image-Guided Procedures, Robotic Interventions, and Modeling* (B. Fei and C. A. Linte, eds.), SPIE, Mar. 2019.